Entwicklung eines Verfahrens zur thermischen Zerlegung von Methan zu Wasserstoff und Kohlenstoff unter Nutzung flüssiger Metalle als Wärmeübertragungsmedium

zur Erlangung des akademischen Grades eines
DOKTORS DER INGENIEURWISSENSCHAFTEN (Dr.-Ing.)

der Fakultät für Chemieingenieurwesen und Verfahrenstechnik des
Karlsruher Instituts für Technologie (KIT)

genehmigte
DISSERTATION

von
Dipl.-Ing. Michael Plevan
aus Hirschau, Bayern

Referent: Prof. Dr. Thomas Wetzel
Korreferent: Prof. Dr. Georg Schaub
Tag der mündlichen Prüfung: 28. März 2017

“If you can meet with Triumph and Disaster

And treat those two impostors just the same”

- Rudyard Kipling, *“Rewards and Fairies” (1910)*

Erklärung

Hiermit versichere ich, die vorliegende Arbeit selbständig und nur unter Verwendung der angegebenen Hilfsmittel angefertigt zu haben.

München, 30. Mai 2017

Vorname, Name

Danksagung

Herrn Prof. Dr.-Ing. Wetzel danke ich für die freiheitliche und inspirierende Betreuung der vorliegenden Arbeit während meiner Tätigkeit am KALLA-Labor und danach und insbesondere für das mir entgegengebrachte Vertrauen, auf diesem für einen Maschinenbauingenieur nicht naheliegenden Fachbereich eine Dissertation anfertigen zu können. Ebenso möchte ich mich bei Herrn Prof. Dr.-Ing. Georg Schaub für das Interesse an dieser Arbeit und für die Übernahme des Korrefarats bedanken.
Der Erfolg dieser Arbeit ist zudem zu einem großen Teil auf die wissenschaftliche und technische Unterstützung vieler Kolleginnen und Kollegen des Instituts für Kern- und Energietechnik IKET und des KALLA-Labors zurückzuführen, insbesondere auf die Unterstützung von Herrn Dr. Leonid Stoppel, Herrn Markus Daubner, Herrn Frank Fellmoser und Herrn Kurt Wittemann und besonders auf die Mitarbeit meines Doktoranden-Kollegen in diesem Projekt, Herrn Tobias Geißler.
Neben der fachlichen Unterstützung möchte ich mich bei allen Kollegen des KALLA-Labors für die außerordentlich schöne und lehrreiche Zeit am Campus Nord des KIT bedanken. Einen ganz besonderen Dank möchte ich an meinen Bürokollegen Herrn Dr. Julio Caesar Pacio richten, der mich unermüdlich und zu jeder Zeit in allen wissenschaftlichen und organisatorischen Fragen im Rahmen dieser Arbeit und vielen damit verbundenen Tätigkeiten unterstützt hat.
Auch unseren externen Projektpartnern, den Kollegen des IASS aus Potsdam und den Kollegen aus der LIMTECH Helmholtz Allianz sowie den KIT- internen Projektpartnern zugehörig dem IHM und dem IAM-WPT fühle ich mich zu großem Dank verpflichtet.
Zuguterletzt danke ich sehr herzlich allen an diesem Projekt mitwirkenden Studenten, insbesondere Herrn Sebastian Herbst und Herrn Jonas Hansen.

Contents

List of Figures

List of Tables

Chapter 1

Introduction

The anthropogenic greenhouse-gas emission associated to the combustion of fossil fuels is considered to have a negative impact on the global climate. It is a prevailing opinion that the emission of substances which are produced during combustion, particularly $\mathrm{CO_2}$, contribute to the increase of the global mean temperature. In return, an increased global mean temperature threatens life on earth due to harsher environmental conditions. In response to this adverse climatic event, advanced energy conversion processes are needed without intrinsic formation of $\mathrm{CO_2}$ emissions, yet with a similar portfolio of processes. Referring to the automotive sector in this respect, the utilization of hydrogen-driven propulsion technologies may be an applicable solution for replacing traditional combustion engines. Existing hydrogen-powered commercial vehicle concepts as well as ongoing research activities in this field of study show that hydrogen energy -being either combusted directly or converted into electric energy by means of fuel cell devices- indeed has a great potential for replacing fossil-fuel driven processes, especially in the long-range vehicle segment. Granovskii et al. [1] found that if hydrogen is produced by renewable energy sources, hence from sources with no intrinsic formation

of CO_2 emissions, and is subsequently applied in a PEMFC[1] vehicle, the greenhouse-gas emissions are minimized. However, he admits that current state of the art CO_2-free technologies for producing hydrogen, namely producing hydrogen from wind-powered electrolysis processes, are currently economically not attractive.

As of today, 96% of the globally produced hydrogen is currently gained from fossil fuel feedstock by means of CO_2-emitting processes, mainly by steam reforming of natural gas (48%). Apart from steam reforming, partial oxidation of hydrocarbons (30%) and partial oxidation of coal (18%) are further utilized to produce hydrogen; all with a considerable amount of intrinsic CO_2 emissions. Only 4% of the hydrogen is produced by electrolysis [2], [3]. At production costs of about 3.8 € per kg in the case of grid-powered electrolysis and about 8.8 € per kg in the case of photo-catalytic water splitting [4], alternative CO_2-free technologies for hydrogen production are much more costly than traditional hydrogen production technologies such as steam reforming with production costs of about 0.8 € per kg [4].

Thermal decomposition of methane (TDM), also known as methane pyrolysis or methane cracking, could serve as a transition technology, providing a missing link between the cheap but CO_2-emitting fossil fuel driven processes and the clean yet expensive alternative forms of hydrogen production. The overall pyrolysis reaction of methane is endothermic and can be expressed as

$$\mathrm{CH_4(g)} \rightarrow \mathrm{C(s)} + 2\mathrm{H_2(g)} \quad \Delta \mathrm{H_R^0} = 75\,\mathrm{kJ/mol} \tag{1.1}$$

starting at about 700 °C [6]. Since heat is the only energy vector needed for the reaction to proceed, a vast variety of different heat sources, reactor types and catalysts have

[1] PEMFC: Proton exchange membrane fuel cell; mostly utilized in the automotive sector.

been studied in lab-scale experiments during the last decades. Beside the investigation of the most efficient reactor/catalyst combination, the understanding of the chemical processes in terms of thermodynamics, reaction mechanisms and especially the reaction kinetics have been investigated as well for specific reactor configurations. However, studying existing state of the art literature, it is apparent that all investigated reactor types and configurations show similar continuous reactor-operation problems which in fact are seemingly more urgent to be solved than gaining additional knowledge about the reaction kinetics of a further specific reactor operation condition.

To address the problem of identifying a suitable reactor setup for continuous reactor operation, the objective of this study is to discuss thermal decomposition of methane in the presence of a liquid heat transfer medium. In parallel, a simple thermo-chemical model is proposed, providing a conversion estimation on the basis of different kinetic data, taken from literature. For the model, a sectional modeling approach is used in order to address the different heat-up and conversion characteristics of methane gas bubbling through liquid metal or flushing through a blank tube. The model is implemented using several different kinetic parameters taken from literature.

This thesis is structured as follows. Chapter 2 provides an overview of the global energy situation and addresses the potential of hydrogen technologies with respect to current and future scenarios. The subsequent chapter 3 focuses on the TDM process for hydrogen production and compares different reactor concepts for the ideal TDM process. In chapter 4, a falsification approach is presented on the basis of a study conducted by Serban et al. [5] which incited the research project, in which this work was embedded. Within this chapter, the identified falsification approach is applied to the findings of this thesis. Basic hypotheses are developed, serving as the starting point for the experimental investigations. Chapter 5 focuses on experiments and results obtained during

two-phase flow measurements in liquid metal. Chapter 6 serves as technical report for the process of developing the own experimental reactor facility and provides information regarding the problems to be solved during the design and operation phases, covering further the experimental results measured during own TDM experiments. Chapter 7 focuses on the features of the thermo-chemical model of the reactor. Subsequently, chapter 8 compares modeling and experimental results. As an additional feature, chapter 9 discusses in detail the experimental results provided by Serban et al. [5] in view of the herewithin obtained theoretical and experimental results. In the final chapters 10 and 11, concluding remarks in the context of the claimed hypotheses and an outlook are stated.

Chapter 2

Hydrogen production technologies: Current situation and prospects

---

► Within this chapter, the socio-economic aspects of a hydrogen society are discussed and put into relation with possible hydrogen production processes.

2.1 Environmental effects of current energy systems

In its 2012 report on energy technology perspectives, the international energy agency IEA[1] defined a plurality of pathways for the energy sector, designed to reduce global warming. The pathways are divided into so-called “2 DS” and “4 DS” scenarios, referring to a temperature increase of 2 °C or 4 °C until reaching of the year 2050. According to the IEA [7], a temperature increase of 6 °C might occur if no actions are taken to address climate change and energy security concerns. On the basis of IEA’s data, which is widely accepted in the global society, the necessity to transform the current energy system into a carbon-free[2] system appears evident.

2.2 Prospects of hydrogen technologies

The IEA [7] concludes that in order to be in sync with the 2 DS-scenario, the annual worldwide consumption of fossil fuels must drop by 20% till the year 2050 compared to the year 2009[3]. Here, consumption is equated with combustion processes or other processes that comprise an intrinsic formation of green-house gas emissions, particularly carbonaceous elements. In order to reach the goal of the 20% reduction, especially the automotive transport segment needs to be reshaped to great extents [7]. In this context,

[1] The International Energy Agency (IEA), an autonomous agency, was established in November 1974. Its primary mandate was - and is - two-fold: to promote energy security amongst its member countries through collective response to physical disruptions in oil supply, and provide authoritative research and analysis on ways to ensure reliable, affordable and clean energy for its 28 member countries and beyond.

[2] The term "carbon-free system" relates to an energy system comprising no emissions of carbonaceous, gaseous elements, mainly hydrocarbons and carbon-dioxide

[3] Fossil fuel use will only drop by some 20% in 2050 compared to 2009 levels. In transport, oil is replaced by a portfolio of three alternative fuels (or energy carriers): electricity, hydrogen and biofuels. These will require a revolution in vehicle propulsion systems, particularly the electrification of light duty vehicles LDV’s. [7]

hydrogen energy has a tremendous potential for being utilized as fuel, due to the fact that it may be stored and transported in liquid state utilizing for example a fuel tank on board of a vehicle. Since hydrogen may either be combusted in conventional piston-based internal combustion engines (ICE) or be converted into electric energy, a great range of engine concepts can be realized and fitted to the given engine requirements. Known are ICE's, electric, fuel cell powered drive-trains, hybrids thereof or hybrids composed of one of the previous systems in combination with a fossil fuel-powered ICE. Moreover, contrary to battery-powered electric propulsion systems, charging the vehicle may be achieved within the time-span of a few minutes, which is in the same order of magnitude compared to time-spans required for charging traditional, fossil fuel driven vehicles.

Even though the practicability of battery-powered vehicles is increasing due to advanced electro-chemical storage technologies of electric energy, there will always be a substantially large niche within the transportation segment where the utilization of batteries is not feasible. Hydrogen-based emission-free propulsion alternative could be implemented for instance in trucking vehicles, heavy-duty vehicles in general, ships and even aircrafts. Apart from transportation, hydrogen may be replacing a wide range of further stationary or mobile propulsion or electricity-providing applications. The limiting factor is merely characterized by the lack of hydrogen availability; hence a lack of de-centralized hydrogen production and hydrogen storage sites.

2.3 Today's predominant hydrogen production technologies

Apart from envisaged future applications of hydrogen energy in the context of a "Hydrogen Society" or "Hydrogen Economy", even today the production of hydrogen already is a mature industry with a total annual production of 0.1 Gton [8]. Unfortunately and somewhat ironically, today's hydrogen production processes themselves significantly contribute to anthropologic greenhouse-gas emissions. Meeting the objectives of the 2 DS scenario, not only hydrogen propulsion technologies, but even more urgently, clean forms of hydrogen production technologies have to be developed and implemented in the global energy markets. Previously stated figure referring to the globally produced amount of hydrogen however might give a false impression of current hydrogen production technologies. According to IEA, current hydrogen production is split 50-50 between the refining and chemical industries [7], whereas the amount of hydrogen produced for other industries, such as the automotive sector, may still be neglected. More detailed, in the refining industry, hydrogen is in most cases produced on-site and immediately consumed during intermediate refining steps which are needed for catalytic reformation processes. Since the production and utilization of hydrogen is interlaced into the refining process itself, it appears far-fetched to stress alternative hydrogen sources for said industry in near future. However, in chemical industries and especially for ammonia- and nitrogen-based fertilizer production industries, large amounts of externally supplied hydrogen are used for the chemical processing, comprising a considerable potential for reducing the CO_2-footprint of said processes by the utilization of carbon-free produced hydrogen. Considering the total amount of globally produced hydrogen, about 96% originates from fossil fuels, while only 4% is produced using regenerative sources, mostly

water electrolysis. All industries put together, hydrogen production is realized by steam reforming of natural gas (48%), partial oxidation of oil-based hydrocarbons (30%), and coal gasification (18%), see also fig. 2.1. Oil-based feedstock is almost entirely consumed by refining processes; thus, showing only little potential for implementing “clean hydrogen” technologies. Therefore, despite the fact that oil-based hydrogen production processes have the highest intrinsically produced $\mathrm{CO_2}$-emissions, said production forms are discarded within this assessment. The current portfolio of hydrogen production can best be explained on behalf of ammonia production; by far the biggest hydrogen consuming industry. According to IEA, hydrogen produced for the ammonia process is about 77% based on steam reforming of natural gas, 20% is being produced by coal gasification and 3% of the produced hydrogen originates from other sources such as fuel oil, naphtha and regenerative sources [2]. Consequently, it may be concluded that the economic benchmark for current hydrogen production is defined by the process of steam reforming of natural gas.

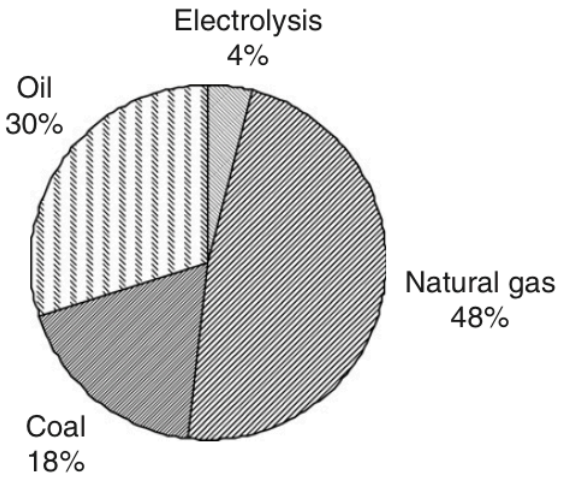

Figure 2.1: Feedstock used currently in global hydrogen production [2]

2.4 Steam reforming of methane: Brief analysis of greenhouse-gas emission, efficiency and costs

Current industrial-scale steam reforming cycles are usually composed of a series of at least two individual processes, which are preceded by a cleaning step for removing impurities from the natural gas. In the first step, a synthesis gas is produced during an endothermic reaction of methane and steam to carbon monoxide and hydrogen. Typical operation temperatures vary between 700 °C and 1100 °C at pressures of up to 100 bar. The stoichiometry of the formation of synthesis gas can be expressed by the following equation:

$$\mathrm{CH_4 + H_2O \rightleftharpoons CO + 3H_2}, \;\; \Delta \mathrm{H} = +206.2\,\mathrm{kJ/mol} \tag{2.1}$$

To the produced synthesis gas, watergas shift reaction is applied, in order to further increase the hydrogen yield. The aim of this step is mainly to strip oxygen from the steam molecules by providing the reaction partner carbon monoxide. With the use of suitable catalysts and suitable operation conditions, C-O bounds are energetically favored over C-H bounds, hence the oxygen is stripped from the steam molecule and passed to the carbon-monoxide to form $\mathrm{CO_2}$ molecules, leaving hydrogen as byproduct.

$$\mathrm{CO + H_2O \rightleftharpoons CO_2 + H_2}, \;\; \Delta \mathrm{H} = -41.2\,\mathrm{kJ/mol} \tag{2.2}$$

Since this reaction is moderately exothermal, it increases the overall efficiency of the steam reformer, reaching hydrogen yields of up to 80% in large reformers [9]. Obvi-

ously, the formed CO_2 has the disadvantage of either being released to the environment as greenhouse gas emission or of creating the need for sequestration by means of highly expensive and energetically inefficient Carbon Capture and Sequestration (CCS) methods. In the final step of the steam reforming cycle, unconverted impurities such as CH_4 and CO in the effluent gas are removed usually by means of a Pressure Swing Adsorption device (PSA). In the recent years, much effort was put into the design of steam reformers, in order to reduce the greenhouse gas emissions. However, the potential of reducing the CO_2-output of a steam reforming cycle is limited by the fact that about 74.8% of the CO_2-emission is linked to the chemical reaction of the process itself [10]. According to a life cycle analysis conducted by Ozbilen et al. [11], the net greenhouse gas emissions of hydrogen production by steam reforming of natural gas amount to 12 kgCO_2-equivalents per kg H_2 produced. Apart from all aspects related to emission of CO_2, hydrogen gained from refining processes still may contain some amounts of CO even after purification [12], leading to a poisoning of catalytic surfaces that are mandatory for the functionality of fuel cells.

2.5 Renewable sources for hydrogen production technologies

The hydrogen production technologies discussed above all focus on separating elementary hydrogen from hydro-carbonaceous sources. Alternatively, hydrogen may also be separated from water by means of mainly two methods, namely photocatalytic water splitting and water electrolysis. In the case of photocatalytic water splitting, water can be directly converted to H_2 and O_2 with zero CO_2 emission by using sunlight illumina-

tion in aqueous electrolytes [12]. Beside the drawback of required temperatures higher than 2200 °C, which are necessary to dissociate water at a decent conversion rate, said method is still in its infancy with currently little relevance for an industrial-scale application [12, 13]. The more competitive method for producing hydrogen from an aqueous feedstock is water electrolysis. Here, a current is passed through water by means of two electrodes for the purpose of splitting the $\mathrm{H\text{-}O}$ bounds, hence the formation of elementary oxygen and hydrogen:

$$2\mathrm{H_2O} + \text{direct current electricity} \rightleftharpoons 2\mathrm{H_2} + \mathrm{O_2} \tag{2.3}$$

In recent years, a wide range of different electrolyzers had been suggested and realized in industrial-scale applications. Most common types of electrolyzers are alkaline electrolyzers, followed by polymer electrolyte and solid oxide electrolyzers [14]. The electrolysis process comprises a similar dilemma as the combustion of hydrogen itself: the process itself proceeds without the emission of $\mathrm{CO_2}$, but the resources needed for maintaining the process are possibly linked to a considerable amount of $\mathrm{CO_2}$-emission. In the case of water electrolysis, the produced hydrogen inherits the $\mathrm{CO_2}$-footprint from the applied source of electrical energy. In fact, if hydrogen is produced by water electrolysis, wherein the electric energy for the electrolysis originates from a typical Rankine or Brayton cycle, the greenhouse gas emissions in most cases accumulate to a worse $\mathrm{CO_2}$-footprint as if the hydrogen was produced by steam reforming of methane [14].

In the context of finding energy-storage solutions, the utilization of clean wind energy has been proposed in numerous studies during recent years in the context of buffering energy from periods where the electric grid is over-charged by using this energy for water electrolysis, hence for the production of hydrogen. The latter solution is free of

intrinsic CO_2-emissions. However, due to the numerous energy conversion steps, this concept still requires substantial improvement until it provides a mature hydrogen production platform.

2.6 An alternative path for a clean hydrogen production technology

Previous outline of current hydrogen production technologies indicates that there is a gap between current greenhouse-gas emitting steam reforming cycles and renewable sources that are not yet being realized to an extent where a reliable production of hydrogen can be based on. The currently considered scenario envisaging hydrogen production by electric energy from wind turbines as a short term buffer of otherwise surplus electric energy is lacking a reliable on-demand hydrogen production scheme for an industrial-scale supply of hydrogen energy. However, the latter is mandatory for the implementation of hydrogen in the energy market in medium and long-terms and in particular with respect to the outlines of the IEA.

To fill the technological gap of medium and long-term hydrogen production technologies without intrinsic formation of CO_2, it appears to be most promising using the - compared to water- thermodynamically preferred source of fossil hydrocarbons, particularly methane, and to establish a feasible, clean hydrogen separation method. Such a process has been identified as thermal decomposition of methane, or thermo-catalytical decomposition of methane in case a catalyst is present during the reaction. The already scientifically proven, but technically challenging process for hydrogen production by thermal decomposition of methane has a compelling potential. Thermal decomposi-

tion of methane is a moderately endothermic process, in which hydrogen is stripped off of molecular hydrocarbons during a pyrolytic reaction, starting theoretically already at 300 °C, as a consequence of the free Gibbs energy favoring elementary hydrogen and carbon above said temperature [15]. If pyrolytic conditions are applied, only hydrogen, solid carbon and intermediate hydrocarbons are formed. In summary, the key advantages in light of the previously described production technologies and fields of hydrogen application may be defined as follows:

- Cheap and abundant methane gas as feedstock, yet without intrinsic formation of CO_2 or other greenhouse-gases
- Only hydrogen, solid carbon and only minor amounts of intermediate hydrocarbons are formed as products of the reaction; no CO or CO_x impurities are present in the post-reaction gas mixture
- Nano-carbon may possibly be further marketed, as well as gaseous intermediate reaction products
- Only heat is required for the reaction to proceed, allowing to integrate the TDM-process into either a solar thermal power plant, particularly into a CSP[4] system, or any heat source available

Despite the fact that hydrogen produced from thermal decomposition of methane comprises substantial advantages compared to processes known from prior art, thermal decomposition of methane is not utilized on an industrial scale for hydrogen production. In recent years, numerous laboratory-scale studies had been investigating said process

[4]CSP: Concentrated Solar Power systems utilize concentration means such as mirrors and/or lenses for concentrating solar radiation in a predetermined area, usually the surface of a receiver, at which the concentrated solar radiation is converted into heat.

as an alternative route of hydrogen production. However, it turns out that although the reaction appears comparably simple, a continuously operating cycle so far has never been documented for several reasons, which will be discussed in the following sections of this chapter.

2.7 State of the art in the field of thermal decomposition of methane

2.7.1 Survey on hydrogen production experiments

Studies aiming towards a hydrogen production process by thermal cracking of methane are usually in the context of a specific heat source, to which the envisaged reactor is designed. Concentrating solar thermal power is by far the predominant form of energy suggested in the majority of studies from research institutes in Germany, Spain, Switzerland, USA, France, Canada, Qatar, Israel and others. Other heat-source oriented studies suggested to apply microwave heating to a volume of methane [16, 17, 18], or plasma heating [19, 20, 21, 22, 23]. Independent from the designated heat source, various reactor types have been investigated by electric heating in order to identify the ideal reactor design for a continuously operable plant. Key issues were found to be the handling of high temperatures of more than 1200 °C, in terms of avoiding the utilization of catalysts and the formation of solid carbon as byproduct of the pyrolysis reaction. As a matter of fact, existing concepts of gas-phase reactors with and without solids in packed-bed or fluidized-bed arrangements all show a high risk of an irreversible reactor blockage

due to solid carbon formation [24][5], [5][6]. Solid carbon, formed during the conversion of methane, was also reported to weaken the active surface of non-carbonaceous catalysts in the reaction zone [25][7], [26][8], [27][9].

As proposed by Serban et al. [5], liquid metal bubble column reactors have the potential of operating at very high temperatures with a good heating characteristic due to the large specific gas-liquid interface. Furthermore, because of the lower density of carbon compared to liquid metals, the carbon produced is expected to float atop of the liquid metal surface which results in a reaction zone inside the liquid metal that is not influenced by the carbon formed during operation. Based on the findings of Serban et al. [5], the utilization of a liquid metal bubble column reactor incites expectations to realize an efficient and continuously operable plant for hydrogen production by thermal decomposition of methane. However, so far no further investigations of liquid metal based reactors have been performed. Since the publication of Serban et al. [5], the only activity considering such a reactor type is the work of Paxman et al. [28] and further from current study [29]. Serban et al. [5] used a tube reactor partly filled with liquid metals as bubble column reactor; reporting heavy carbon formation during the experimental runs with run times of several hours. Carbonaceous materials with a high surface area are expected to have a strong catalytic impact on the thermal decomposition reaction of methane [30, 26, 31, 32, 33]. Therefore, if the carbon formed during the reaction has a high surface area, the possibility exists that methane decomposition in hot blank reactor

[5]Rodat et al. [24]: the tubes started to block because of carbon deposition. The experiment was then stopped.

[6]Serban et al. [5]: There is no other mechanical or chemical method for removing the carbon accumulated inside the porous structure other than by burning it.

[7]Abanades et al. 2012: Coke formation on the surface of the catalyst is the main reason for their deactivation [25]

[8]Dunker et al. 2006: For a commercially viable process, it will be necessary to restore the activity of the catalyst by some means [26]

[9]Shah et al. 2001: The efficient removal of the carbon from the catalyst surface in the form of nanotubes is believed to be the key factor influencing catalyst performance. [27]

sections is catalysed by the byproduct carbon.

2.7.2 Survey on methane decomposition kinetics

In the context of own experiments described later, a numerical model has been developed, covering the thermal and chemical behavior of the methane gas flowing through the reactor including parasitic hot zones upstream and downstream of the liquid metal volume. For the chemical part of said model, it is mandatory to make use of existing kinetic data that allows a quantitative prediction of the methane conversion during a given thermal decomposition reaction. In order to model the kinetics of thermal decomposition of methane, several reaction mechanisms had been suggested and experimentally validated in the past. Whereas the detailed reaction mechanism is very complex and not yet fully understood, most authors agree over the stepwise dehydrogenation forming ethane in the first, ethylene in the second, acetylene in the third stage of decomposition, which was first proposed by Back et al. [34].

$$2\mathrm{CH_4} \overset{-\mathrm{H_2}}{\rightarrow} \mathrm{C_2H_6} \overset{-\mathrm{H_2}}{\rightarrow} \mathrm{C_2H_4} \overset{-\mathrm{H_2}}{\rightarrow} \mathrm{C_2H_2} \overset{-\mathrm{H_2}}{\rightarrow} 2\mathrm{C} \tag{2.4}$$

Although this simplified stepwise model proved not detailed enough for a complete explanation of the reaction kinetics [15], it is still widely accepted as the fundamental reaction path. In the following, various data proposed in the literature will be discussed briefly. A graphical comparison thereof is provided within fig. 2.2 below.

Kassel [35] found that the initial methane decomposition reaction is homogeneous and of a first order reaction, which he claims to be heavily retarded by hydrogen. He sug-

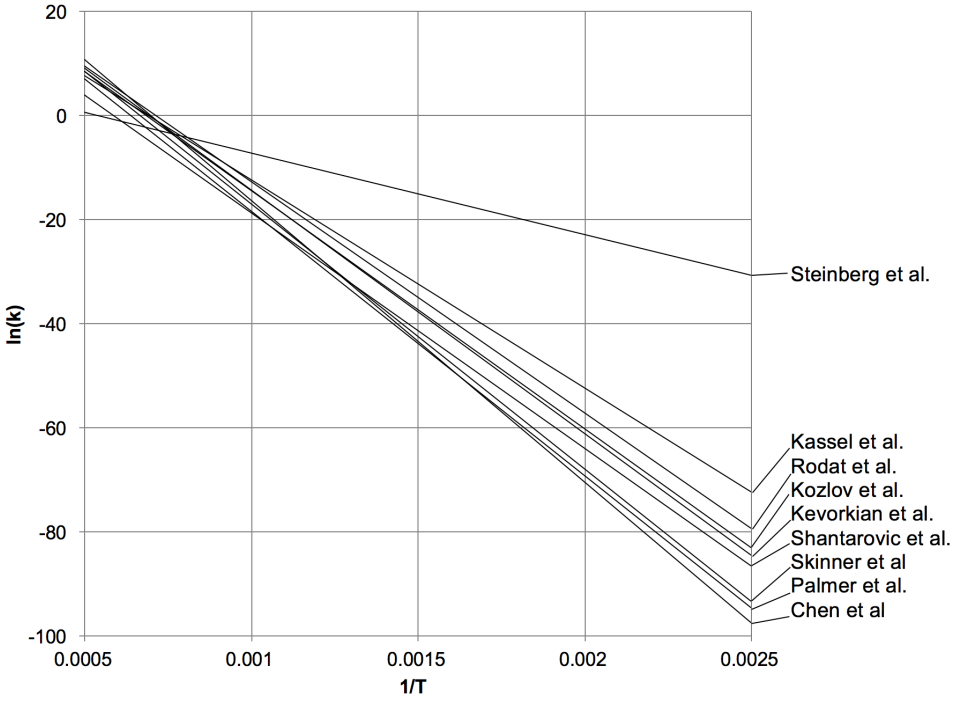

Figure 2.2: Arrhenius plot using kinetic constants proposed by different Authors

gests the stepwise dehydrogenation according to equation 2.4 and assumes the reaction mechanism to be reversible in all single reaction steps. Although Kassel et al. [35] assumes a homogeneous reaction, he found that hydrogen and carbon have been the only products of importance, which in return could have led to a heterogeneous reaction with formed carbon acting as catalyst. Based on experiments conducted in a stainless steel shock tube, Skinner et al. [36] confirms the first-order assumption stated by Kassel et al. [35], he claims however that the methane decomposition is not retarded by hydrogen. Kevorkian [37] also used a shock tube reactor for his experiments. In his study, he suggests a reaction mechanism with an opening step similar to Kassel et al. [35], but with an additional decomposition of methane into methylene radicals and an exothermic inhibition reaction. Steinberg et al. [38] used a tube reactor at very high pressures of 28 to 56 bars for his investigation. Surprisingly, although he applied low temperatures and high pressures, his results point to a very low activation energy of

only 131 kJ/mol; an indicator of relatively fast reaction rates. Compared to experiments conducted with shock tubes, his applied residence times were longer to the factor of $1{\cdot}10^5$; hence the probability of formed carbon catalysis is likely to have influenced his findings. A similar approach was presented by Rodat et al. [24], who coupled experiments using a tubular reactor with a numerical calculation of the conversion. He also found that the methane decomposition reaction is of first-order and mentions a possible heterogeneous reaction at the reactor wall to be likely, which was not represented in the used model however. Most available kinetic data was gathered experimentally and fitted to a rather narrow range of reaction temperatures T_R, educt gas concentrations c_i of a reactant i and applied pressure p_R in a set of experiments, conducted with or without the consideration of catalysts. This spread in experimental parameters and the fact that the used reactors differ in type, dimensions and surface material, a comprehensive correlation is difficult to be found based on existing data. Focusing on kinetic data for the decomposition of methane without the consideration of additional catalysts, several kinetic studies have been considered useful for the herewithin investigated range of operational parameters. For any reaction order, the reaction rate of the reactant $\mathrm{CH_4}$ is defined as

$$-r_{\mathrm{CH_4}} = k_0 \cdot e^{\left(\frac{-E_a}{\Re \cdot T}\right)} \cdot \Pi_i c_i^{n_i} \tag{2.5}$$

The majority of the authors consider the decomposition of methane to occur in a first-order reaction with pre-exponential factors ranging between $5.39{\cdot}10^3$ 1/s and $2.82{\cdot}10^{16}$ 1/s and activation energies in the range of -131 kJ/mol to -450 kJ/mol for our selection of authors. Depending on the applied kinetic data, the conversion results differ to a great extent. False conversion prediction calls for a detailed discussion of the used kinetic

data. As explained in chapters 6, the envisaged reaction temperature is in all cases equal or below 900 °C. In general, thermal decomposition of methane is an endothermic reaction with a minimum reaction starting temperature of about 300 °C at ambient pressure. Full conversion of methane occurs at temperatures above 1200 °C in case the thermodynamic and kinetic prerequisites are fulfilled [6]. The overall methane decomposition reaction according to equation 1.1 has a volumetric expansion factor of $\epsilon = 1$; therefore, increasing the pressure shifts the equilibrium in favor of the educt methane, whereas a lowered pressure shifts the equilibrium in favor of the products. Consequently, high temperatures, low pressures and long residence times favor methane decomposition into lighter hydrocarbons and ultimately hydrogen and carbon. It is hardly possible to extract a common correlation from the literature data, due to the dissimilarity of the individual kinetic sets. However, literature data shows the tendency towards higher methane conversions for data, gained from experiments conducted in the presence of carbon. Table 2.1 is based on a table provided first by Wullenkord [15] and presents a summary of the discussed kinetic data which will be applied to the numerical model and compared with own experimental results in chapters 7 and 8.

Ref	Reactor	Reaction	Temp [K] T_R	Pressure [bar] p_R	Conc. [vol-%] c_i	Res. time [ms] t_{res}	Order - n_i	Pre-exp. F. $\left[\frac{1}{s}\right]$ k_0	Act. En. $\left[\frac{kJ}{mol}\right]$ E_a
Kassel et al. [35]	Quartz Tube	$CH_4 \rightarrow CH_2 + H_2$	973-1123	0.017-0.51	100	5-40 min	1	$1 \cdot 10^{12}$	-332.4
Skinner et al. [36]	Shock Tube	$H + CH_4 \rightarrow \rightarrow CH_3 + H_2$	1430-1785	5.1	100	15	1	$5.13 \cdot 10^{14}$	-422.9
Kevorkian et al. [37]	Shock Tube	$CH_4 \rightarrow$ Products	1656-1965	3.4-12	2-10	0.5-0.1	1	$1.32 \cdot 10^{14}$	-389.4
Shantarovic et al. [39]	Ceramic Tube	$CH_4 \rightarrow$ Products	1566-1646	0.023-0.027	0.8-0.05	5-42	1	$3.98 \cdot 10^{11}$	-376.8
Kozlov et al. [40]	Shock Tube	$CH_4 \rightarrow$ Products	1670-2050	2.0-8.1	0.5-0.2	-	1	$4.4 \cdot 10^{13}$	-381
Palmer et al. [41]	Annular Reactor	$CH_4 \rightarrow$ Products	1163-1351	-	-	-	1	$1.26 \cdot 10^{14}$	-422.9
Chen et al. [34]	Quartz Tube	$CH_4 \rightarrow CH_3 + H$	995-1103	0.033-0.99	0.01	2.5	1	$2.82 \cdot 10^{16}$	-450.5
Steinberg et al. [38]	Tube Reactor	$CH_4 \rightarrow C + 2H_2$	973-1173	28.6-56.8	0.01	103s	1	$5.4 \cdot 10^{3}$	-131
Rodat et al. [24]	solar reactor	$CH_4 \rightarrow 2H_2 + C$	1500-2300	4kPa	0.2-0.5	12-35	1	$6.6 \cdot 10^{13}$	-370

Table 2.1: Overview of relevant literature considering thermal decomposition of methane into various products without the use of catalysts

Chapter 3

Liquid metal for thermal decomposition of methane

► The following chapter documents the process of identifying the most suitable reactor concept for a TDM process comprising a liquid phase as heat transfer medium.

Previous chapter pointed out that most of the available reactor proposals related to thermal decomposition of methane for hydrogen production are lacking a continuously operable reactor concept. This is mainly related to the problem of carbon accumulation on solid surfaces within the reactor, particularly on sites where heat is transferred to the pyrolysis gas. Since the hottest spot is in most cases located directly at the solid surface, conversion of methane occurs right on the surface as well, along with the formation of carbon atop of the surface. To overcome this problem, it appears advantageous to replace static heat transfer surface structures with a dynamic liquid-gas interface, where the liquid phase serves as heat transfer medium. By means of such a dynamic

liquid-gas interface, two effects are expected to be observed. First, a more efficient heat transfer to the pyrolysis gas due to the increased surface area. Thus, the heat transfer area is increased, and therefore, the time needed for gas heat-up inside of the reactor is reduced. Second, the liquid phase provides a dynamic liquid-gas interface without surface-adhesion of solid carbon that is formed as a TDM by-product during the methane conversion.

In view thereof, a liquid-gas system seems promising for realizing a continuously operable TDM process. With respect to the challenging operation conditions of a two-phase reactor for thermal decomposition of methane, several requirements for candidate liquids have been found to be relevant, for instance a

- low melting point for simplified handling during idle times;
- high boiling point, as the TDM reaction requires operation temperatures of up to 1000 °C or even above;
- good heat transfer characteristics, namely high thermal conductivity, for an optimized heat-up of the pyrolysis gas;
- good wettability with the gas dispersion device for good bubble/droplet formation;
- low solubility of metal components in the liquid to minimize steel corrosion attack;
- low cost and abundant availability;
- non-toxic material;
- little or no reactivity when exposed to air or oxygen;
- catalytically active material for increased reactor performance; and

- existing operational experience.

Due to the above stated requirements, the range of considered liquids is reduced to pure metals or metal alloys in liquid state. In the following chapters, the term “Liquid Metal” does not refer to specific sorts of metals, but rather refers to the liquid state of a given metal or alloy of metals. Liquid metals have been investigated in terms of applicability as heat transfer fluids since the beginning of the development of nuclear reactors in the 1940’s and 1950’s and are now still under investigation for various applications in nuclear reactors and also for applications in the field of solar thermal power. However, the utilization of liquid metals as direct contact medium in chemical processes has rarely been suggested.

3.1 Candidate liquid metals for the TDM process

Because the application of liquid metals as heat transfer medium for the TDM process requires an operation at temperatures in the range of 750 °C to 1000 °C, or even higher temperatures, typically suggested candidates for lower temperature processes are alkali metals such as Li, Na, K and also the alloy Na-K. Mainly for reasons of handling safety, in particular because of their high reactivity with oxygen, the latter metals have been discarded from consideration for the application of thermal decomposition of methane. Even though oxygen is not a reactant, oxygen impurities must not lead to a critical operation condition of the reactor. More specific, a reactor operated with Li, Na or K or combinations thereof will, in the case of an unforeseen leakage, be in the risk of causing a catastrophic event. From the spectrum of all metal compounds, transition metals and alloys of such are usually excluded from consideration as heat transfer flu-

ids, simply due to their very high melting points which are usually above 1000 °C. Apart from mercury, the lowest melting transitional metals are Cadmium and Zinc, melting at 320 °C (Cd) and 419.5 °C (Zn); which would be acceptable for the TDM process. Both of those two transition metals however boil at comparably low temperatures, namely 765 °C in the case of Cd and 907 °C in the case of Zn at ambient pressure. The same applies for mercury with a boiling point of 356.85 °C.

From the heavy metal candidates, Sn, In, Ga as well as the alloy Ga-In-Sn comprise low melting points, namely 232 °C (Sn), 157 °C (In), 30 °C (Ga) and 11 °C (GaInSn), and boiling points higher than 2000 °C, while Pb, Bi and Pb-Bi have boiling points in the range of 1533 °C (Pb-Bi) to 1743 (Pb) at ambient pressure. High boiling points correspond to a low vapor pressure at operation temperatures, hence low amounts of metal elements in the gaseous phase. As an example, at 750 °C, the vapor pressure of Pb exceeds the one of Sn by three orders of magnitude. High vapor pressures lead to undesired metal condensation and partial formation of particles in gas lines down-stream of the reactor volume, requiring expensive filtering devices especially if the generated metal vapor is toxic. Toxic metal condensation and particles might also lead to a contamination of the products, hence requiring additional purification steps.

In light of the above stated requirements, liquid tin was identified as the best candidate metal, since it meets the constraints of high availability, low cost, low vapor pressure at operation temperature and is non-toxic. In terms of the physical property requirements, liquid tin has a dynamic viscosity close to that of water and a thermal conductivity of 33.8 W/(m K) at 600 °C. Quantitative statements regarding solubility of metal components in liquid tin are challenging due to the very little available information, especially for temperatures above 600 °C. In fact, existing literature indicates that liquid tin is one of the most aggressive liquid metals in terms of compatibility with ferrous, non-ferrous

and in parts non-metal materials. Similar to the inter-metallic corrosion chemistry, the assessment of catalycity of tin with respect to the TDM process is hard to predict, due to the lack of available data. In the work of Serban et al. [5], a possible catalytic activity can be derived from the experimental results which will be discussed in the subsequent chapter.

3.2 Applying liquid metal to the TDM process

The presence of a liquid media was found by Serban et al. [5] to have a considerable potential for realizing a continuously operating process of thermal decomposition of methane. It was further identified in the previous section of this chapter that on the basis of a comparison of several liquid metals, the utilization of liquid tin seems to be the most promising option. What needs to be identified is the ideal reactor setup for the interaction of liquid tin and the pyrolysis gas methane.

As shown in fig. 3.1, which is based on an illustration provided by Mersmann et al. [46], a great variety of existing two-phase reactors is known in the field of process engineering. In most cases, the two phases are provided in a counter-flow configuration, particularly if both fluids are reactants. In the case of thermal decomposition of methane, the liquid phase does not participate in the reaction, but is rather used as heat transfer medium and possibly as catalyst. Accordingly, there is in principle no necessity to circulate the liquid if not for a dispersion of it.

The spectrum of technologies for managing the two-phase interaction can be subdivided into two major groups. The first group comprises a liquid as disperse phase and gas as the continuous phase, whereas the second group comprises a liquid medium as con-

tinuous phase and a gaseous medium as the disperse phase. The first group requires atomizing the liquid into droplets or spray. Common technologies for fluid atomization, known in this field of study are for example pressure driven atomization means, gas flow driven atomization (airblast atomizer) means or rotation driven atomization means. The common principle of aforementioned atomizers is to apply sheer stresses to the liquid, whereas high sheer stresses lead to small droplets and vice versa. In chemical engineering, a selection of typical reactor types is shown in fig. 3.1. Among those, reactors belonging to the first group are plate column reactors (type I in 3.1), spray tower reactors (type II in fig. 3.1) and Venturi scrubbers (type V in fig. 3.1), using either nozzles, gravitational force or gas flow driven atomization means for atomizing the liquid. Plate column reactors (type I in fig. 3.1) usually comprise a sharp step or edge, at which the liquid is sheared off by gravitational forces. Such reactors however have a poor atomizing performance in terms of gained liquid-gas surface, due to the comparably weak sheer stresses that are resulting from gravitational force. Venturi scrubbers (type V in fig. 3.1) atomize the liquid by means of fast gas flows, usually air, to sheer off the liquid media from from a sharp edge, in order to form droplets. In a Venturi scrubber (type V in fig. 3.1), the high gas velocities and therefore the small gas residence times make them generally unattractive as a useful device for a reactor utilized for thermal decomposition of methane. Spray towers (type II in fig. 3.1) use pressurized nozzles to sheer off the liquid phase at the edges of small orifices. Alternatively, liquid may also be dropped into the reactor using gravitational force only. From the above introduced range of two-phase reactors comprising the liquid as disperse phase, spray towers seem to be most practical.

In the second group, the reactor comprises liquid tin as continuous phase, whereas methane is dispersed into the liquid. The most basic design of the second group of

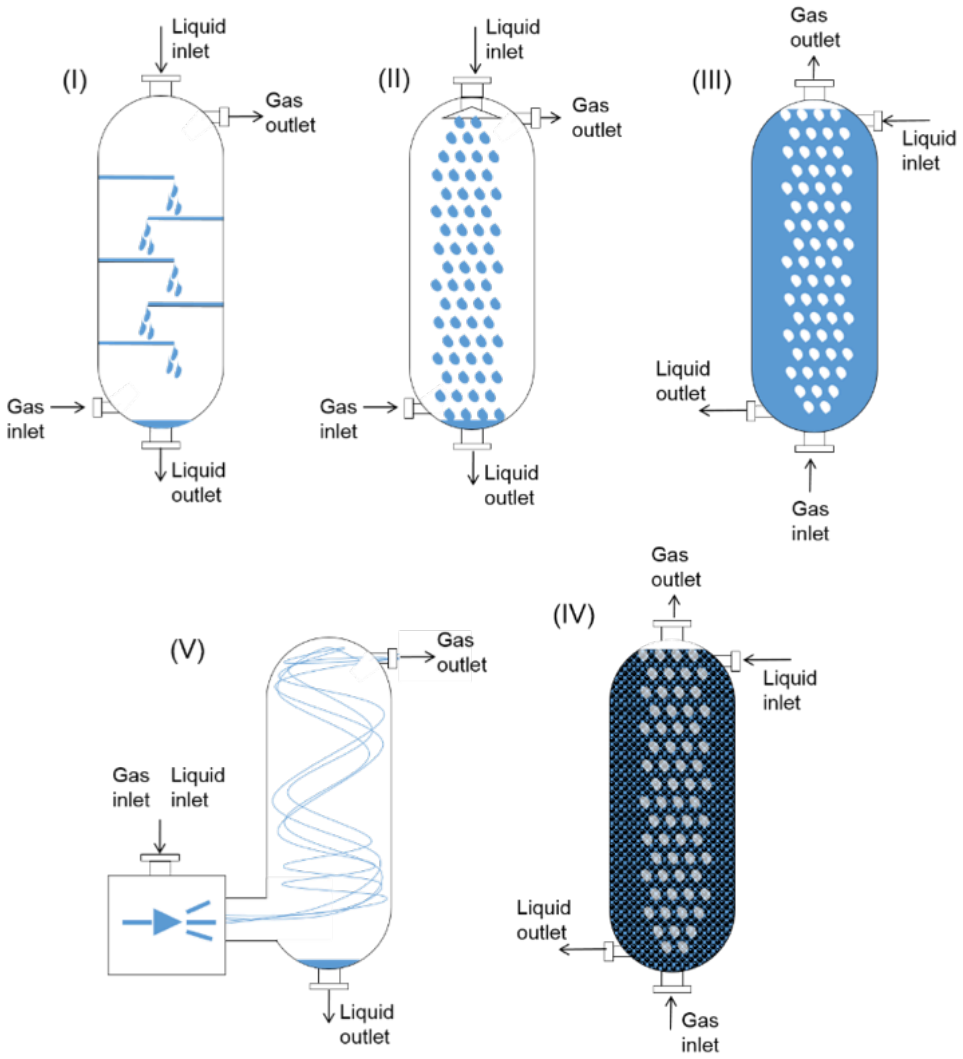

Figure 3.1: Overview of commonly used liquid-gas reactors in process engineering [46]

gas-liquid reactors is the bubble column reactor (type III in fig. 3.1) which mainly consists of a tank and at least one submerged gas injection means. In most applications, bubble column reactors are designed as counter-flow devices, wherein additional to the upward-flow of the disperse gas, a downward-flow of the liquid phase is imposed on the liquid. A wide range of different embodiments of bubble column reactors has been suggested for an even wider range of applications. Moreover, in a further embodiment of a bubble column reactor, additional installations may be submerged into the continuous

liquid phase of a so-called packed-bed bubble column reactor (type IV in fig. 3.1), such as solid packings in various shapes. Also, deviation plates or mixing devices that are suspended on the reactor top are known. All of the inserted and submerged installations have the objective to increase the residence time and also the surface area of the disperse and continuous phase for heat and mass transfer purposes. The question to be answered is which of the two above-mentioned options, namely tin being dispersed into methane or methane being dispersed into tin, are to be favored for the process of thermal decomposition of methane.

3.3 Spray tower vs. bubble column reactor: Comparison of the practicability for the process of TDM

As outlined in the sections before, among all considered multi-phase reactor types, two technical options seem to be most promising for the realization of a continuously operating TDM process in the presence of liquid tin as heat transfer medium, namely a spray tower type reactor and a bubble column type reactor. Within this section, an evaluation shall be provided, discussing the advantages and disadvantages of both options if utilized for the TDM process. For this purpose, four key questions have been defined as follows:

1. **Two-phase flow phenomena:** Which reactor configuration features the better two-phase flow characteristic?
2. **Conversion performance:** Which reactor configuration provides the higher theoretic conversion results?

3. **Influencing the operation conditions:** Which reactor configuration qualifies for controlling the chemical operation conditions, mainly temperature and gas residence time during operation?

4. **Carbon removal potential:** Which reactor configuration provides better carbon removal possibilities during operation?

With respect to subsequent experimental chapters and also the chemical limitations of the TDM process, the following assessment will discuss a liquid-gas composition comprising liquid tin and pure methane gas, following the ideal gas law. Considered temperatures will be in the range of 300 °C - 1000 °C. For the defined temperature range, the change in liquid tin properties are considered within the calculations. In this context, the density of liquid tin ρ_{Sn} will be calculated using a correlation proposed by Alchagirov [42], covering the temperature range from the melting point 232 °C up to about 1600 °C.

$$\rho_{\mathrm{Sn}}(T) = 7374.7 - 0.6765 \cdot T \quad (\mathrm{T(K)}; \mathrm{kg/m3}) \tag{3.1}$$

The surface tension σ_{Sn} of liquid tin for temperatures lower than 1000 °C was found by Alchagirov et al. [43] to be

$$\sigma_{\mathrm{Sn}} = 551 - 0.09 \cdot (T - 505.05) \quad (\mathrm{T(K)}; \mathrm{mN/m}) \tag{3.2}$$

Dynamic tin viscosity η_{Sn} properties are taken from Assel et al. [44]

$$\eta_{\mathrm{Sn}} = 10^{(-0.408+343/T)} \quad (\mathrm{T(K)}; \mathrm{mPa \cdot s}) \tag{3.3}$$

For a concise overview of the subsequent comparative calculations, table 3.1 provides liquid tin properties calculated for several reference temperatures on behalf of above

listed equations.

	Temperature	Density	Dynamic viscosity	Surface tension
		ρ	η	σ
		$[\mathrm{kg/m^3}]$	$[\mathrm{mPa \cdot s}]$	$[\mathrm{mN/m}]$
Sn	300 °C	$6.9 \cdot 10^3$	1.6	545
	600 °C	$6.7 \cdot 10^3$	1.0	518
	900 °C	$6.6 \cdot 10^3$	0.8	490
CH_4	900 °C ($p = 2\mathrm{bar}$)	0.33	$1.12 \cdot 10^{-5}$	

Table 3.1: Applied fluid properties at various reference temperatures

3.3.1 Gas-liquid system

From a fluid dynamics point of view, both options may be discussed equally on the basis of dispersing fluid A in a continuous fluid B. Thus, in the case of a bubble column reactor, methane is dispersed into the continuous fluid liquid tin and in the case of a spray tower, vice versa, tin is dispersed into the continuous fluid methane. In both cases, the heat flux is directed from the liquid tin to the gas phase. Therefore, methane conversion is predominantly triggered at the boundary of disperse and continuous phases. As a result, if carbon is formed at this location and time, solid carbon is flushed from the phase boundary surface atop of the liquid surface, where carbon accumulation is desired and may be treated during subsequent processing steps. Fig. 3.2 provides a schematic illustration of a spray tower (left) in comparison with a bubble column (right) reactor. The disperse phase, defined by the entity of all fluid particles, is referred to with the index d, wherein the continuous phase is indexed c. In this context, the term "fluid particle" relates to both liquid droplets and gas bubbles. In fact, both particle forms may validly be described with the same formulas. Here it is only distinguished between the disperse and continuous phase. For changing the disperse phase into the continuous phase and vice versa, only the properties of both liquids need to be swapped.

It is assumed that in both scenarios, any fluid particle is formed at an orifice, from which the fluid particles depart with an initial particle velocity w_0. During the floatation/falling time along the vertical axis Z, each fluid particle is floating or falling with a general velocity $w(Z)$. In the following sections, both of the two competing reactor configurations will be compared on behalf of different aspects.

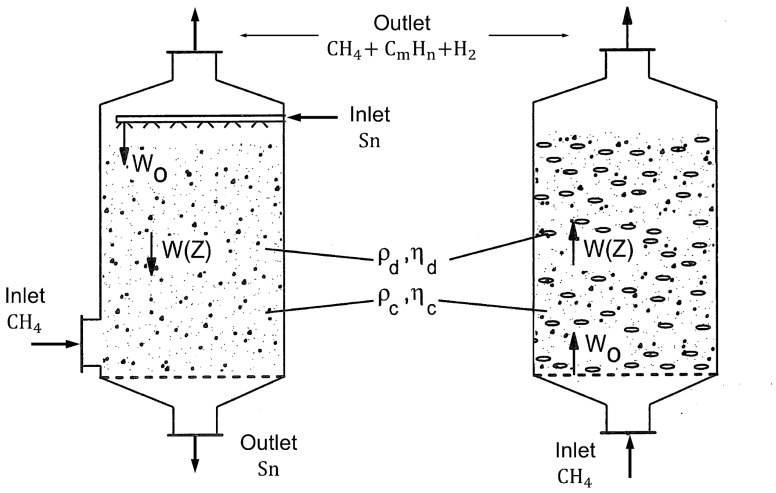

Figure 3.2: Possible reactor configurations for TDM in the presence of liquid tin: Spray tower (left) and bubble column reactor (right). For spray towers liquid tin is dispersed in the continuous fluid methane, whereas for bubble columns methane is dispersed in the continuous fluid tin.[46]

Terminal fluid particle velocities

Many chemical reactor engineering devices utilize one or a plurality of small, usually cylindrical holes, so-called "orifices", to disperse a first phase into a second phase by injection. Said orifices may also be in the shape of tubes, pipes or the like. The flow of the fluid to be dispersed through the orifice may be correlated with the shape of the obtained particle formed during and after the departure of the orifice. For this purpose, the non-dimensional orifice We-number $\mathrm{We_O}$ was defined; showing the ratio of the gas kinetic energy to the surface energy. It is used to predict the behavior of the fluid particle

departing an orifice by taking into account the fluid velocity w_{O} inside the orifice with a diameter d_{O}, as well as the density of the disperse fluid ρ_{d}.

$$We_{\mathrm{O}} = \frac{w_{\mathrm{O}}^2 \cdot d_{\mathrm{O}} \cdot \rho_{\mathrm{d}}}{\sigma} \tag{3.4}$$

For small orifice- We-numbers, $We_{\mathrm{O}} \rightarrow 0$, Mersmann [46] suggests a correlation for linking the gained particle diameter with the physical properties of the continuous fluid along with geometrical dimensions:

$$d = \sqrt[3]{\frac{6 \cdot \sigma_{\mathrm{c}} \cdot d_{\mathrm{O}}}{\rho_{\mathrm{c}} \cdot g}} \tag{3.5}$$

For simplification purposes, the fluid particle is here approximated by a rigid sphere moving in a continuous fluid. The friction forces resulting from the movement of the fluid particle are accounted by the dimensionless drag coefficient C_{D}, balancing the friction force F_W acting on the particle with the forces of dynamic pressure, caused by the particle movement at a velocity w:

$$C_D = \frac{F_W}{\frac{1}{2} \cdot \rho_c \cdot w^2 \cdot A}. \tag{3.6}$$

Here, A is the cross-sectional area of the fluid particle and ρ_c refers to the density of the continuous phase. As can be seen, the drag coefficient depends on the particle shape and the particle velocity. Assuming a terminal velocity w_t, buoyant forces and drag forces are equal. Therefore, the following balance may be stated:

$$C_D \cdot \frac{1}{2} \cdot \rho_c \cdot w_t^2 \cdot A = g \cdot \Delta\rho \cdot V, \tag{3.7}$$

with the force F_W being defined as

$$F_W = g \cdot \Delta\rho \cdot V. \tag{3.8}$$

For a spherical particle, C_D may be transposed according to:

$$C_D = \frac{4}{3} \frac{\Delta\rho}{\rho_d} \frac{g \cdot d}{w_t^2}. \tag{3.9}$$

By means of the Fr-number, which is defined as the ratio of inertia and gravitational forces acting on a floating particle in a continuous fluid, namely

$$Fr = \frac{w^2 \cdot \rho_c}{d \cdot \Delta\rho \cdot g} \tag{3.10}$$

equation 3.9 may be further simplified to

$$C_D = \frac{4}{3 \cdot Fr}. \tag{3.11}$$

On behalf of the Reynolds number Re,

$$Re = \frac{\rho_c \cdot d \cdot w}{\eta_c} \tag{3.12}$$

wherein η_c is the dynamic viscosity of the continuous phase and the Fr-number, both the fluid particle velocity w and its diameter d can be expressed on mutual dependencies as suggested by Mersmann [45]:

$$\sqrt[3]{Re \cdot Fr} = w \cdot \sqrt[3]{\frac{\rho_c^2}{\eta_c \cdot \Delta\rho \cdot g}} \tag{3.13}$$

$$\sqrt[3]{\frac{Re^2}{Fr}} = d \cdot \sqrt[3]{\frac{\rho_c \cdot \Delta\rho \cdot g}{\eta_c^2}} \tag{3.14}$$

In accordance with the above stated equations, a graphical correlation was suggested for applying the introduced equations to existing fluid particle problems. As shown in fig. 3.3, proposed by Mersmann in the year 1977 [45], the ordinate axis covers equation 3.13, whereas the abscissa refers to equation 3.14.

The above depicted graphical correlation shall be used as follows. For instance, a given dimensioned particle diameter is defined and multiplied by the non-dimensionalizing term, shown in fig. 3.3 and equation 3.14. Depending on the flow regimes which are represented within the figure, the corresponding non-dimensional velocity value may be found on the ordinate of the graphical correlation. The value of the found velocity is then obtained from dividing the identified value of the graphical correlation by the non-dimensionalizing term of equation 3.13. The same procedure shall be applied vice-versa for a given dimensional velocity value.

Assuming an operation temperature of 900 °C, an orifice diameter of 1 mm and the material properties of tin and methane according to table 3.1, the Mersmann correlation can be applied to the first scenario, the bubble column reactor. For a considered

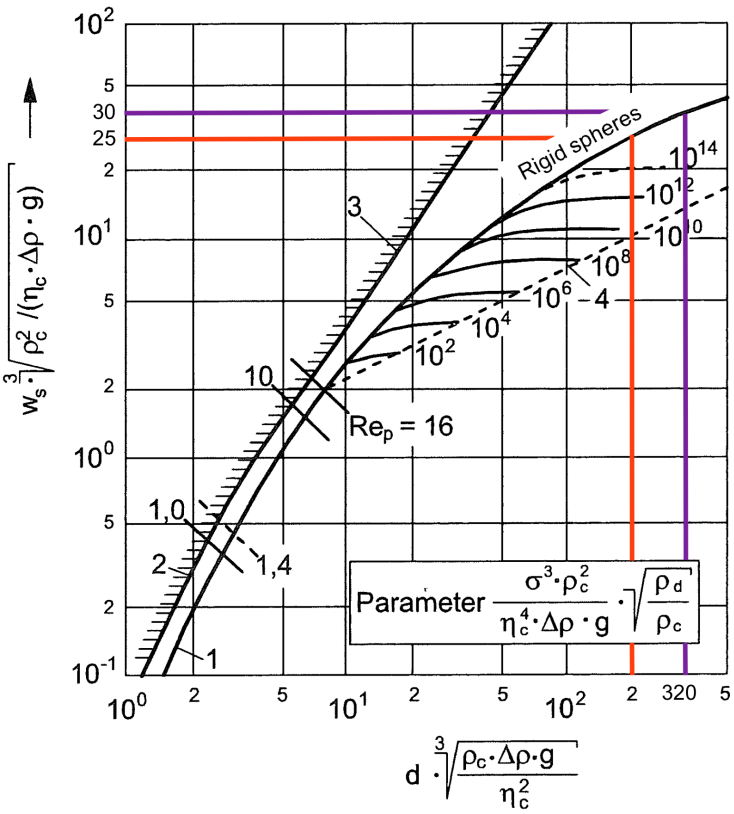

Figure 3.3: Dimensionless terminal rise or sink velocity of solid and fluid particles in relation of the dimensionless particle diameter [46]

gas flow rate in the range between 5 and 200 mln/min, the gas velocity inside of the orifice ranges between 0.2 m/s and 9.2 m/s, further applying ideal-gas law at an absolute pressure of 2 bars inside of the orifice. Due to the high surface tension of tin, the resulting We-number is extremely low, ranging from $3.6 \cdot 10^{-10}$ to $5.7 \cdot 10^{-2}$. Since the condition $We_{\mathrm{O}} \rightarrow 0$ is valid, equation 3.5 may be used for finding the particle diameter, according to Mersmann [46]. The obtained particle diameter yields in 3.6 mm and is independent from the applied flow rate. Now, the dimensional diameter is multiplied by the non-dimensional equation 3.14, which results the value of roughly 320, see the red lines in fig. 3.3. As can be seen from the graphical correlation, the corresponding non-dimensional velocity thereto for rigid spheres yields roughly the value 30. In return, the result for the dimensional particle rise velocity for a methane bubble in liquid tin at

900 °C is about 0.3 m/s.

The same approach shall now be applied to the other scenario, namely dispersing tin into the continuous fluid methane. Again, the We-number needs to be checked. For example, assuming identical orifice velocities in the range of 0.2 m/s to 9.2 m/s as a common value for both scenarios, the results differ to extreme extents. Whereas an orifice velocity of 0.2 results in a We-number of about 0.7, an orifice velocity of 9.2 returns a We-number of $10 \cdot 10^3$. In fact, in order to stay below the critical We-number of 2, which is required to achieve a stable flow of individual particles, the orifice velocity must not be greater than about 0.3 m/s. However, equation 3.5 cannot be used for this scenario. Therefore, as a simplification, it is assumed to have liquid tin particles of the same size compared to the methane particles, namely 3.6 mm. Now, if the equation for the dimensional tin particle is multiplied with equation 3.14, the value 200 is obtained. With reference to fig. 3.3, the corresponding non-dimensional particle velocity is about 25, see also the purple lines in fig. 3.3. During the non-dimensionalization by means of equation 3.13, the terminal tin particle velocity is about 47 m/s.

As a conclusion, according to the correlations above, liquid metal droplets are expected to reach a terminal velocity, that surpasses the velocity of methane bubbles by three orders of magnitude. It is generally required to maintain a maximum of phase boundary interface inside of the reactor with a minimum in effort. In view of the above-referenced results, dispersing tin particles in methane however requires an increase by three orders of magnitude, in order to provide the same amount of particles of the same size inside of the reactor. Thus, dispersing methane into tin is favored according to the above conducted calculations.

Phase boundary interface

In the following section, a further comparative estimation will be presented for the volume fraction of the disperse phase for both the bubble column and the spray tower arrangement. The velocity of the continuous phase is considered zero. ϵ is defined as the volume fraction of the continuous phase, balancing the initial height volume V_0 without fluid particle charge and the resulting volume V in the presence of fluid particles.

$$\epsilon = \frac{V_0}{V} = \frac{H_0}{H} \tag{3.15}$$

Correspondingly, the volume fraction of the dispersed fraction is defined as

$$1 - \epsilon = \frac{(V - V_0)}{V} = \frac{(H - H_0)}{H} \tag{3.16}$$

The velocity of the disperse phase inside a reactor without the continuous phase is defined as the superficial velocity

$$\dot{v}_{\mathrm{d}} = z \cdot \frac{\dot{V}_{\mathrm{d}}}{A} \tag{3.17}$$

where $z \cdot \dot{V}_{\mathrm{d}}$ represents the volumetric flow of the disperse phase [45]. In the case of the bubble column, the density ratio is $\rho_c/\rho_d \approx 2 \cdot 10^4$; in the case of a spray tower arrangement, the density ratio is $\rho_c/\rho_d \approx 5 \cdot 10^{-5}$. In fig. 3.4, a graphical correlation is provided, interrelating the volumetric fraction of the disperse phase ϵ_d with the dimensionless superficial velocity

$$\frac{\dot{v}_\mathrm{d}}{w_\mathrm{t}} = \frac{\dot{v}_\mathrm{d}}{1.55} \cdot \sqrt[4]{\frac{\rho_c^2}{\sigma \cdot \Delta\rho \cdot g}} \tag{3.18}$$

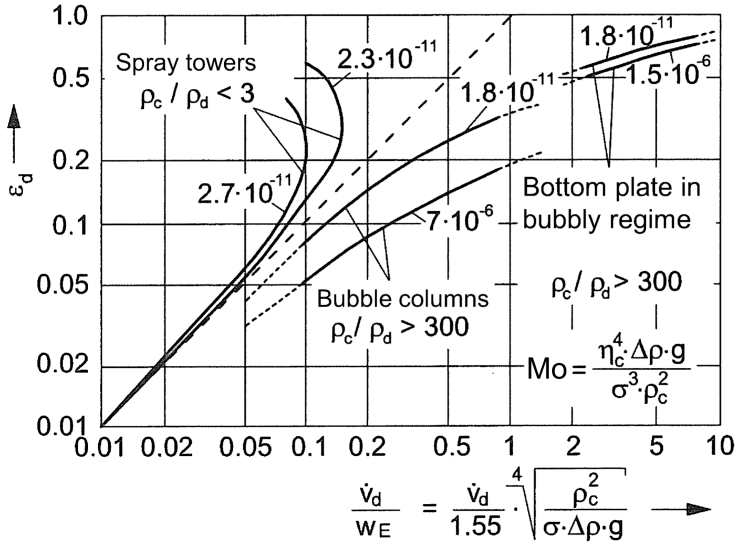

Figure 3.4: Volume fraction of the disperse phase in relation of the parameter $\frac{\dot{v}_\mathrm{d}}{w_\mathrm{t}}$ [46]

Fig. 3.4 shall be interpreted as follows. The volume fraction of the disperse phase is only a function of fluid properties and the applied superficial disperse velocity. Depending on the Mo number

$$Mo = \frac{\eta_c^4 \cdot \Delta\rho \cdot g}{\sigma^3 \cdot \rho_c^2} \tag{3.19}$$

and the density ratio of continuous and disperse phase ρ_c/ρ_d, real systems deviate from the ideal line. The smaller the result of equation 3.19, the smaller is the deviation from the considered fluid-fluid system from the dotted reference line. Inserting an identical superficial velocity for both scenarios, a comparison is possible based on the different results for the dimensionless superficial velocity, as shown in equation 3.18.

For methane-tin systems at a reference temperature of 600 °C and 2 bar, the phase-interaction behaves as follows. The value of the Mo-number for methane dispersion in

liquid tin results in 4.13·10^{-15}. In order to obtain a hypothetical disperse volume fraction of ϵ_d=0.1 in a bubble column reactor, the corresponding dimensionless velocity value of 0.11 needs to be reached. According to fig. 3.4 and equation 3.18, ϵ_d=0.1 corresponds to an applied superficial gas velocity $\dot{v}_{\mathrm{d}}$=3 mm/s.

Now, for spray tower systems, equation 3.19 returns the value 9·10^{-14}. Following the same strategy as for the calculation for bubble columns; in order to obtain $\epsilon_d = 0.1$, a dimensionless superficial velocity of about 0.09 needs to be targeted. Such value is reached for superficial velocities of 45 m/s. Consequently, due to the liquid phases' physical properties, maintaining a defined disperse volume fraction ϵ_{d}, a spray tower type reactor requires a superficial velocity of the disperse fluid four orders of magnitude bigger compared to a dispersion of methane into liquid tin.

The volume related phase boundary interface a is defined by the volume fraction of the disperse phase $1 - \epsilon$ and the Sauter diameter d_{32}. for fluids with a viscosity below 3 mPa·s ($Sn_{600^{\circ}\mathrm{C}}: \eta = 0.77\,\mathrm{mPa \cdot s}$), d_{32} is defined according to Mersmann [45] as follows.

$$d_{32} = 1.8 \cdot \sqrt{\frac{\sigma}{\Delta\rho \cdot g}} \tag{3.20}$$

For both methane and tin as disperse media, equation 3.20 provides a Sauter diameter of 5 mm with less than 10% alteration for the temperature range of 300 °C - 900 °C. According to Mersmann [45], the phase boundary a is defined as

$$a = \frac{6 \cdot \epsilon_{\mathrm{d}}}{d_{32}}\,, \tag{3.21}$$

showing a linear dependency on the disperse volume fraction ϵ_{d}. As a conclusion, from

a fluid dynamics point of view, spray tower systems seem to be less favorable, mainly due to the poor specific phase boundary yield for any operation state compared to a bubble column reactor.

3.3.2 Conversion performance

In chapter 2, the reaction order for the TDM reaction was discussed based on the findings of several studies from different authors. It was found that the majority of authors suggest a reaction order of 1 for a non-catalytic reaction. If catalysts are applied, the resulting reaction orders varied between 0.5 and 2, depending on the used catalyst and the reaction conditions. The fundamental reaction of methane decomposition is volume increasing, with $\epsilon_{\mathrm{CH_4}} = 1$. Typical ideal models of continuous reactors used in chemical engineering, like the ideal plug flow reactor (PFR) and the continuous stirred-tank reactor (CSTR) are helpful for selecting the better reactor configurations in terms of their conversion performance for a given reaction kinetic. An ideal plug flow reactor comprises no radial change in concentration, however concentration changes with the length of the reactor. An ideal CSTR has no concentration gradient whatsoever, the feed flow immediately reaches final concentration. On behalf of mass balances, design equations can be derived for both reactor types and compared by the space time τ for a specific conversion X of a substance A.

$$\frac{\left(\tau \cdot C_{\mathrm{A0}}^{\mathrm{n}-1}\right)_{\mathrm{CSTR}}}{\left(\tau \cdot C_{\mathrm{A0}}^{\mathrm{n}-1}\right)_{\mathrm{PFR}}} = \frac{\left[X_{\mathrm{A}} \cdot \left(\frac{1+\epsilon_{\mathrm{A}} \cdot X_{\mathrm{A}}}{1-X_{\mathrm{A}}}\right)\right]_{\mathrm{CSTR}}}{\left[\int_0^{X_{\mathrm{A}}} \frac{(1+\epsilon_{\mathrm{A}} \cdot X_{\mathrm{A}})^{\mathrm{n}}}{(1-X_{\mathrm{A}})^{\mathrm{n}}} \mathrm{d}X_{\mathrm{A}}\right]_{\mathrm{PFR}}} \tag{3.22}$$

As shown in fig. 3.5, for reaction orders and volumetric expansion factors greater than 0, a PFR reactor requires less space time with increasing effect for reactions of higher

orders and expansion factors [47]. As a conclusion, one can say that mixing of reactants has a negative impact for the TDM reaction, according to ideal reactor models.

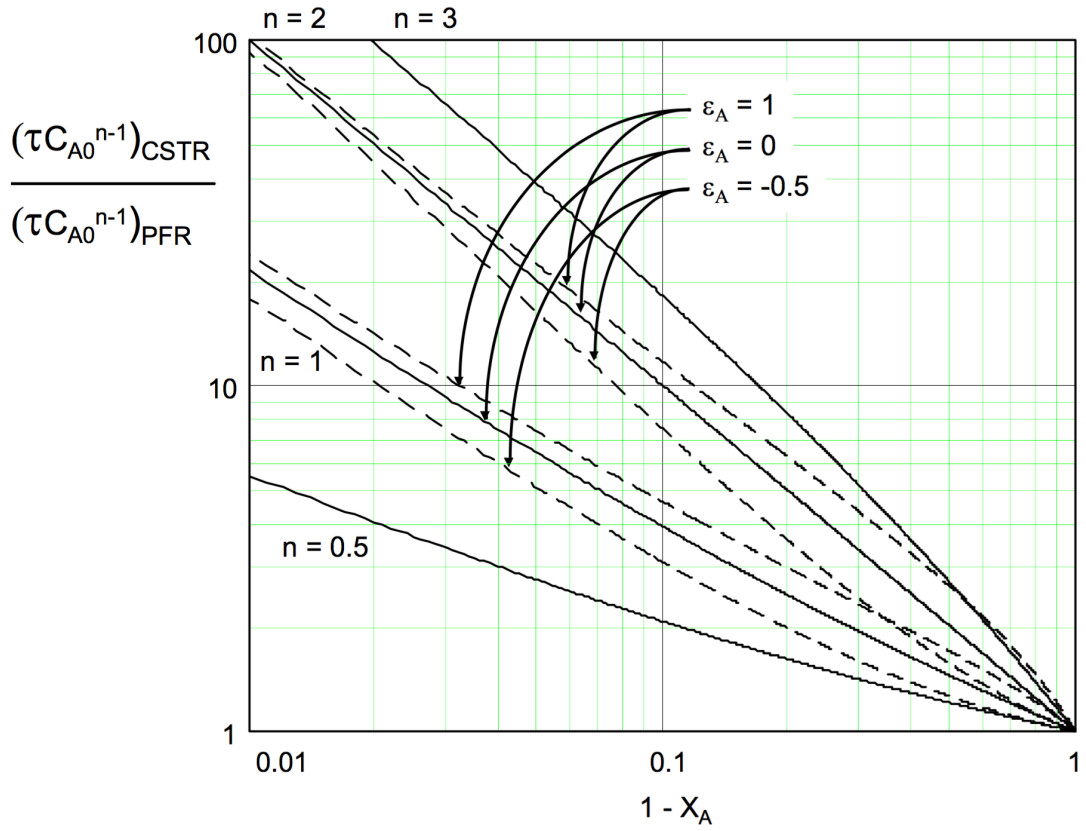

Figure 3.5: Comparison of continuous PFR and CSTR reactors for different reaction orders n and volume expansion factors ϵ [47]

Considering the spray tower and bubble column reactor options, the flow regimes are more complex than the above assumed regimes. However, the bubble column reactor is likely to show less mixing, due to the isolation of single gas volumes from each other. Each bubble entity converts gradually during its climb, similar to a hypothetical gas entity in an ideal PFR. For a spray tower however, wake turbulences of droplets are likely to mix the gas volume, especially if a high disperse volume fraction of droplets is applied to the continuous gas phase.

3.3.3 Influencing the operation conditions

Actively altering the gas residence time within the reactor during operation may be desired for optimizing the conversion. As discussed earlier in this chapter on behalf of several simplified equations and on behalf of experimental investigations within chapter 5 later in this study, the yielded particle diameter is merely a given property, depending on temperature and the velocity in the orifice, the properties of the disperse and continuous phase and further on the orifice diameter. In view thereof, the particle diameter may not simply be adjusted during operation without changing the entire operation condition. This effect however is particularly disadvantageous for methane being dispersed into tin, since in this case, the two-phase flow may not be further influenced from. A known solution is to immerse solid elements into the liquid phase, wherein the rising bubbles are forced to circumvent the obstacles which results in a longer overall distance to be covered, hence an increased residence time.

In the case of tin being dispersed into methane, the gas residence time may be altered entirely independent from two-phase phenomena, simply by altering volumetric flow rate accordingly.

3.3.4 Carbon removal potential

One key advantage of providing a liquid phase to the TDM reaction is having a buoyancy-driven phase separation, driven by accumulating the light solid carbon particles that are formed during the TDM reaction atop of the liquid heavy metal surface. In a subsequent step however, carbon particles or solid carbon agglomerates of any sort need to be removed from the inner reactor volume continuously or intermittently. From

the state of the art, several technologies are known that are sufficient for removing solid particles and/or slag from a liquid metal surface. Due to the novelty of the current process however, no existing knowledge is available on whether carbon removal from a liquid tin surface may be achieved using means that are designed for the use in steelmaking processes. In brief, the following methods are widely accepted in this field of study:

- **Overflow Method** Suppes [48] suggests the immersion or partial immersion of a displacing-body into the liquid, causing the liquid level to rise and allowing the slag to escape by means of an overflow device. Ruff [49] suggests a similar approach; however he includes a scum remover in the shape of a skimmer or scraper or rake which is skimming off the solid elements from the liquid metal surface. The skimming is performed in an extended pool of liquid metal with a constant filling height. By means of Ruff's technology, solids or slag are mechanically forced out of the reactor volume.

- **Rotating Surface-Skimmer Method** A possible method for surface skimming in liquid tanks is the application of rotating skimming blades. The difficulty of such method is manifested in the challenge to skim as little liquid as possible and at the same time to prevent the formation of a packed solid layer underneath the blades. Numerous designs are known, see for example Bourke et al. [50].

- **Tilt-and-Rake Method** Especially in the metallurgical industry, liquid metal tanks are often tilted in order to remove the uppermost layer of the liquid metal including floating solid particles and/or floating slag with or without additional mechanical skimming devices. One example is provided by Abel [51], who suggests tilting the reactor vessel to a degree most suitable for the skimming procedure and to skim

the slurry off the surface into a receptacle by means of a transversally movable arm.

- **Scoop Method** A further possibility of removing slag from large liquid metal baths could be to lift the slag out of the furnace by means of a hollow scoop with an open side, the scoop being pivotally mounted onto the furnace, as suggested by Blank [52].

- **Conveyor-Worm Method** Considering the future application of thermal cracking of methane, it is desired to develop or use a skimming method of low-invasive nature and at the same time a simple, yet effective performance. One possibility would be to apply a stationary conveyor with a horizontally extended axis, as suggested by Klotz [53].

- **Suction Method** An effective method for slag removal is the utilization of a slag cleaner, as suggested by Matsunaga [54], wherein the slag cleaner comprises a suction head that is positioned slightly above the slag surface, floating on the liquid surface. The suction head is connected to a vacuum pump or vacuum source, and slag is drawn through the head and discharged downstream of the suction head [54].

Considering the first option, dispersing methane into liquid tin, in principle all of the above discussed slag removal technologies could serve as a basis for developing a suitable carbon-removal technology, particularly because a bubble column reactor may be treated as a tank, if no gas flow is applied to the bubble column. However, none of the above discussed potential carbon removal technologies are applicable to a spray tower system, due to the extremely dynamic liquid metal surface, particularly in view of the continuously approaching liquid metal droplets.

3.4 Concluding remarks on the chosen reactor concept

Current chapter illustrates the strategy followed in the very beginning of the project. From a vast spectrum of possible liquids needed for phase separation and heating purposes, liquid tin was identified and later discussed in terms of the most helpful reactor integration. Basic calculations using non-dimensional numbers in combination with existing correlations from literature have shown that the dispersion of methane is favored over the dispersion of tin, for several reasons. First, for identical fluid particle diameters, tin droplet velocities are surpassing methane bubble rise velocities by three orders of magnitude. Comparing the obtained volume fraction for both systems based on the fluid properties and the superficial gas velocity, quite similar results have been found. The volume fraction obtained during the dispersion of tin into methane is lower by three orders of magnitude, compared to the dispersion of methane into tin. From a chemical reactor engineering point of view, ideal reactor models show, that TDM reaction yields more products at a given reactor space time if a PFR is chosen compared to a CSTR, which is attributed to less mixing of reactants inside the PFR. In abstract terms, the change of product concentration inside a bubble column resembles the concentration change of a PFR, whereas a spray tower reactor is likely to mix the gas phase utterly. However, the spray tower system was identified to be more flexible in terms of adjusting the desired gas residence time, in order to operate the reactor at a given conversion rate. In a final comparison, the known slag removal technologies have been assessed in terms of their applicability to carbon removal purposes for both reactor options, with the result that said removal means and methods cannot be used within spray tower system. As a conclusion of above stated findings, it was decided to proceed with a bubble column reactor using liquid tin as heat transfer media in the presence of thermal decomposition of methane.

Chapter 4

Applying falsification methods to thermal decomposition of methane

---

► Within the following chapter three basic hypotheses are deducted from a reference study, wherein said three basic hypotheses serve as the starting point for the subsequent experimental investigations.

“The game of science is, in principle, without end. He who decides one day that scientific statements do not call for any further test, and that they can be regarded as finally verified, retires from the game".

- Karl Popper, *“The Logic in Scientific Discovery” (1934)*

In his book “The Logic of Scientific Discovery”, published in 1934 [56], Karl Popper pos-

tulated a revolutionary approach on how scientific knowledge should be acquired. Influenced by the work of Anaximander and, to some extent, by the work of Hume, Popper developed a theory he called “critical rationalism” which is in direct opposition to the formerly predominant empiricism and inductive methodology [57]. His fundamental statement is that any human knowledge including all scientific theories is, in fact, based on a series of observations and assumptions and that it is impossible to receive a final approval of any theory, regardless of how many times it was proven correct. Consequently, he strictly rejects conclusions drawn from observed phenomena as a foundation or justification of knowledge. According to D. T. Early [58], rather, he claims that since a theory can never be confirmed, but it can only be falsified- and as long as a theory withstands falsification attempts and therefore is not replaced by an improved theory, it may be considered valid until it is objected by falsification means. Therefore, according to Popper, any scientific work needs to be evolved around basic negating statements or hypotheses from the very beginning, it needs to be the motivation for all scientific work. To do so, existing theories and all findings need to be tested by their intrinsic negating or non-existence statement “The theories of natural science, and especially what we call natural laws, have the logical form of strictly universal statements; thus, they can be expressed in the form of negations of strictly existential statements or, as we may say, in the form of non-existence statements (or “there-is-not” statements)” [58],[56]. If there is no certain truth however, but only currently un-falsified theories, from a pragmatic point of view, two main questions arise: (1) Which existing theory shall provide the foundation for our actions? And (2) which existing theory shall be preferred for our actions? Popper’s answer to question (1) is, that we may not rely on any theory ever, since a theory can never be proven. His answer to question (2) is that we should favor the best-tested theory among all options, since testing a theory is the only reasonable path to go. As a reminder, the most wide spread acceptance and application of a theory is not

necessarily corresponding to the best-tested theory.

4.1 The methodology of testing a theory

According to Popper, the process of testing a theory always follows the same procedure which he calls the methodology of deductive testing. Starting from a preliminary stated theory, scientific finding or any sort of hypothesis, one must derive several conclusions in a logical and deductive manner which then need to be questioned in terms of derivability, consistency and contradiction among each other. The conclusions themselves are to be postulated as hypotheses, so called basic hypotheses, and will in a final step be tested by empirical experiments. More specifically, Popper defines four checks that shall be applied to basic hypotheses prior to drawing a conclusion from them.

- Are the basic hypotheses logical amongst each other, or are there any contradictions in the context of the superordinate theory?
- Do the basic hypotheses have an empirical-scientific nature, hence is it possible to conduct empirical experiments which allow a statement of its validity?
- Are the basic hypotheses suitable for providing a scientific progress, in case they stand the test?
- The last check is the examination of the tests by empirical experiments itself.

The entire procedure strictly avoids the utilization of inductive means, but is in strict agreement with the inference rule modus tollens. At no point, a conclusion is applied, withdrawn from the validity of a singular hypothesis, to the validity of the superordinate

theory. Even if all defined hypotheses were found to stand the tests they had been exposed to, it will not be concluded that the theory itself is valid. The here drafted procedure of testing a theory is embedded within the proposed infinite, evolutionary progress of scientific knowledge, which Popper expresses by the following equation.

$$\mathrm{P}_1 \rightarrow \mathrm{BH}_1 \rightarrow \mathrm{PE}_1 \rightarrow \mathrm{P}_2 \tag{4.1}$$

According to equation 4.1, starting from a problem P_1 that can be expressed as a theory, an assumption or a hypothesis, basic hypotheses BH_1 are being deducted according to the above stated rules in order to perform a problem elimination PE_1, which then either leads to a new problem P_2, or it leads to an increased fitness of P_1. The equation expresses the underlying concept postulated in the opening quote of this chapter by Karl Popper.

4.2 Defining the abstract hypothetical theory for thermal decomposition of methane

Applying the methodology of testing a theory to a scientific problem, it seems reasonable to define hypotheses based on existing results that are new and somewhat beyond the expected results or at least pointing into a new direction, mainly for two reasons. First, if the surprising or unusual hypothesis withstands the testing phase, it gains more credibility, hence provides further ground for even more exceptional hypotheses. Second, if the testing phase results in a falsification, this result leads to the withdrawal of the formerly surprising hypotheses. However, due to the iterative process of falsification, knowledge may be gained later from the modified hypothesis that is replacing its predecessor by

providing ground for a repeated, adapted testing phase. Divisive statements therefore are important for the progress of scientific work.

In the case of thermal decomposition of methane in the presence of liquid metal and particularly liquid tin, we have the opportunity to derive several hypotheses from a series of experiments that was conducted by Serban et al. [5] in the year of 2003, providing a wide range of methane conversion results measured in various experimental setups and operation conditions. Moreover, in this specific application, the work of Serban et al. [5] represents the benchmark experiments. In fact, the work of Serban et al. [5] is the only available study providing experimental data for thermal decomposition of methane in the presence of liquid tin. As shown in the end of this chapter, the hypotheses are in parts derived directly from Serban's conclusions and in parts derived from own interpretations of Serban's experimental results. However, due to the limited availability of detailed information regarding the experiments such as dimensions, temperature distribution in solids and operation pressures, no complete assessments about Serban's work can be obtained. The herewithin provided criticism of Serban therefore is to a considerable amount based on own interpretations. It is likely that additional information regarding said experiments would lead to different hypotheses.

4.3 Brief introduction into the work of Serban et al.

Thermal decomposition of methane in contact with liquid metal was subject of very few studies during the recent years which were all conceptual studies without documented results, see for example the work of Steinberg et al. [73]. Therefore, current study mainly focuses on this work and the corresponding experimental results presented by Serban.

Within said publication, Serban described a wide range of different experiments for the purpose of investigating the conversion of a gas mixture which was composed of 95% methane and 5% ethane[1]. In all cases, Serban utilized a 350 mm long and 12 mm in diameter stainless steel cup reactor for the methane decomposition experiments. Natural gas was fed to the reactor using a vertical feed pipe, mounted to the reactor top, and guided the feed gas along the concentrically attached feed tube to the reactor bottom, wherein the feed tube comprised either an open hole or a porous cylindrical sparger on the lower end of the feed tube, see also fig 4.1.

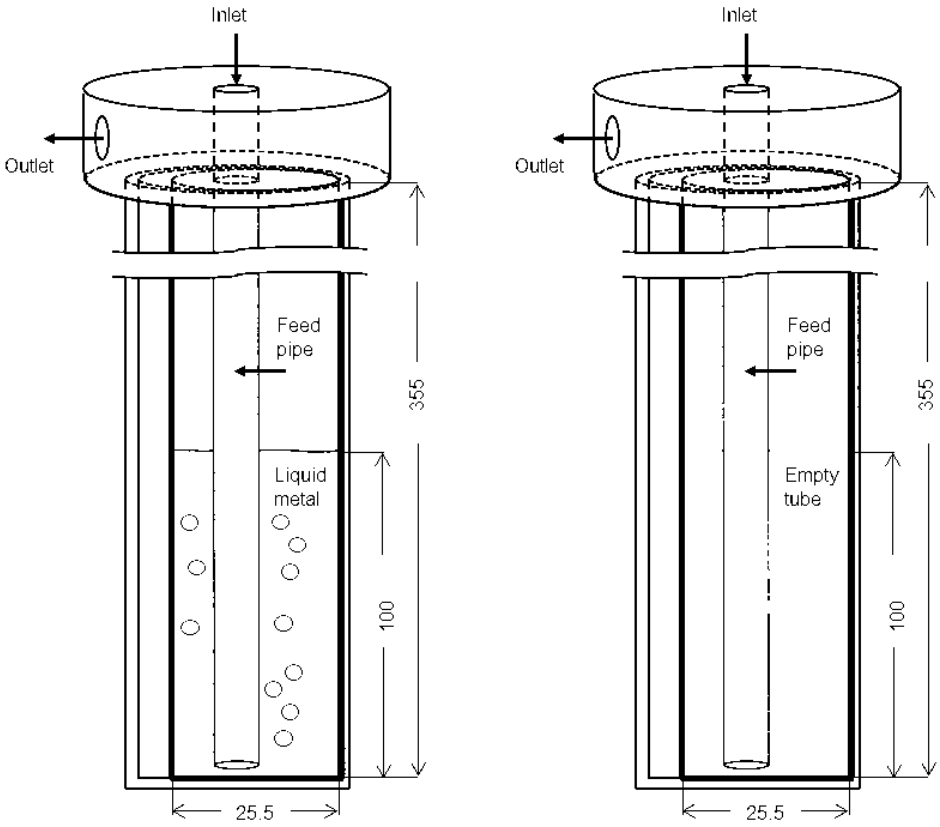

Figure 4.1: Schematic illustration and dimensions of Serban's reactor presented in $[\mathrm{mm}]$-units. The shown figure is based on an illustration taken from Serban et al. [5]

[1]Methane (99.995% research grade) or commercial grade natural gas (95% methane and 5% ethane) was used for the experiments

4.4 Defining the problem and basic hypotheses

Within the publication [5] filed in the year 2003, Serban presents several experimentally gained results in the context of thermal decomposition of natural gas. Among all of Serban's findings, the most striking aspect in terms of methane conversion in liquid tin is depicted in fig. 4.2. Here, methane conversion results are shown for several gas flow rates and a liquid tin temperature of 750 °C. In a first reactor configuration, the tube reactor was filled to about one third with liquid tin and was operated at two different gas flow rates, namely 15 ml/min and 25 ml/min, see squares connected by a solid line. In a second reactor configuration, the tube reactor was empty and operated at three different flow rates, namely 8 ml/min, 15 ml/min and 25 ml/min, see squares connected by a dashed line. According to fig. 4.2, the measured methane conversion

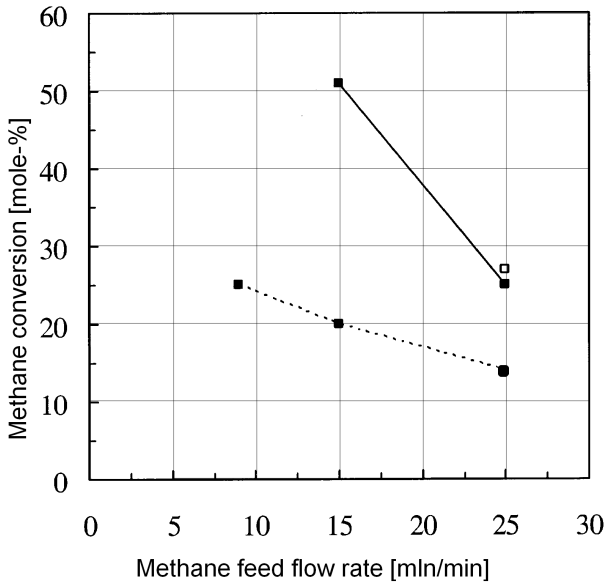

Figure 4.2: Methane conversions in natural gas pyrolysis over 4-in. molten Sn (solid line) or blank runs (dashed line) bubbled through a 0.5 μm (■) Mott sparger at 750°C. Symbol (□) indicates repeated experiments [5].

was always higher for runs with liquid tin compared to runs with an empty tube reactor, so-called "blank runs". Assuming that the reaction thermodynamics of thermal decom-

position of methane is depending on i) the reaction temperature, ii) the gas residence time and further assuming that iii) the entire reactor is isothermally operating time- and location-wise, the above stated findings are striking. Since the presence of liquid metal reduces the volume that is available for the feed gas inside of the reactor by about one third, the total residence time must be reduced by one third as well, assuming very low residence times of the gas bubbles inside the liquid tin. Consequently, the conversion rate should be lowered by about one third as well. However, Serban's findings do not agree thereto. Contrarily, the conversion rate is substantially increased for runs with a reduced total gas residence time in the presence of tin. For a more detailed analysis of the experiments of Serban, see also chapter 9. Based on the assumptions i) - iii), the only explanation of achieving such over-compensation is that liquid tin has a substantial catalytic impact on the thermal decomposition reaction of natural gas, particularly methane. As a conclusion, the starting problem P_1 according to Popper is in the present case defined as:

Problem (P_1) *At an operation temperature of about 750 $^\circ$C, liquid tin has a catalytic impact on the decomposition of natural gas, particularly methane, if the latter is dispersed into the liquid in a bubble column-like reactor setup.*

In the following, it is primarily desired to postulate and answer several basic hypotheses that are deducted from analyzing the reference-study. Finding these answers however shall not be achieved on behalf of repeated identical experiments, but by conducting own experiments, comprising a basis which still allows an evaluation of the key questions, yet in an advanced context. In detail, the subsequently conducted experiments have been utilized in a reactor of much larger dimensions and different design features. Therefore, two-phase and heat-transfer phenomena may vary to a certain degree. However, on behalf of three basic hypotheses, the problem P_1 will be tested. In view of the above,

and as a general observation, if liquid tin catalytically supports the TDM reaction, said effect is valid for all reactor geometries and further is this effect most likely increasing with increased temperature. The above stated hypothesis shall be tested on behalf of experiments that allow a comparison of methane conversion in the presence of liquid tin and without the presence of liquid tin.

Basic Hypothesis 1 ($\mathrm{BH}_{1,1}$): *At 750 °C and at similar gas residence times compared to Serban et al., runs with liquid metal yield a higher conversion rate compared to runs without liquid metal.*

Focusing on another aspect of fig. 4.2, the rather trivial effect of longer residence time leading to higher conversion rates shall be comparatively interrelated with the observations provided by Serban. This may solely be identified by an analysis of the above envisaged comparative experiments.

Basic Hypothesis 2 ($\mathrm{BH}_{1,2}$): *At an operation temperature of 750 °C, runs without tin show an increase in methane decomposition for longer gas residence times, yet with a slower slope compared to runs with liquid tin.*

Furthermore, referring to a further aspect fig. 4.2, the increase of conversion for lowered flow rates needs to be addressed. At the above stated limitations, liquid tin is hypothesized to be catalytic and the reaction is hypothesized to proceed predominantly in the liquid phase. Such increase of conversion as a function of the flow rate may only be achieved, if the bubble residence time is increased substantially for smaller flow rates, or if the specific surface area of the gas within the liquid is substantially increased. The latter is particularly important for a catalytically active liquid, since gas would be catalyzed on the surface of the liquid. Smaller bubble sizes further correlate with an increased specific surface area.

Basic Hypothesis 3 ($\mathrm{BH}_{1,3}$): *Bubble size and bubble rise velocities of gas injected into liquid tin using a porous sparger are significantly flow rate dependent.*

4.5 Further implementation of falsification means into current thesis

Previously, the core problem has been defined which represents the key question on whether the utilization of liquid tin to the process of thermal decomposition of methane might be particularly advantageous compared to existing technologies. The herewithin discussed hypotheses however do not aim to entirely answer the question on whether tin should be utilized in general, especially due to the proven advantages that were discussed in previous chapters, such as the improved heat transfer, and in particular the phase separation for processing intrinsically formed solid carbon.

The objective of subsequent chapters therefore is to explain, conduct and evaluate a series of experiments which aim for testing the previously defined basic hypotheses. At a given point of the chapter, a reference to current chapter is made. However, for the sake of clarity, a final discussion of the outcome of the current thesis is provided in a final chapter 10.

In the subsequent chapters, thermo-chemical models will be presented, which have been developed to suitably support the conducted experiments on behalf of several kinetic parameters taken from literature. For comparative purposes, said models have further been applied to the reactor of Serban.

Chapter 5

Bubble size, velocity and frequency measurement in liquid tin

---

► Current chapter covers a series of experiments conducted for the purpose of investigating bubble characteristics of gas bubbles injected in liquid tin. Furthermore, the experimental setup and in particular the custom-made sensors will be presented.

The following chapter aims to test the third basic hypothesis which was introduced in the previous chapter. Said basic hypothesis was developed in the context of the work conducted by Serban et al. [5] and was defined in the previous chapter according to:

Basic Hypothesis 3 ($\mathrm{BH}_{1,3}$): *Bubble size and bubble rise velocities of gas injected into liquid tin using a porous sparger are significantly flow rate dependent.*

Since the bubble properties are crucial to all future experiments both in terms of selecting the right design of the reactor and also in terms of understanding the reactor

behavior, this third basic hypothesis shall be tested first.

Investigating the bubble properties was conducted before and independent from the methane decomposition experiments which will be covered in the subsequent chapter. Therefore, and for the purpose of a simplified readability, this chapter aims to include all relevant information that are required for understanding the herewithin covered experiments.

5.1 Introduction in bubble measurements in liquid metal

Bubble measurements in liquid metals have been subject of research and industrial-scale efforts mostly in the context of material-refining processes agitated by gas injection, for example submerged oxygen injection in the steel making process [55]. In the context of those efforts, technologies for measuring bubbles in liquid metal have been developed. Said technologies can be divided into invasive and non-invasive techniques. Non-invasive techniques such as radioscopic methods and flow tomography have the advantage of inducing no or little impact on the measured flow pattern. The drawback of mentioned non-invasive measurement technologies is the complexity and cost intensity of high energy applications which are needed to transmit waves or radiation through the highly dense media. Common invasive techniques are needle probes of various shape and Ultrasonic Doppler Velocimetry (UDV) methods. UDV sometimes is regarded as non-invasive method; it is however required to inflict the ultrasonic wave to the flow region by a continuous acoustic path which is usually established by submerging the transducer directly into the liquid. For high temperature applications, the

transducer is extended using a wave guide, guiding the acoustic waves from the transducer into the liquid and back. Invasive methods have the disadvantage of a) influencing the flow pattern by the flow resistance induced by the probe itself and b) being exposed to high temperatures along with the possibility of chemical attack. In the case of UDV technologies, a further obstacle is to provide a properly wetted interface between liquid and the wave propagating surface of the sensor. Present study investigated UDV measurement technologies first. Due to tin-corrosion inflicted damages to the UDV wave guide, it was then decided to investigate the bubble characteristics in liquid tin by means of needle probes only. The following sections aim to provide gained insights in handling the needle probe sensors and to discuss the results.

5.2 Survey on studies focusing on bubble measurements in liquid metal

Two-phase flows in liquid metal have been subject to a series of investigations throughout the last decades, with first investigations starting in the mid 70's. The vast majority of available studies conducted are in the context of refining processes such as the deoxidation of copper, degassing of aluminum and decarburization of stainless steels. In the early years of this technology, either sound-based measurements of so-called electroresistivity probes have been utilized for measuring both single bubbles and bubble swarms in liquid metal. Pioneer work in the field of measuring two-phase phenomena in liquid metals by means of electroresistivity probes was achieved by Sano and Mori in the late 70's and early 80's [59]. In their study, the behavior of bubble swarms in mercury has been investigated in terms of the axial and radial gas hold-up distribution. On behalf

of a single-needle probe, the bubble frequency was detected at different locations of the reactor. About a decade later, Iguchi et al. [60][61][62] again utilized electroresistivity probes, or needle probes. In his work, he focused on both understanding the bubble sizes of large single bubbles in liquid metal at ambient temperatures using Wood's metal and later also on measuring bubble sizes and bubble velocities in a molten iron bath at 1600 °C. The latter work also includes the technical features of the custom-made needle probes that have been submerged into the molten iron, serving as the basis for the development of the needle probes used in this thesis. In the year 2004, Saito et al. [63, 64] also applied needle probes to measure the shape transitions of nitrogen gas bubbles that were injected into a lead-bismuth volume in combination with neutron radiography visualization means.

Unfortunately, physical properties of the aforementioned alloys differ from those of tin to a great extent, whereas studies considering gas-liquid applications utilizing liquid tin are very rare. The work of Andreini [65] provides the most useful insight, since it is the only available study for bubble measurements in liquid tin. Andreini [65] measured the bubble rise velocity of single bubbles in liquid tin at a temperature of 262 °C by means of detecting the noise that was generated by the successively rising bubbles during the departure of a submerged nozzle and during the splash formed when the bubble reached the liquid tin surface. Andreini [65] further considered the bubble volume V_{B} by correlating the applied volumetric flow at standard conditions $\dot{V}_{\mathrm{STP}}$ with the detected bubble detachment frequency f:

$$V_{\mathrm{B}} = \frac{\dot{V}_{\mathrm{STP}}}{f} \tag{5.1}$$

wherein the bubble diameter d_{B} may be retrieved from the bubble volume V_{B}, assuming

a spherical shaped bubble. During the experiments, the flow rate and also the orifice diameter d_{O}, corresponding to the submerged orifice had been varied. Andreini states that the findings observed in liquid tin for the explained series of experiments could be described with the non-dimensional function

$$\left(\frac{d_{\mathrm{B}}}{d_{\mathrm{O}}}\right)_{\mathrm{Sn}} = Fr_{\mathrm{O}}^{0.227} We_{\mathrm{O}}^{-0.112} \tag{5.2}$$

on behalf of the orifice Fr_{O} and orifice We_{O}- numbers. Based on the calculated bubble diameter d_{B}, the bubble rise velocity v_{B} further yielded in the equation:

$$v_{\mathrm{B}} = 29.69\, d_{\mathrm{B}}^{0.316} \tag{5.3}$$

which provides a useful basis for the comparison of own experimental findings with those of Andreini. The measurements of Andreini are represented in fig. 5.1, showing some of his findings: the frequency of bubble formation increased with the orifice Reynolds number (and hence the gas flow rate) up to some limiting value after which the frequency remained relatively constant [65]. Said observation is further depicted in the left plot of fig. 5.1. Moreover, Andreini finds that below a critical frequency $f_{\mathrm{B,\,crit}}$, the bubble volume is not much affected by the frequency, especially for small orifices. Rather, it appears as if the increase in flow rate causes an increase in bubble frequency at a more or less constant bubble volume. However, beyond the critical frequency, the observed phenomena are not applicable. Here, for an increase in flow rate, a constant frequency yet with a continuously increasing bubble volume were reported, see also right image of fig. 5.1. Andreini [65] explains the aforementioned observations by the assumption that for low frequency regimes, surface tension dominates the bubble formation pro-

cess, whereas for high frequency regimes the momentum of the incoming gas has the predominant impact on the bubble formation process.

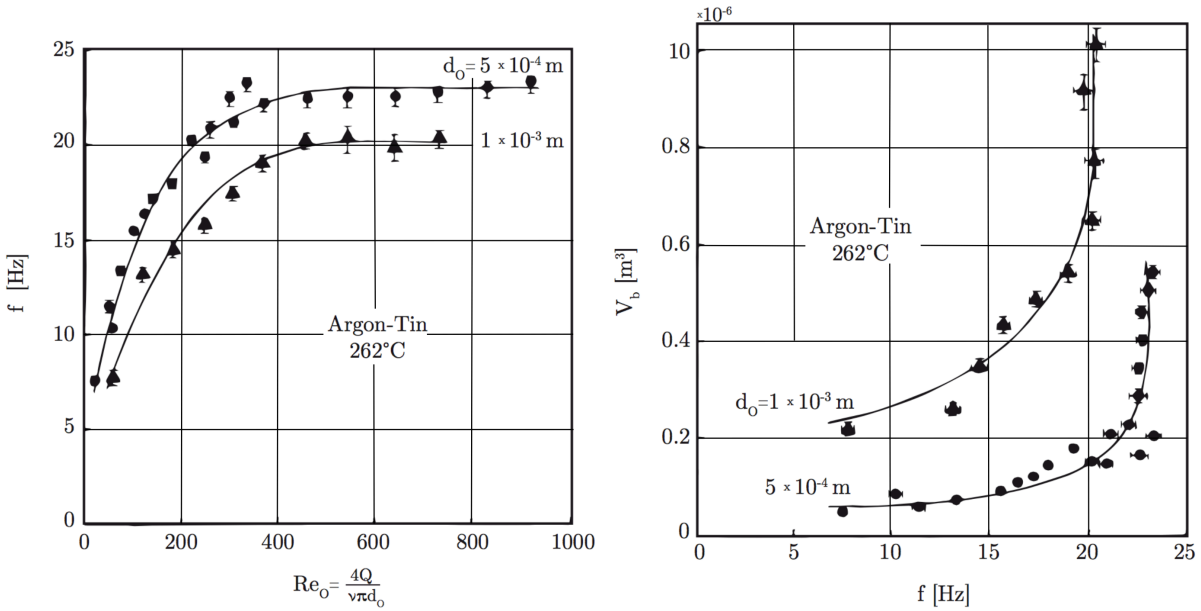

Figure 5.1: Experimental results obtained for single Ar-bubbles rising in liquid tin at 262 °C. Left: dependency of the bubble frequency f on the orifice Reynolds number Re_{O}; right: dependency of the bubble volume V_{B} on the bubble frequency f [65, 66]

5.3 Needle probes for bubble measurements in liquid metal

5.3.1 Explanation of the concept

In general, for the determination of the properties of liquid and multi-phase mixtures, for example of the gas bubble properties, the measurement of the electrical conductivity is widely used. To do so, electrodes are submerged in the medium or the mixture to be measured and integrated in an electric circuit to measure the conductivity by means of

direct or alternating voltage.

For the measurement of gas bubbles in liquid tin however, no ready-to-use probes were identified on the market. Therefore, a custom-made needle probe was developed, which will be explained in the following. According to fig. 5.2, the base component of the custom-made needle probe sensor 1 is provided by a thermocouple, namely a type-K thermocouple with an outer conductive shell 2 and an inner insulation material 3 for an electric resistivity of about 10 $\mathrm{M}\Omega$. Inside the insulation material 3, two separate wires 4a and 4b are guided. According to the setup of the type-K thermocouple, wires 4a and 4b are composed of slightly different alloy compositions; 94.5%Ni+5.5%Al-alloy and 90.5%Ni+9.5%Cr-alloy. However, this difference in alloy composition is of no relevance for current application as a needle probe. In order to obtain sufficient needle probes for the envisaged measurement in turbulent gas flow in the liquid metal, two stainless steel needles 5a and 5b where welded onto the wires 4a and 4b, wherein needle 5a surpasses the length of needle 5b by 5 mm. Subsequently, the welding spots were filled with insulating ceramic glue. When a bubble approaches the needle, it must cause a complete temporary insulation of the probe, in order to trigger a change in voltage. Therefore, the needles 5a and 5b as well as the front face of the needle probes were insulated by means of an insulation coating 6, with the exception of a conductive tip 7a and 7b on each of the needles 5a and 5b. On the back end of the needle probe, the wires 4a and 4b were connected to a two-pin plug 8 for a convenient integration into the electric circuit.

Fig. 5.3 provides a scaled view of a needle probe according to the embodiment of fig. 5.2. The total length of the needle 5a is 24.8 mm, wherein the conductive tip protrudes to about 2 mm from the insulation cladding 6. The core diameter of the conductive tip is 0.2 mm; the overall diameter of the protruding needle is 0.6 mm. The second nee-

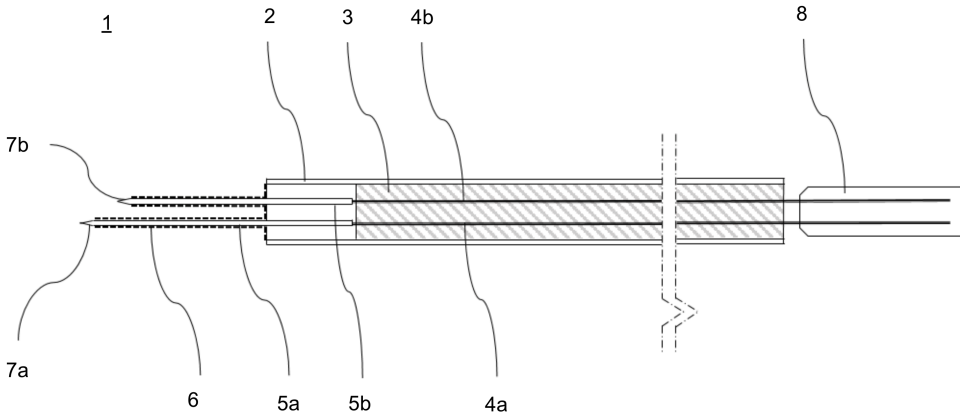

Figure 5.2: Simplified schematic illustration of a custom-made needle probe sensor 1 according to the embodiment of the sensor used for the measurements of the bubble rise velocity, bubble diameter and bubble frequency

dle 5b is of identical design, yet with an offset of 2 mm in the direction of the sensor axis. Furthermore the distance of the two parallel needles 5a and 5b is 2 mm. The sensor core is composed of an 800 mm long and 4 mm in diameter tube, originating from a type-K thermocouple as described above.

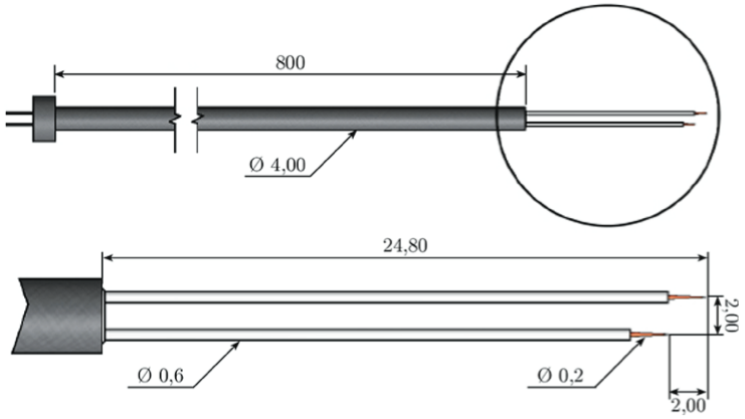

Figure 5.3: Illustration of the dimensions of the used needle probe sensor according the embodiment of the above presented sensor.

The integration of the above explained needle probe sensor into the liquid metal bubble column reactor is depicted in fig. 5.4. Here, a 316 SS stainless steel tube reactor is

shown comprising a porous steel disc on its bottom, the porous steel disc[1] - also referred to as Sparger - comprises a connector to the gas supply feed. The tube reactor has a total length of 550 mm, an inner diameter of 35.9 mm and is filled to a height of 300 mm with liquid tin[2]. As shown in 5.4, the needle probe sensor is adjustable inserted from the open top of the reactor tube and is partly submerged into the liquid metal.

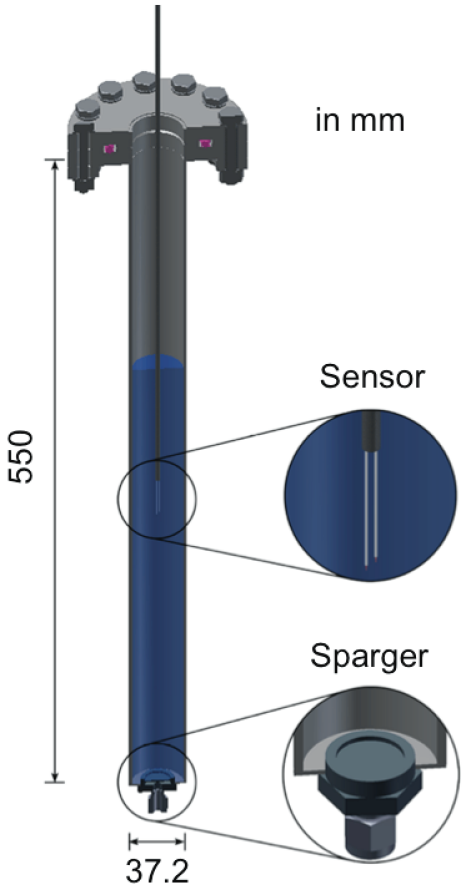

Figure 5.4: Cross-sectional view of the reactor used for bubble measurement with attached needle sensor

[1]The 316SS stainless steel porous sparger comprises a porous diameter of 19 mm and an average pore size of 50 μm

[2]The liquid tin filling height refers to a theoretical height of liquid tin at a temperature of 300 °C and without the presence of bubbles inside the liquid containment.

5.3.2 Experiments in liquid tin using the needle probe sensor

In the following section, an overview of the conducted experiments for measuring the bubble rise velocities in liquid tin will be presented. The majority of this content was obtained by the master's thesis of Sebastian Herbst [66] which was embedded in context of current study and also within an own publication together with fellow colleagues from the KIT [67]. Therefore, the experiments will only briefly be discussed; for a more detailed discussion such as measurement routines and data processing, please refer to mentioned publications.

The integration of the needle probe sensor is explained on behalf of fig. 5.5. Being submerged in the fluid inside of the reactor containment, each needle probe of the needle probe sensor 1 is integrated in a separate electric circuit with an inner electric resistance R_i. The electric circuits further comprise a common DC voltage source[3] and a common electric connection to the liquid. Depending on the applied voltage in the source and on the inner resistance of the circuit, a current is established. According to 5.5, the change in current was measured by integrating an additional resistance into the circuit which allowed to detect the change in voltage, for which a LabView- routine was built and applied, see also [66] for further information.

Parameter	Value	Unit
Sampling rate	5	kHz
Supplied voltage	3.6	V (DC)

Table 5.1: Electric parameters used for the experiments, namely the sampling rate, resolution and the supplied voltage

According to [66], the electric circuitry was designed in the form of two parallel circuits, see also fig. 5.5

[3] A National Instruments USB-6008 was used as DC voltage source and analogue digital converter

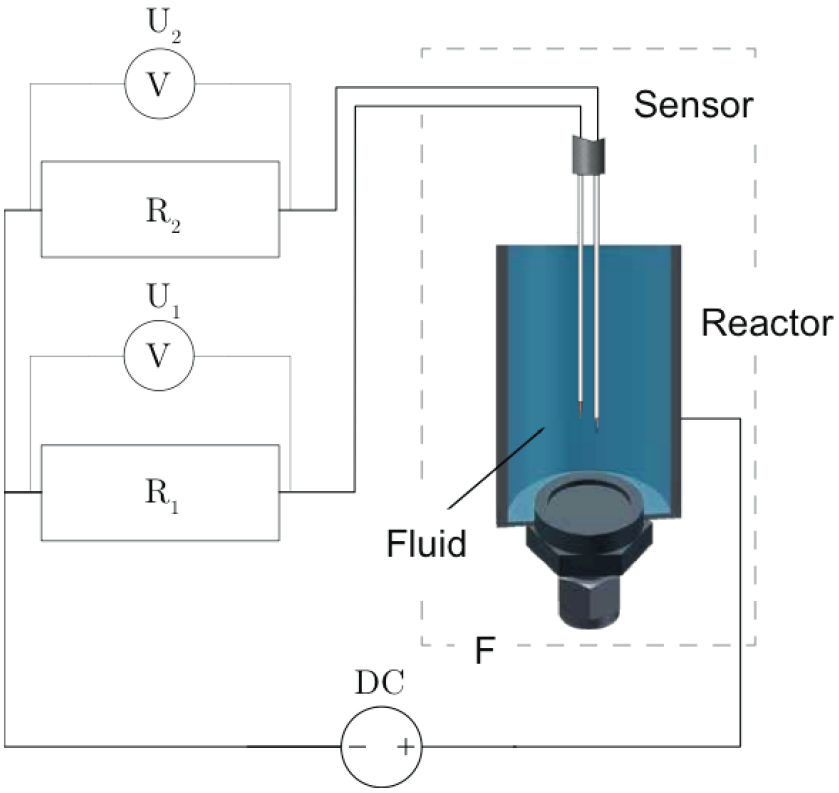

Figure 5.5: Illustration of the electric circuits used in the experimental setup

Therefore, the measured voltages U_1 and U_2 can be expressed as

$$U_1 = U_2 = U\frac{R_{\mathrm{DAQ}}}{R_{\mathrm{total}}} = U\frac{R_{\mathrm{DAQ}}}{R_{\mathrm{DAQ}} + R_{\mathrm{S}}} \tag{5.4}$$

where R_{S} represents the overall resistance of the sensor unit including the liquid metal and the reactor bulk. The total resistance of the DAQ R_{DAQ} is defined as

$$R_{\mathrm{DAQ}} = \frac{R_1 R_2}{R_1 + R_2}\,, \tag{5.5}$$

allowing a representation of the voltage to be measured according to:

$$U_i = U \left(1 - \frac{1}{1 + \frac{R_i}{R_{S_i}}} \right) . \tag{5.6}$$

On behalf of equation 5.6, it is shown that if the resistance R_{S_1} is increased, for example due to an attached bubble, the voltage decreases.
According to the above provided description, in an ideal scenario, the measuring method is characterized in the following steps, wherein a bubble

1. approaches the lower needle such that it is pierced by needle;
2. the bubble then rises further such that the conductive tip of needle is fully insulated, thus causing voltage U_1 to drop;
3. is then pierced by the second needle, comprising a vertical offset of 2 mm towards needle in an upward direction;
4. subsequently also fully insulates the conductive tip of needle, thus causing voltage U_2 to drop;
5. then disengages first from the lower conductive needle tip, causing voltage U_1 to recover, and then from the upper conductive needle tip, causing voltage U_2 to recover to its initial voltage levels.

5.4 Data processing

In the following, the lower needle is referred to as needle ”A”, whereas the upper needle is referred to as needle ”B”, according to the embodiment of fig. 5.2. As discussed above, the binary sensor differentiates between the voltage levels U_{LM} and U_{Gas}, referring to

liquid metal or gas as the medium surrounding the conductive tip. For each needle, the event of insulation that is established when a bubble encloses the needle tin has the time-span Δt_i. It is started at the starting incident which is referred to by the index 1 and ended at the ending incident which is referred to by the index 2. Fig. 5.6 exemplary illustrates how a bubble might approach the two needles. Ideally, both needles should pierce the bubble along the center of the bubble which is however never the case due to the lateral offset of the two needles to each other.

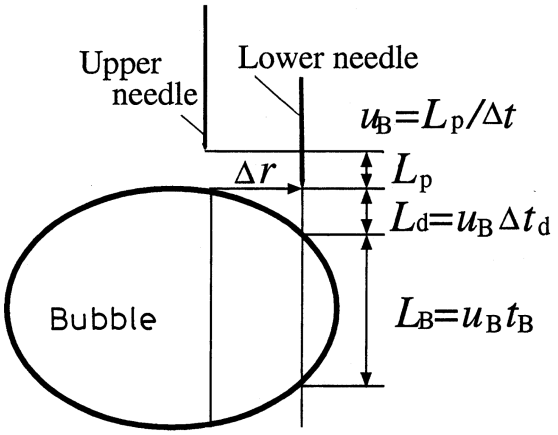

Figure 5.6: Illustration of a bubble approaching the two-needle probe sensor [61]

In an ideal case, a bubble approaches the sensor with a vertical flow direction in the centerline of the sensor rod, comprising a bubble diameter of $d_\mathrm{B} \gg 2\,mm$. On its upwardly directed movement, the bubble is pierced according to the previously explained measuring method, triggering the signals t_{A_1} and t_{B_1}. Accordingly, the ending signals t_{A_2} and t_{B_2} are triggered in the same way. By means of the time-span in between the signals t_{A_1} and t_{B_1} and the vertical offset L_p, the velocity v_B of the bubble front can be calculated as follows.

$$v_\mathrm{B} = \frac{L_\mathrm{p}}{\Delta t} \tag{5.7}$$

The actual measured length of the pierced bubble section is defined as the chord length $L_{\mathrm{A,B}}$, which is measured at the corresponding sensor tip. The chord lengths may further be expressed using the bubble rise velocity v_{B} in combination with the time-span Δt for each sensor tip [66].

$$L_{\mathrm{A}} = v_{\mathrm{B}} \cdot \Delta t_{\mathrm{L,A}} \text{ and } L_{\mathrm{B}} = v_{\mathrm{B}} \cdot \Delta t_{\mathrm{L},B} \tag{5.8}$$

whereas Δt_{L} is defined as

$$\Delta t_{\mathrm{L},A} = t_{A_2} - t_{A_1} \text{ and } \Delta t_{\mathrm{L},B} = t_{B_2} - t_{B_1} \tag{5.9}$$

Above stated signal analysis clearly shows the application limits of explained needle probes. Considering the chaotic bubbly flow in the observed volume, many different scenarios of bubble approaches are likely. In most cases, only one of both needles provided signals without the corresponding counterpart, indicating that the velocity vector of the approaching bubble has either an angular or horizontal offset to the centerline of the sensor rod. For the purpose of filtering noise created by bubble fragments from useful bubble measurements, several filter rules have been stated, see Herbst et al. [66] for further details. As mentioned earlier, for each experimental run to be measured, only a fraction of the acquired signals were actually considered and applied for measuring the bubble rise velocity and the bubble chord lengths. In order to obtain a sufficient amount of bubble signals, each flow-rate condition to be measured was maintained for time spans ranging from 5 min up to 30 min. The signal output of a bubble measurement according to above described method is provided in an exemplary illustration 5.7 of the measurement of several bubbles approaching and disengaging from a two-tip

needle probe sensor. The upper half of the illustration represents raw signals, as they were acquired from the measurement installation. Here, the blue line represents the lower needle and the red line represents the upper needle. For processing purposes, the signals were normalized, as shown in the lower half of the illustration. This figure again shows that only in some cases where a needle probe triggered a signal, the other needle probe also triggered a useful signal as well.

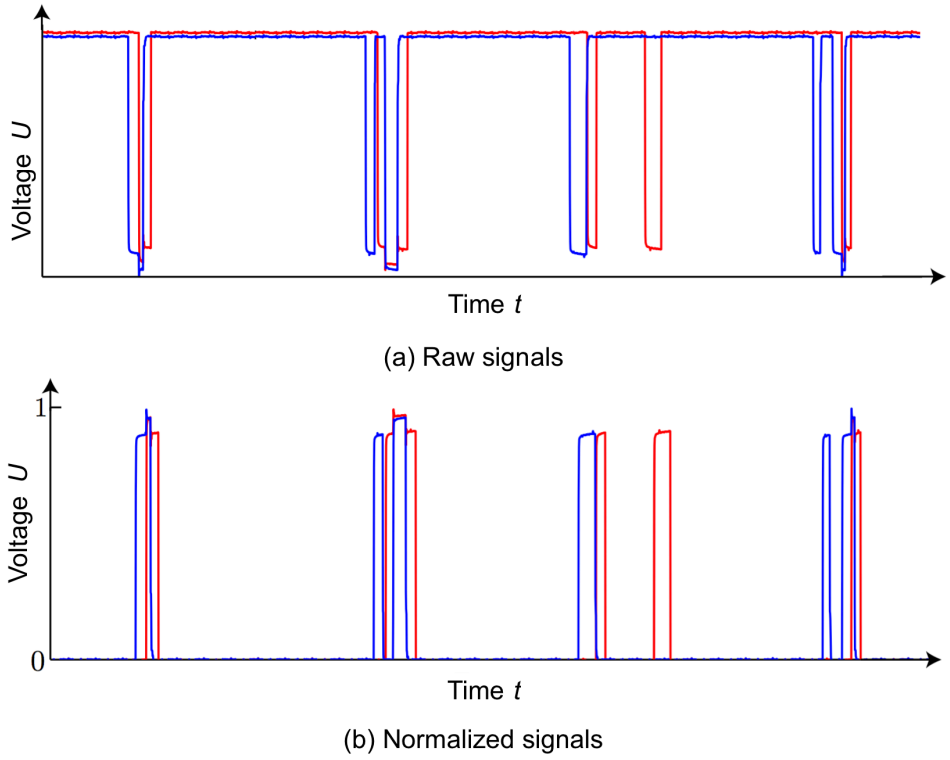

Figure 5.7: Exemplary illustration of signals produced during bubble measurements using a two-tip needle probe sensor

5.5 Discussion of the experimental results

Needle probe sensors according to the above explained embodiment have been applied to liquid Sn at 300 °C, in order to measure the bubble rise velocity as well as the bubble

chord length of bubbles formed inside of a reactor according to reactor presented in fig. 5.4. Argon gas was injected and dispersed at the bottom of the reactor at volumetric flows in the range of 5 mln/min to 200 mln/min, referring to nominal conditions. This range of flow rate was identified to represent the most likely range of flow rate for the later TDM experiments. It was identified by water mock-up experiments using quartz glass reactors to allow both an extremely low flow rate at 5 mln/min with only one string of single bubbles detaching from a porous quartz disc and also a very churn and vibrant flow at 200 mln/min. Furthermore, said range also covered the feed flow ranges used within the vast majority of known TDM studies of other research projects. The operation temperature was limited to 300 °C, because the conductive tips of the needle probe sensor were rapidly corroded by the surrounding liquid tin already at this temperature, let alone higher temperatures. Moreover, due to thermal and vibration loads on the needle probe sensor, the insulation of the needles quickly malfunctioned and caused a short-circuit, thus causing a malfunction of the needle sensor.

Bubble rise velocities were obtained from the signals of the sensor tips and based on the above stated equations. For a variation of flow rates in the range of 10 mln/min to 200 mln/min, a slight increase in bubble rise velocities was observed in the range of 16 cm/s up to 24 cm/s, yet with an inconsistent growth rate among lower flow rates. Fig. 5.8 provides both the mean bubble rise velocity (right axis, black circles) and the bubble frequency (left axis, black diamond) as a function of the applied nominal feed flow rate.

With respect to the findings of Andreini et al. [65], it shall be mentioned that current experiments applied a porous metal sparger instead of a single-hole orifice which was used by Andreini. However, during the execution of the experiment, a repetitively occurring bubble break-up was observed at the sparger, rather than a continuous bubbly flow. Reasons for such bubble behavior might be a lack of wetting at the metal surface

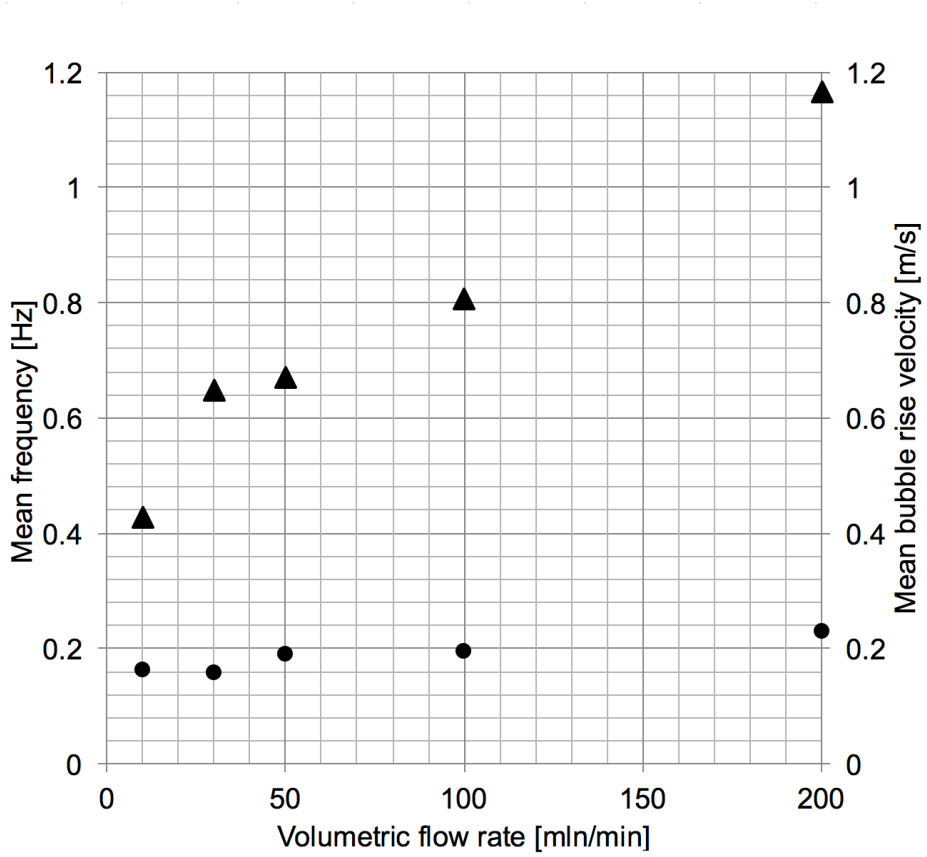

Figure 5.8: Overview of the experimental results. Obtained bubble frequencies (▲) and mean bubble rise velocities (●) are shown for various flow rates of Ar

that was in contact with liquid metal, due to an oxide-layer on the top surface of the porous sparger. Therefore, the observed bubble regime was even closer to the one observed by Andreini et al. Furthermore, as will be shown in chapter 6, the later conversion experiments also used a single hole orifice, due to other reasons which are explained there. It is a fortunate incidence that the behavior exhibited by the sparger seams to result in similar bubble release characteristics as single hole orifices in the observed reactor configuration.

Fig. 5.9 illustrates a comparison of experimentally obtained (●) own results and results obtained from applying Andreini's correlations to the corresponding experimental conditions. It is shown that measured bubble rise velocities and also bubble diameters tend

to be slower and smaller in experiments, compared to the results gained from the correlation. Considering the invasive needle probe sensors, it is likely that the sensor itself causes the bubbles to locally slow down and also it is likely that the measured chord length is smaller than the actual chord length, due to bubble deformation during the piercing by the needle. The depicted function represents the results of equation 5.3 for the given operation conditions. However, the comparison of fig. 5.9 shows that the obtained experimental results in fact follow the same trend and are in the same order of magnitude as the predicted results, making use of the correlation provided by Andreini.

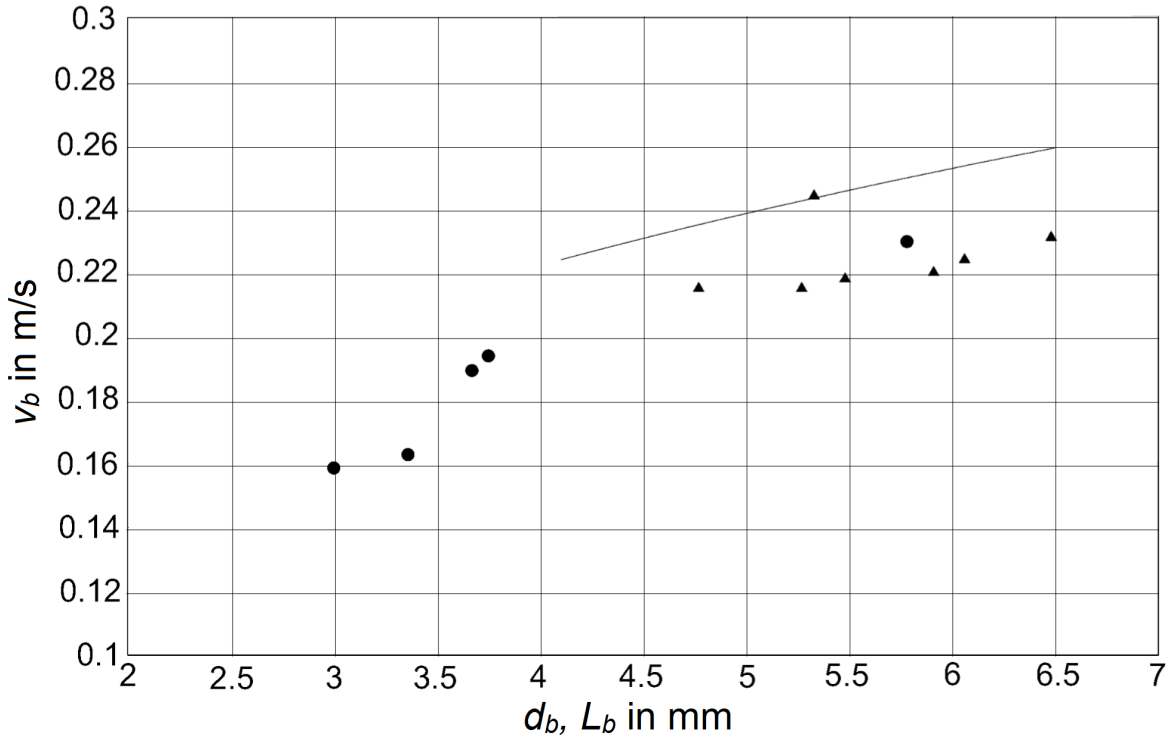

Figure 5.9: Comparison of own experiments in tin at 262 °C (▲) and 300 °C (●) with theoretical results based on the correlation provided by Andreini et al. [65], which is represented by the solid line.

The bubble regime may further be estimated on behalf of a graphical correlation provided by Clift et al. [68] on the basis of the dimensionless Reynolds number Re, Eötvos number Eo and the Morton number Mo. For given properties of the liquid and gaseous

phase, it is possible to predict the bubble shape qualitatively. The before-mentioned numbers are defined as

$$Re = \frac{\rho_{\mathrm{L}} \cdot v_{\mathrm{L}} \cdot d_{\mathrm{B}}}{\eta_{\mathrm{L}}} \tag{5.10}$$

$$Eo = \frac{\Delta\rho \cdot g \cdot d_{\mathrm{B}}^2}{\sigma_{\mathrm{L}}} \tag{5.11}$$

$$Mo = \frac{g \cdot d_{\mathrm{B}}^2 \cdot \Delta\rho}{\rho_{\mathrm{L}}^2 \cdot \sigma_{\mathrm{L}}^3} \tag{5.12}$$

Fig. 5.10 depicts an excerpt of the Clift-Diagram, representing the parameters for the gas bubbles in tin at 300 °C, based on the previously shown experimental results. It is shown that the observed results are beyond the existing range of parameters, considered by Clift et al. which is mainly a consequence of the high density and the high surface tension of liquid tin. It is further indicated that based on this diagram, the bubbles should be of a wobbly, ellipsoidal shape rather than of a spherical shape. The circles refer to the measured values of the herewithin conducted experiments. It was found that higher applied flow rates lead to more wobbly-shaped bubbles.

5.6 Summary and concluding remarks

With reference to fig. 5.8, the following conclusions may be drawn. Average Ar-gas bubble rise velocities of Ar-gas injected into liquid tin at 300 °C using a submerged porous sparger at feed gas flow rates between 10 mln/min and 200 mln/min were found to have a bubble rise velocity in the range of about 16 cm/s up to about 24 cm/s. The bubble rise velocities tend to increase towards higher flow rates, yet only at a small

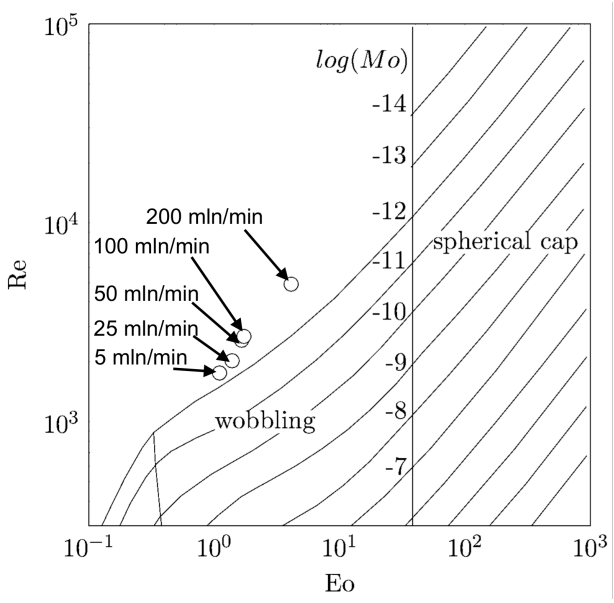

Figure 5.10: Graphical correlation for indicating the bubble regime of a two-phase flow system on the basis of the non-dimensional numbers Re, Eo and Mo.

inclination. Correspondingly, the bubble frequency was found to increase at a higher, continuous inclination. Whereas the lowest flow rate of 10 mln/min yielded in a frequency of about 0.4 Hz, 200 mln/min yielded in a frequency of about 1.2 Hz. Furthermore, with reference to fig. 5.9, the average bubble diameter was found to increase towards higher flow rates, starting from about 3 mm at the lowest flow rate and reaching 6 mm at the highest flow rate. Obtained results are in principle agreeing with the findings of Andreini et al. [65].

Chapter 6

Evolution of the reactor design and conducted experiments

► The present chapter explains the process of designing and operating a bubble column reactor using liquid tin as continuous phase for the purpose of hydrogen production by thermal decomposition of methane.

Based on the outcome of chapter 3, the process of thermal decomposition of methane shall preferably be realized in the presence of liquid tin. Here, liquid tin is provided as continuous phase, into which the pyrolysis gas, methane, is dispersed. Since methane decomposition is known to already slightly occur at methane temperatures higher than about 300 °C[1], it is generally advantageous to inject methane at a temperature close to this value, to reduce heat-up processes within the reactor. Simultaneously, the formation

[1] This temperature was later raised to about 550 °C, as experiments showed no carbon formation even for long experiment durations

of premature methane decomposition in the feed tubes and gas dispersion devices must be avoided, due to the associated solid carbon formation and the accompanied risk of reactor blockage. In view thereof, the methane was fed to the reactor via an external and temperature controlled feed tube, the feed tube leading to a gas injection device which was provided at the reactor bottom. The previously introduced reference-study, namely the study of Serban et al. [5] used a substantially different reactor concept. Here, a reactor-inner sparger was used, mounted on top of the reactor and extending almost to the bottom of the reactor whilst being partly submerged in the liquid phase. Moreover, the herewithin presented reactor design further differs from Serban's reactor in that the gas dispersion device is not of a cylindrical sparger design, but either a porous disc or a single hole orifice. The technical difference of this feature is that the total vertical distance to be traveled is identical for all gas bubbles. As a further distinguishing feature, it was desired to provide gas bubble residence times within the liquid metal phase of at least a few seconds which resulted in a envisaged liquid metal filling height of about 1000 mm. In this matter, the experimental findings as discussed in the previous chapter 5 have been utilized. Also, a liquid metal temperature of up to 1000 °C was desired to be achievable with the envisaged reactor. The realization of the explained desired aspects of the reactor, however, led to a variety of technical problems to be solved, as explained in the subsequent chapters. Additionally, a method for filling the reactor with liquid tin and a method for operating the reactor for TDM experiments have been developed.

6.1 General facility specifications

The objective was to remotely monitor and control the experimental facility and at the same time to have a platform that allows a modularly exchangeable setup, containing the instrumentation, gas supply and heating components, provided to support the reactor operation. For this purpose, a measuring cabin was built, comprising an external gas storage for methane, the calibration gas mixtures and Ar-gas. The gas was led from the external storage to the inside of the cabin, where a framework for receiving the reactor vessel was provided. The gas feed was monitored and controlled using pressure sensors, electronic switching valves and volumetric flow meters. For the reactor heating, an oven or heating wires have been applied. The facility was monitored and controlled using a Siemens SPS unit in combination with a custom-made LabVIEW program for storing the process data during operation. The sampling rate was set to 1Hz. Gas analysis was achieved by using a gas chromatograph, which was operated independent from the facility. The facility framework was continuously optimized in between various experimental campaigns, as shown in the subsequent sections.

6.2 General reactor specifications

According to the preliminary theoretical considerations introduced previously within this thesis, a liquid tin bubble column reactor operated at temperatures in the range of 700 - 1000 °C and comprising a methane injection device for flow rates in the range of 5 - 200 mln/min was desired. Although liquid metals in general have very high surface tensions, liquid metals and also tin have the tendency of creeping into very fine pores and gaps, which is accounted to the good wetting behavior especially for high temperatures. In the

case of attaching the gas injection device to the reactor vessel, great care is needed in order to avoid liquid tin leaking through the gas injector itself or installation gaps in between individual components. Several design options had been investigated for the leak-tight mounting of the gas-injection device to the reactor vessel. Mounting means comprising an attachable flange have the advantage of providing the gas injection device on one side of the flange and the reactor vessel on the other side. However, flange-type mounting means have the drawback of requiring a flange seal that is operable at reaction temperatures of up to 1000 °C. As an alternative, mounting the gas injection device to the reactor vessel therefore may further be achieved by connecting the gas injection device to the reactor bulk using an adhesive bonding technology, such as glass or metal welding. A first material composition considered a quartz glass tube comprising a welded-in porous quartz disc. The intended functionality of the porous quartz disc was to retain the liquid metal on the reactor bottom without leakage of liquid and to further allow methane gas to travel through the porous quartz disc and being dispersed into the liquid metal subsequently. However, mock-up experiments in water have shown that the quartz disc did not withstand the forces resulting from the pressure drop within its porous structure. After several minutes on stream, cracks were formed within the porous glass structure, leading to a disintegration of the quartz disc. Furthermore, liquid tin showed very poor wetting of quartz glass, which would have led to poor bubble formation at the sparger. In a second approach, the utilization of steel-metal joints[2] was investigated. Such application promised to separate the gas injector (steel) from the bulk material of the reaction zone (quartz). However, operation of said glass-metal conjunctions proved to be very sensitive towards temperature gradients and in particular transient temperature.

[2]Steel-metal joints are cylindrical tubes, connecting a steel tube with a quartz tube by several transition layers of different glasses

Parallel to this work, the resistivity of alternative metals and non-metals towards tin corrosion was investigated by the colleagues at the IHM, namely Dr. Annette Heinzel, Dr. Alfons Weisenburger and Prof. Georg Müller, considering e.g. carbonaceous materials and refractory metals. Because of the lack of suitable alternatives, it was decided to build a modular facility for the reactor operation and to use steel as bulk material in the first reactor generations. In the following sections, the evolution of facility and reactor design are explained in more detail. The most challenging design aspects may be summarized as follows.

1. Operation related design aspects
    (a) Filling concept of the reactor
    (b) Temperature management and insulation of the reactor
2. Reactor related design aspects
    (a) Bulk material, pre-operational treatment of bulk surfaces in contact with tin
    (b) Gas injection device including the joint to the reactor vessel
    (c) Gas outlet design including gas volume above liquid metal surface and gas outlet
    (d) Instrumentation of the reactor exposed to liquid tin, e.g. liquid tin temperature measurements, liquid tin level sensors, pressure sensors

6.3 Preliminary campaign 1.0: Reactor and facility features

In the first generation of the experimental facility, it was envisaged being able to change the reactor unit quickly without the need for replacing other components of the facility. The main reason for this was the expectantly strong corrosion of steel by liquid tin during operation of the reactor. For this purpose, a sump tank was installed which was connected to the reactor bottom via a riser pipe. After heating the sump tank and the empty reactor to 300 °C, liquid tin was pumped into the reactor by applying pressurized Ar to the sump tank. Also, in case of emergency, liquid metal could be flushed back into the sump tank. Fig. 6.1 shows a simplified scheme of the facility established for the 1.0 campaign. The layout of the facility allowed the injection of either pure methane (99.995 Grade 5.0, AirLiquide) or Ar gas (99.9995 Grade 6.0, AirLiquide) through the sparger. The index enumeration of the facility instrumentation is defined as follows. Instrumentation in direct contact with liquid metal is referred to with the index 1. Instrumentation of the gas supply framework has an index of 2, whereas the sump tank instrumentation is referred to by the index 3. Reactor heater instruments have the index 4.

Both the methane and Ar flow was controlled by flow meters $\mathrm{F}_{2.2}$ for Ar and $\mathrm{F}_{2.1}$ for methane with a range of 5 - 200 mln/min. The flow direction was controlled by pneumatic valves $\mathrm{V}_{2.\mathrm{i}}$. The gas flow prior and post the reactor unit was also monitored by pressure sensors $\mathrm{P}_{2.1}$ and $\mathrm{P}_{2.2}$ and the thermocouples $\mathrm{T}_{2.1}$ and $\mathrm{T}_{2.2}$. Furthermore the gas supply comprised several hand valves HV_{i} and over pressure safety valves Y_{i}. All off-gas pipes were connected to a common chimney. By means of a switching valve W_1, the effluent gas flow was deviated into the gas chromatograph. The reactor heaters $\mathrm{H}_{4.\mathrm{i}}$

were controlled by the corresponding thermo couples $\mathrm{T_{4.i}}$; $\mathrm{H_{1.8}}$ and $\mathrm{H_{1.9}}$ represent the heaters needed for the lower membrane of the difference pressure sensor $\mathrm{PD_{1.1}}$. Several level sensors $\mathrm{L_{1.i}}$ were attached to the reactor, in order to identify the liquid metal filling height. The sump tank was connected to the reactor by a heated riser pipe comprising the standard-open pneumatic valve $\mathrm{V_{3.1}}$. On behalf of the manually operated Ar feed, the sump tank could be pressurized with Ar gas in order to force liquid metal into the reactor via the riser pipe. For this purpose, the pressure sensor $\mathrm{P_{3.1}}$ and two level sensors $\mathrm{L_{3.1}}$ and $\mathrm{L_{3.2}}$ were installed. Filling the reactor for operation was achieved by several work steps including:

1. Heating all reactor components,
2. Flushing,
3. Pressurizing the sump tank to fill the reactor
4. Disconnecting the sump tank from the reactor.

During the heat-up of the reaction zone to desired operation conditions, Ar was fed to the sparger. As soon as the envisaged temperature level was reached, the Ar flow was set to zero and methane was applied to the sparger. Taking into account the estimated gas residence time in all pipes and reactor sections, the three-fold of the estimated residence time was taken into account, until a GC measurement was conducted. Prior to each measurement the switching valve $\mathrm{W_1}$ was set to "GC".

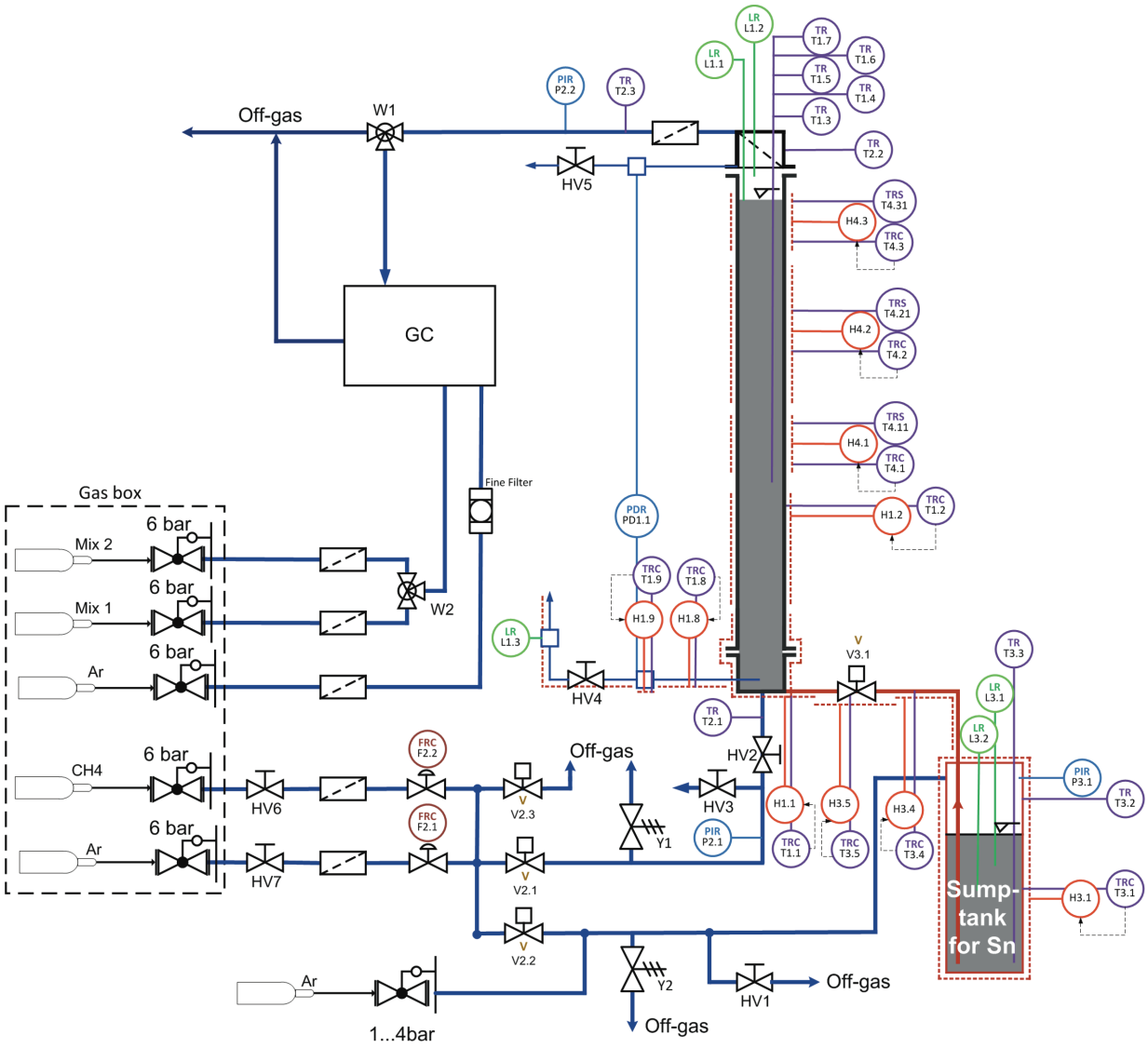

Figure 6.1: Schematic view of the 1.0 facility

6.3.1 Reactor features of generation 1.0

The first reactor generation was made of a 316 stainless steel tube with an inner diameter of 37.2 mm and a wall thickness of 2.6 mm. For practical purposes, the gas and liquid metal supply pipes were attached to the reactor tube using a Garlock flange. The off-gas and instrumentation ports on top of the reactor were attached accordingly, see fig. 6.2. The total filling height of the liquid metal inventory was estimated to be in the

range of 998 and 1050 mm. More information regarding the reactor dimensions may be found in the appendix 12. No surface treatments of the bulk material have been applied. For the purpose of reducing tin corrosion at the porous gas injector, the reactor tube is divided in to two temperature sections, as follows. In the 'cold' section at about 400 °C, the tube is heated by a detachable 300 W wire heater. In the 'hot' section, the reactor tube is heated using a three-zone furnace. By means of such design it was desired to establish a temperature gradient between the hot reaction zone at 1000 °C and the gas injection level at 400 °C. The used sparger is identical to the sparger used for the bubble measurement experiments, see chapter 5. The sparger was welded on the tube using electron beam welding in order to minimize the heat inflicted to the porous structure during the welding process. The liquid metal thermo couples $\mathrm{T}_{1.3}$ - $\mathrm{T}_{1.7}$ were inserted to the reactor from the reactor top by means of 6 mm Swagelok connectors serving as instrumentation ports. Five 0.5 mm type K thermo couples were mounted onto a common supporting rod according to the shown sensor heights as shown in fig. 6.2. The level sensors were also mounted using two instrumentation ports on top of the reactor. Laterally of the reactor top, the off-gas tube as well as the gas sided membrane of the difference pressure sensor were attached.

6.3.2 Lessons learned from the 1.0 campaign

Filling the reactor with liquid metal was successfully achieved according to above defined work steps. However, operation of the reactor had to be terminated after 30 hours on stream in total, due to liquid metal solidification inside of the reactor and inside of the off-gas tube. After about eight hours of operation including the time needed for heat-up of the reactor, transient bubble eruptions could be observed by the feed gas pressure

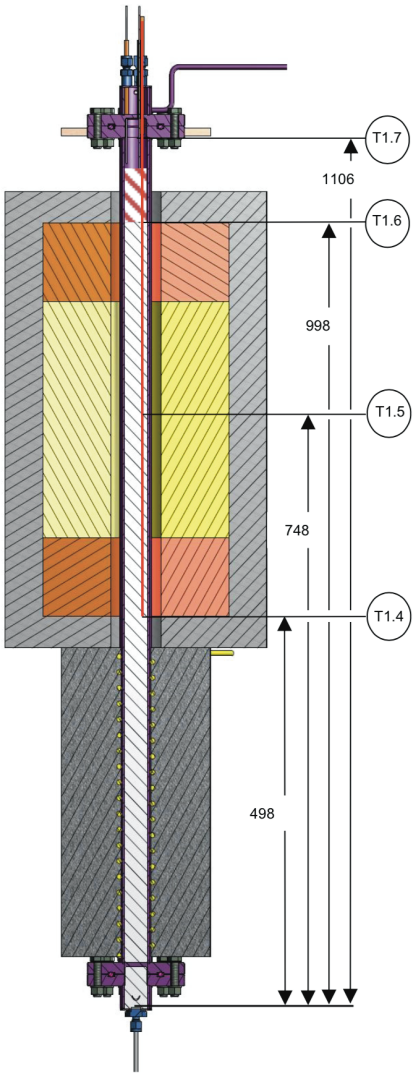

Figure 6.2: Schematic view of the 1.0 reactor

and also acoustically. Such eruptions were most likely related to partial solidification of tin alloys in the liquid phase or corrosion products which were blocking the gas flow through the sparger. During the post-experimental reactor analysis, it was found that an irregular distribution of tin and tin-alloys was present inside the reactor, see fig. 6.3. It can be observed that liquid metal reached all the way to the reactor top and gas was accumulating in large volumes. Particularly sections 9, 10 and 11 allow an interpretation of the observed, rather unexpected tin distribution inside of the reactor: prior to cooling

down the reactor, the sump-tank valve $V_{3.1}$ was opened, which should have forced all liquid tin flushing back into the sump tank. Even though all surface structures in contact with tin featured temperatures of 300 °C or higher, only a small portion of tin flushed back, namely the gaps of sections 9 and 10. Also section 11 comprises a small tilted gap, facing in the direction of the sump tank supply pipe. The rest of the liquid metal was obviously not in a liquid state at 300 °C, which is an indication for a drastically changed tin-alloy composition.

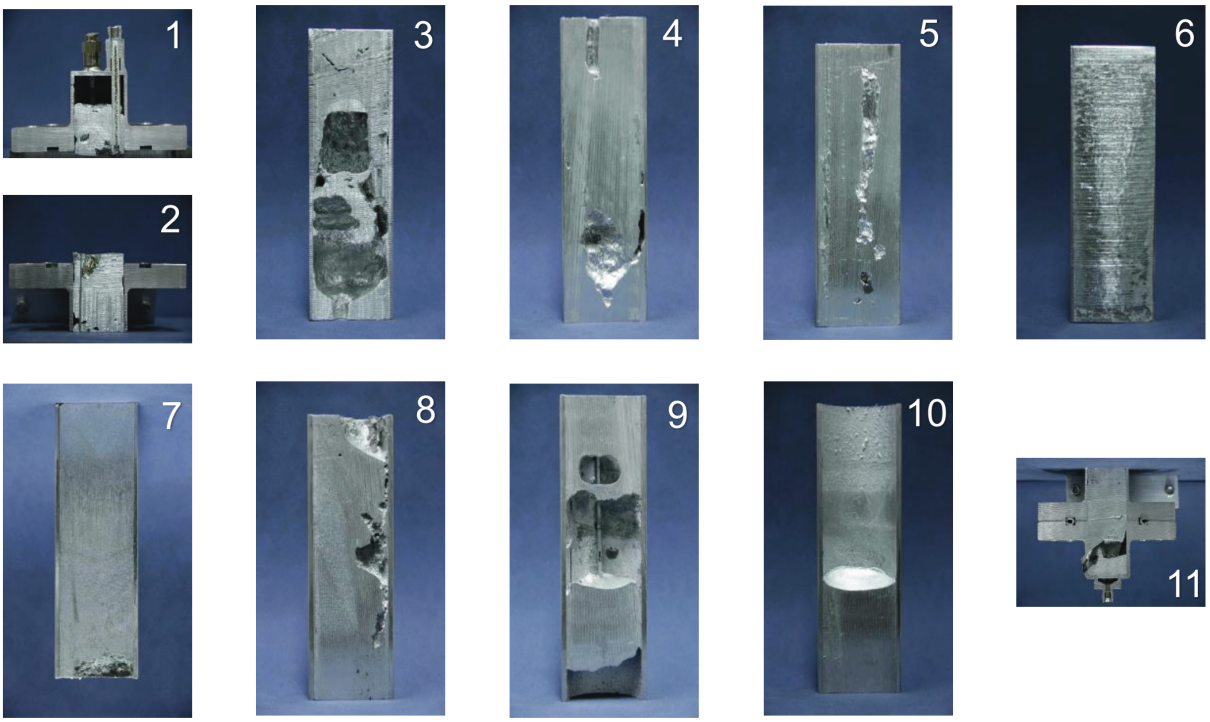

Figure 6.3: Axial cross-section of the 1.0 reactor intersections post-experiments. Section numbering from top to bottom

The lessons learned during campaign 1.0 may be summarized as follows.

- 316 stainless steel was severely attacked by liquid, corroding almost 80% of the tube wall at the hot zone within 30h of operation. This has been found by post-test analysis of the reactor, see fig. 6.4. Consequently, and following parallel material

investigations from Weisenburger et al. [69], for the next reactor generation it was decided to use a steel containing less Ni, which will be explained in the following sections.

- Formation of tin alloys with a higher melting point than tin were found to have a substantial impact on the facility design if steel is exposed to liquid tin.
  - The two-fold temperature concept proved inefficient due to solidification of tin alloys
  - Sump tank operation at temperatures higher than 300 °C is not useful, due to tin corrosion.
- Liquid metal solidification inside the off-gas tube used in the 1.0 experimental campaign proved that the design needed an efficient droplet splashing protection.
- The sparger proved good resistivity towards liquid tin corrosion. Microscopic analysis have shown an intact sparger surface, which was covered by FeO oxides, serving as cladding of the metal.
- Although much of the reactor bulk material was dissolved by tin corrosion, the thermo couples showed good resistivity towards tin corrosion.
- The level sensors proved to be unreliable, since liquid metal tends to solidify and agglomerate on the sensors which led to misleading signals, triggered by short-circuits between the reactor wall and the sensors.

Due to the poor operation conditions of the first experimental campaign, no useful data regarding methane conversion was gained.

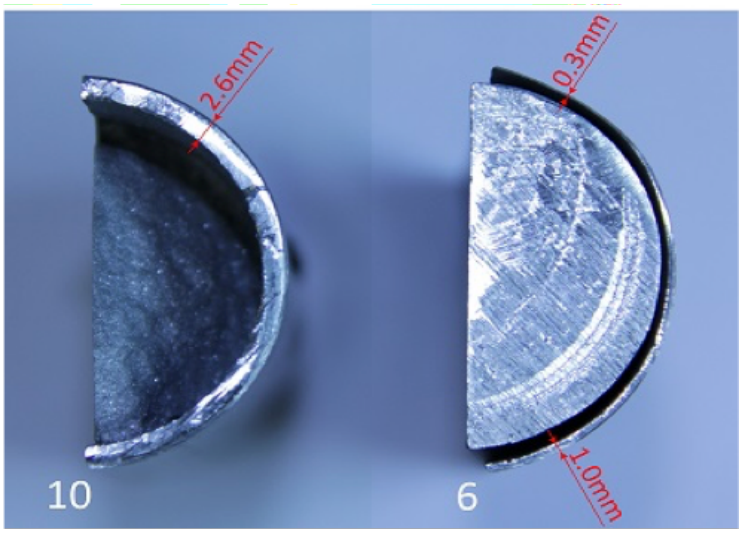

Figure 6.4: Corrosion attack on the reactor wall after 30 hours of operation at the hot section (right) compared to the reactor wall at the cold section (left)

6.4 Preliminary campaign 2.0: Reactor and facility features

6.4.1 Reactor features of generation 2.0

Based on the experiences from the first reactor generation, the main objective of the consecutive 2.0 campaign was to reduce complexity of the facility and the reactor itself. According to the findings of the previous generation, the sump tank unit was discarded entirely and the lower flange of the reactor was removed. Instead of charging the reactor with liquid tin, it was decided to charge the reactor tube with granular tin in cold condition. By such means, both the level sensors and the difference pressure sensor could be removed. Since liquid tin shall not be in contact with oxygen due to SnO formation, all of the required amount of tin needed to be inserted into the reactor prior to heating up the tube. Therefore, the reactor tube was temporarily enlarged by about

30% in length, taking into account the porosity of granular tin. After melting, the large gas phase above the liquid metal surface was considered to serve as droplet protection. Droplet freezing in the off-gas tube was also reduced by the installation of a droplet baffle. A major change regarding the reactor design was the replacement of 316 SS bulk material to 1.4749 steel[3], on which the sparger was welded on in similar fashion as in generation 1.0. Heating the reactor was achieved using wire heaters only as shown in fig. 6.6. Furthermore, a gas preheater was installed in order to control the feed gas temperature. The thermo couple instrumentation design of generation 1.0 was used without major changes. A scheme of the generation 2.0 facility is provided in fig. 6.5.

6.4.2 Lessons learned from the 2.0 campaign

Concerning the performance of the 2.0 experiment campaign, different conclusions can be drawn. After about eight hours of initially heating the reactor, the gas flow through the sparger was blocked due to corrosion of the sparger. Later during operation, the thermo couple instrumentation was also corroded by the liquid metal, leading to a complete blind-out of the reactor-inner temperature values after about 48 hours on stream. The increased corrosion of the sparger and the thermo couple instrumentation was mainly a result of the increased corrosion-resistivity of the reactor wall. Since less steel alloys are dissolved out of the reactor wall, the corrosion is increased on less corrosion-resistant components, namely thermo couple installations and the sparger. Furthermore, the temperature at the sparger was increased due to a different insulation concept in comparison to campaign 1.0.

At eight hours, operation was terminated due to sparger blockage. As a work-around,

[3] 1.4749 is a high temperature chromium steel with a very low Ni-content hence a better expected corrosion resistance towards tin corrosion

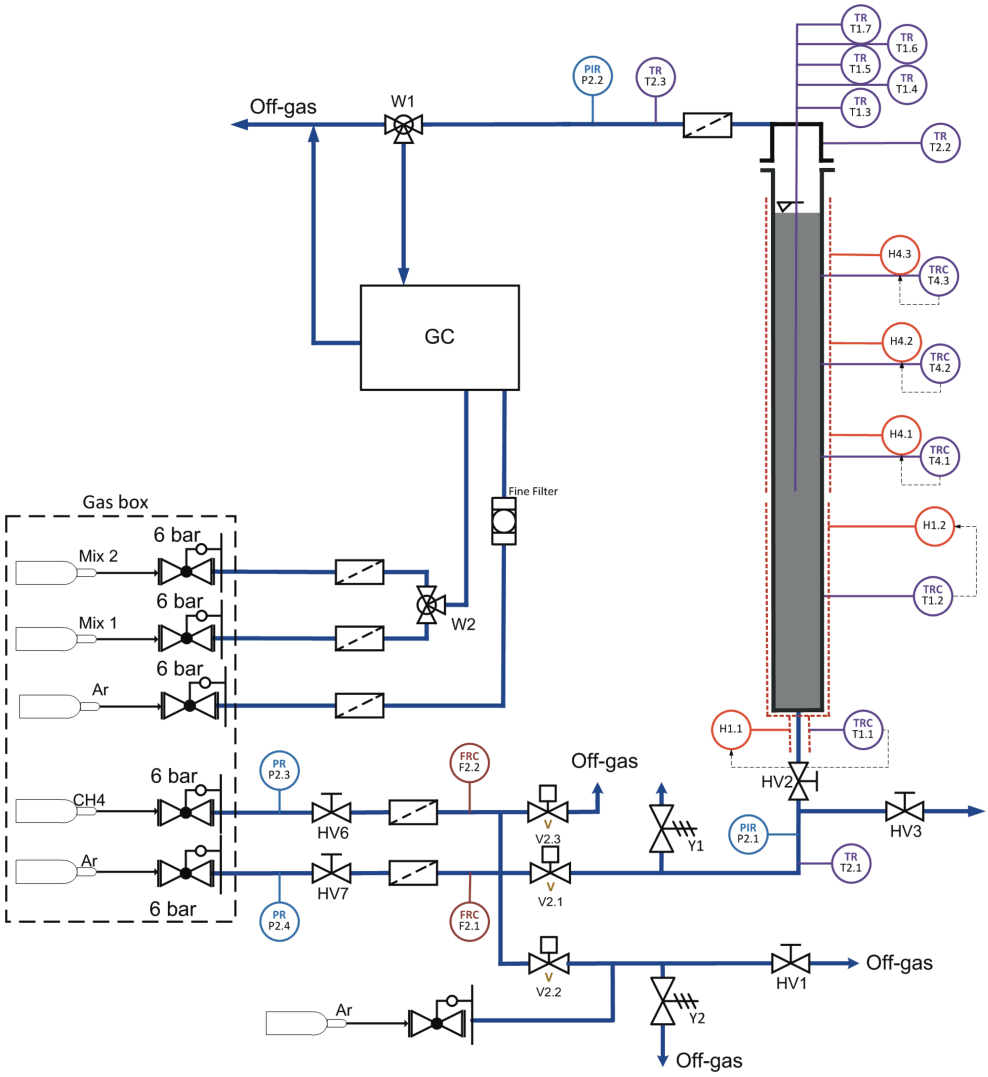

Figure 6.5: Schematic view of the 2.0 facility

the facility was shut down and partly disassembled. Through the now gas leak-tight corroded sparger disc a hole with a diameter of 1 mm was drilled, yielding in a single orifice gas injection device. As a conclusion, it was decided to repeat the 2.0 experiments including several minor improvements:

- A single hole orifice was found to allow a much more stable operation compared to the porous sparger

- Thermo couples must not be exposed to liquid tin directly, due to tin corrosion
- The large reactor-inner gas volume was found to be inefficient due to the very large gas residence times within the tube, particularly for low methane flow rates

Although several individual measurements were conducted during the 2.0 campaign, no complete data set was obtained. Still, operation experience could be gained and several improvements in the control system had been conducted. For the sake of maintaining readability however, said improvements shall not be subject of this chapter.

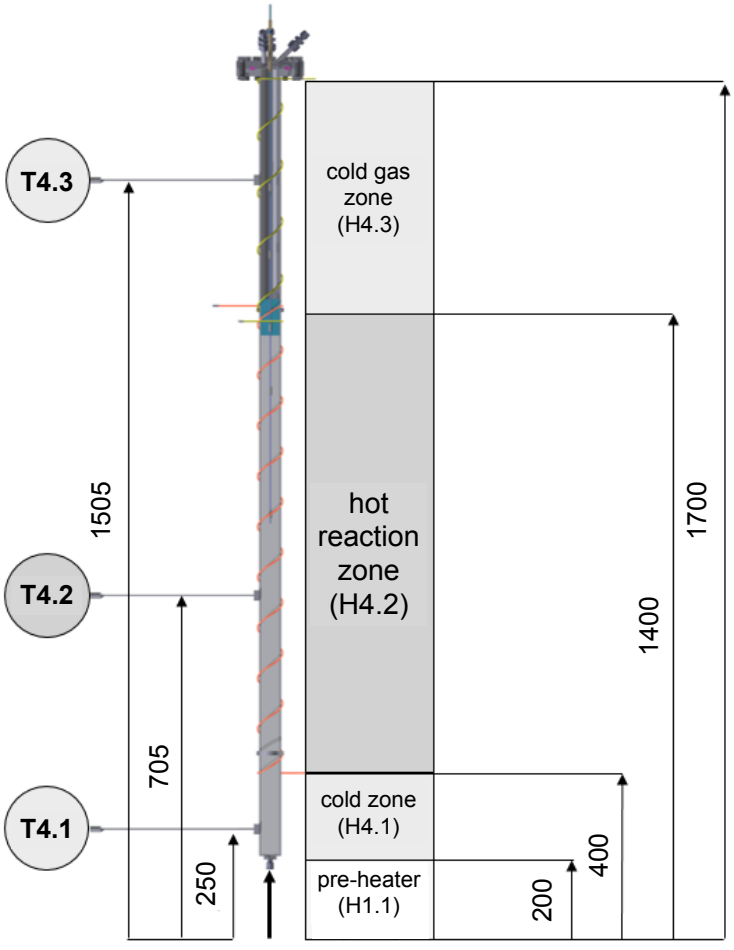

Figure 6.6: Schematic view of the 2.0 reactor

6.5 Experimental campaign 2.1: Successful runs with liquid metal

According to the items listed previously, the major improvements of version 2.1 are defined by the reduced gas volume inside of the reactor, the utilization of the single hole orifice and an alumina tube, in which the thermo couples $\mathrm{T}_{1.3}$ and $\mathrm{T}_{1.4}$ had been inserted and used for measuring the liquid tin temperature during operation. Compared to generation 2.0, the overall reactor length was shortened by 300 mm. Filling the reactor despite the reduced volume was achieved attaching a temporary extension tube on top of the reactor prior to tin melting. Furthermore, the reactor inner surfaces were exposed to hot air at 600 °C for eight hours, in order to promote the formation of an oxide layer for cladding purposes. More detailed, the filling procedure can be summarized as follows.

6.5.1 Conducted experiments: Measurements scheme and process data

After fully charging the reactor with tin and a subsequent heat-up phase, over the course of two consecutive days, the campaign 2.1 was carried out by means of a slightly improved facility infrastructure which is depicted in fig. 6.7. The conducted experiments were carried out using one tube reactor at different temperatures and different flow rates and, in the case of experiments at 900 °C, with a lowered liquid metal filling height. During the heat-up and in between individual measurement campaigns, the reactor was flushed with pure Ar gas to minimize carbon formation inside of the reactor. Prior to methane injection, the reactor surface temperatures as well as the liquid metal temperature were first kept at a uniform level. As the targeted temperature was reached,

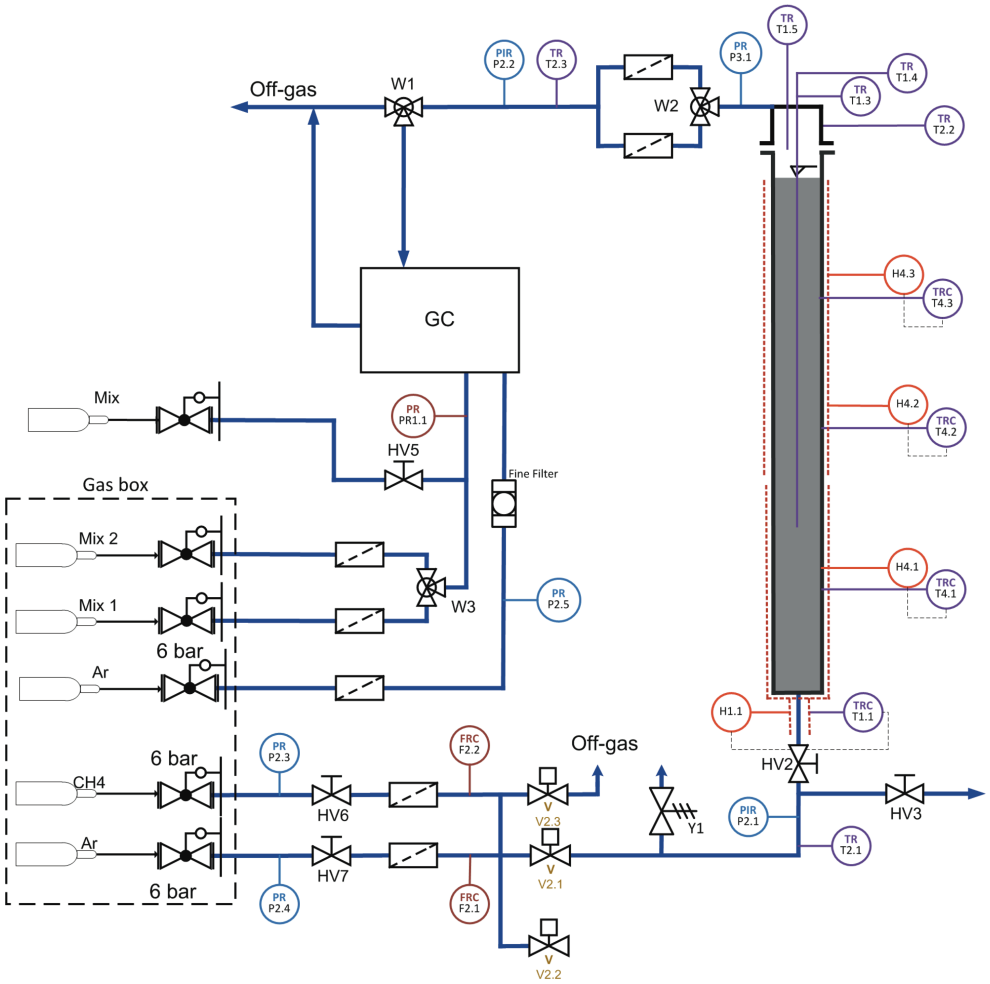

Figure 6.7: Schematic view of the 2.1 facility

pure methane was injected and the threefold of the product gas dwell time was allowed before the gas analysis.

In fig. 6.9, a selection of the monitored temperature, pressure and flow-rate data throughout the two days of experimental operation is shown. For clarity and improved readability purposes, not all of the data is shown. For a detailed representation of the below shown data, see also fig. 12.1 and 12.2 in the appendix. The latter figures further include the real-time events, at which the gas samples for the gas composition analysis had been retrieved from the effluent gas stream. Fig. 6.9 shows reactor-inner tempera-

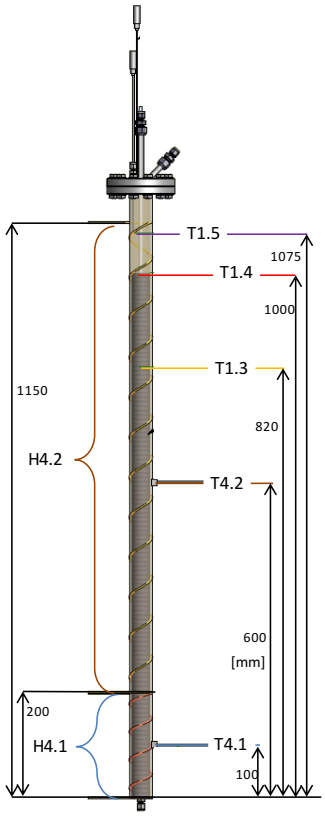

Figure 6.8: Schematic view of the 2.1 reactor

ture values ($\mathrm{T}_{1.3}$ and $\mathrm{T}_{1.5}$), reactor outer temperature values ($\mathrm{T}_{4.1}$ and $\mathrm{T}_{4.2}$) as well as the methane feed flow rate ($\mathrm{F}_{2.2}$) on the primary y-axis, and the absolute methane gas pressure ($\mathrm{P}_{2.1}$) on feed side, facing away from the reactor, on the secondary y-axis. The position of the above mentioned thermo couples is provided in fig. 6.8, representing the reactor of the 2.1 generation.

In fig. 6.9 the reactor-inner thermocouple $\mathrm{T}_{1.5}$ indicates a temperature decrease after about 630 minutes of reactor operation time. Several minutes later, a further reactor-inner thermocouple, namely $\mathrm{T}_{1.3}$ also indicated a temperature decrease; yet to a smaller extent. Apart from that, all of the other operation parameters were fine; hence, operation was not terminated. This temperature decrease was related to a leakage of liquid tin

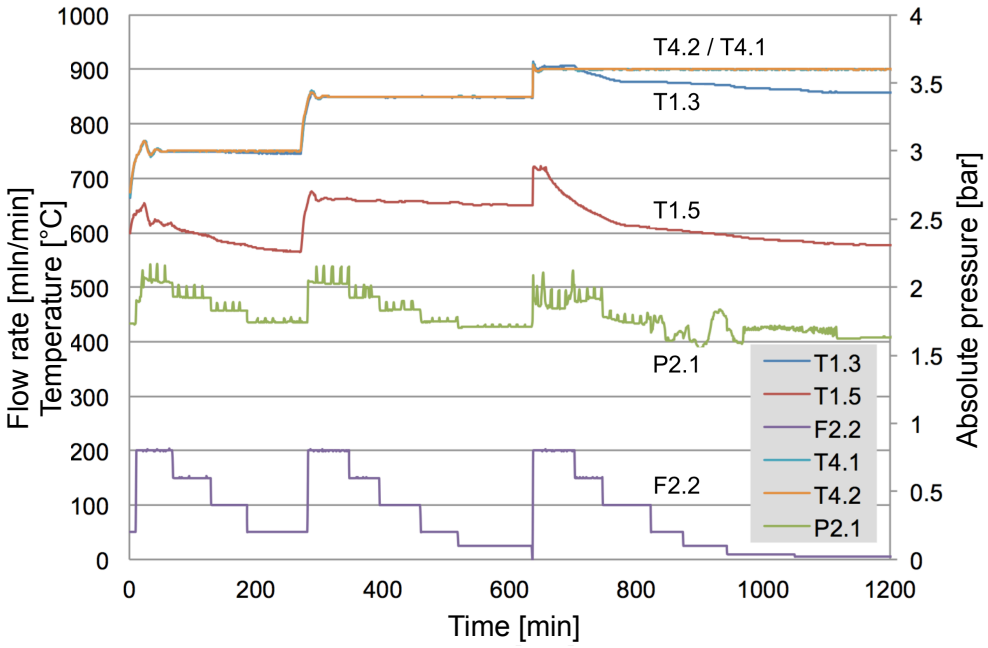

Figure 6.9: Overview of a selection of the obtained process data for runs with liquid metal.

through the reactor wall which was a result of tin-induced steel corrosion. It was later found that due to this leakage, the filling height of tin was reduced to 600 mm. The reduced filling height was also considered in the data analysis and was found to have not affected the gas flow characteristics.

Table 6.1 provides an overview of all measured effluent gas compositions at a given temperature, methane feed flow rate and liquid metal filling height. Furthermore, the gas flushing time is provided, representing the three-fold gas residence time of methane gas to travel through the entire reactor volume and the gas pipelines in between the reactor and the location of the gas chromatograph. With respect to the long residence times at low flow rates, the full range of 5-200 mln/min was only realized in the 900 °C-campaign, in order to limit the exposure of the reactor inner surfaces to corrosion attack. Because the risk of tin leakage at the orifice is increasing with lowered flow rates, runs with 5 mln/min were only conducted during the 900 °C-campaign. Indeed, small quantities of

solidified tin were found in the orifice feed pipe in the post-examination of the reactor.

	[mln/min]	200	150	100	50	25	10	5
($H_{\mathrm{LM}} = 1000$ mm)	750 °C	4x	4x	4x	6x	-	-	-
($H_{\mathrm{LM}} = 1000$ mm)	850 °C	5x	3x	4x	4x	6x	-	-
($H_{\mathrm{LM}} = 600$ mm)	900 °C	6x	4x	6x	3x	4x	4x	4x
Flushing time t_{flush}	4	5	8	15	29	70	140	

Table 6.1: Conducted measurement schedule and the corresponding flushing time t_{flush}

6.5.2 Conversion results obtained with the liquid metal bubble column reactor

For every measurement, a pre-defined volume of the product gas was deviated from the effluent product gas flow and being analyzed in terms of gas concentrations by means of gas chromatography. Specifically, the mole-% of methane, ethane, ethylene and acetylene have been measured. The gained gas concentrations therefore only refer to the gas phase, wherein the formation of the by-product carbon was not measured. Results show that for runs with liquid tin, the amounts of the intermediate products ethane, ethylene and acetylene were not within the measurable range of the gas chromatograph, i.e. below 0.1vol-%, therefore only methane and hydrogen concentrations are represented in the following data. The gas chromatograph was calibrated from 0.1vol-% to 20 vol-% in the case of hydrogen, and from 0.1vol-% to 100 vol-% in the case of methane. More information regarding the gas chromatograph calibration can be found in the Appendix 12.

In fig. 6.10, the methane conversion results are presented as a function of the flow rate for various temperatures. The error bars shown for each data point represent the spread in concentrations of the repeated measurements. Although methane conversions are very low at high flow rates, an increase in conversion for higher temperatures could

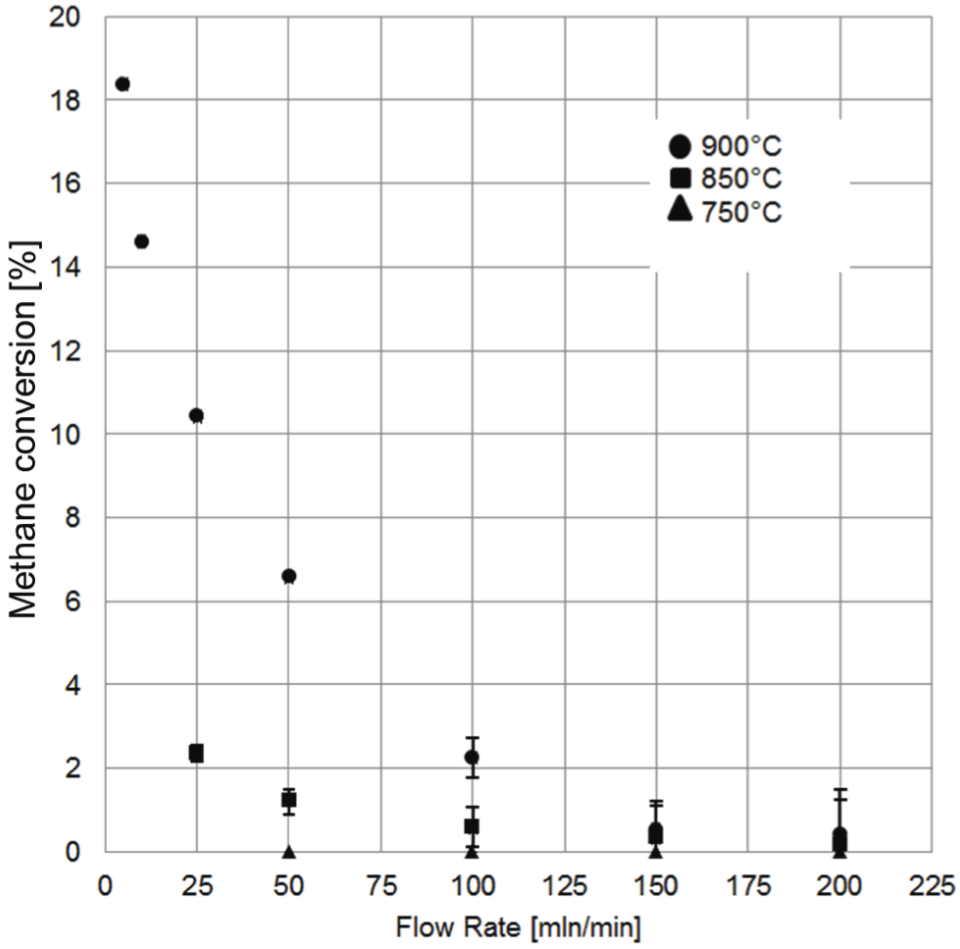

Figure 6.10: Obtained methane conversions during the experimental runs. The 900 °C experiments were conducted with a reduced liquid metal filling height and an increased PFR- section

still be detected. As shown, methane conversion is favored for reduced flow rates and increased temperatures. In view of the observations made during the bubble rise and bubble size experiments, discussed in chapter 5, it is unlikely that the observed increase in methane conversion is driven by a change in flow rate. As a reminder, it was found that a change in flow rate is merely compensated by an increase in bubble frequency, hence more bubbles of similar shape and rise velocities are formed. Consequently, the flow-rate dependency is more likely to be related to methane conversion, occurring in the hot gas section above the liquid metal surface and within the reactor. It further seems as if the liquid phase in phase must have a rather small impact on the conversion rate

in general. In particular, the 900 °C experiments with a 40 % reduced liquid metal filling height show a decent methane conversion. However, at the time of analyzing the 900 °runs of the 2.1 generation experiments, it was not clear which impacts are in fact causing the increased conversion to which extent. For the 900 °runs, several changes had been made to the system, namely

- the liquid metal temperature was raised to 900 °C;
- the liquid metal filling height was reduced from 1000 mm to 600 mm;
- as a consequence of the reduced liquid inventory, the gas phase section inside of the reactor was increased accordingly; and
- the temperature distribution within the gas phase section was different.

Again, in view of the measured conversion rates, it was observed that said changes in total led to an substantial increase in conversion. In the context of this thesis, the main focus lies on the impact of the liquid metal on the overall conversion. Therefore, for comparative purposes, it was decided to conduct experiments with an "empty-tube" reactor of similar shape and operation conditions. The comparison itself is conducted by testing the previously defined hypotheses. The general idea was to identify, to what extent the observed flow-rate dependencies of runs with liquid tin and runs with an empty-tube reactor differ from each other. The higher the similarity, the smaller the fraction of methane conversion may be attributed to the liquid phase and the more it may be attributed to have been occurred in the gas phase of the reactor. In the following, the empty-tube reactor experiments are referred to as generation 2.2 experiments, or campaign 2.2. As a side note, due to the different temperature distributions provided in the two experimental campaigns 2.1 and 2.2, an ideal isolation of flow rate and temperature-driven

dependencies of the measured methane conversion is difficult to assess.

6.6 Experimental campaign 2.2: Runs without liquid metal

By means of campaign 2.2, several aspects were examined. The primary purpose of the campaign was to measure methane conversion occurring in the gas phase section with a design similar to that of campaign 2.1. Accordingly, dimensions and reactor bulk material of the 2.2 reactor are identical to the 2.1 reactor without the liquid metal section, see fig. 6.12 for more details. In order to obtain maximum comparability in terms of the reactor-inner volume with the 2.1 experiments, reactor generation 2.2 again comprised an $\mathrm{Al_2O_3}$ alumina cladded thermo sensor that is identical to the one used in generation 2.1 on the inside of the reaction volume. The reactor then was integrated into the reactor facility, as depicted in fig. 6.11.

6.6.1 Conducted experiments: Measurements scheme and process data

The examined experimental runs for methane decompositions were chosen corresponding to campaign 2.1, but with a more complete range of flow rates for each temperature level. Similar to the measurement procedure used in the bubble column experiments, the three-fold of the residence time at steady-state conditions of a given temperature and flow rate was applied prior to a conversion measurement, whereas each conversion measurement was repeated three consecutive times. Contrary to previous runs

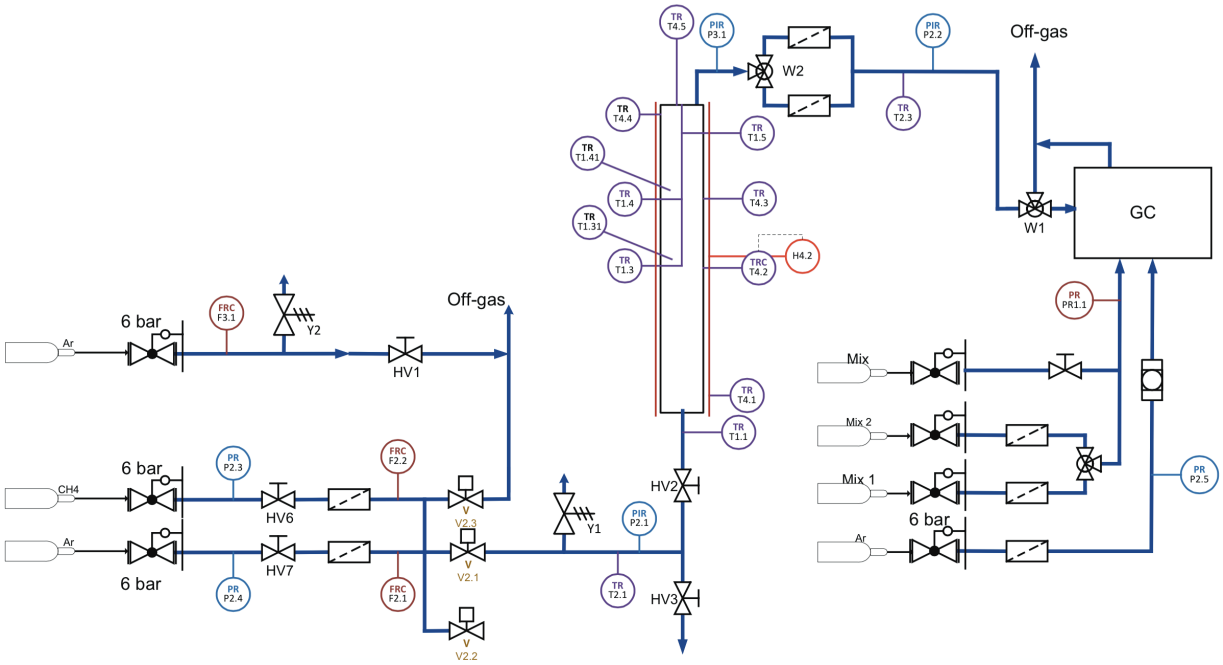

Figure 6.11: Schematic view of the gas phase facility 2.2

with liquid metal, the empty-tube section of the reactor was actively controlled by the outer surface temperature $\mathrm{T}_{4.2}$, allowing constant operation conditions for all applied flow rates. The used reactor for the gas phase experiments is identical in diameter and bulk material, comprising a tube height of 575 mm. As shown in fig. 6.12, four additional thermo couples had been attached to the reactor surface, namely $\mathrm{T}_{4.1}$ - $\mathrm{T}_{4.4}$ and two additional thermo couples had been inserted to the gas phase of the reaction volume, $\mathrm{T}_{1.31}$ and $\mathrm{T}_{1.41}$.

According to the runs conducted during generation 2.1 using the bubble column reactor, generation 2.2 experiments also investigated the same operation temperature ranges of 750 °C, 850 °C and 900 °C at methane feed flow rates in the range of 5 and 200 mln/min. Corresponding, theoretically calculated gas residence times inside of the reactor tube varied from 1 - 60 min, assuming pure methane and the application of the ideal gas law. Again, the process data was monitored and stored in real-time during

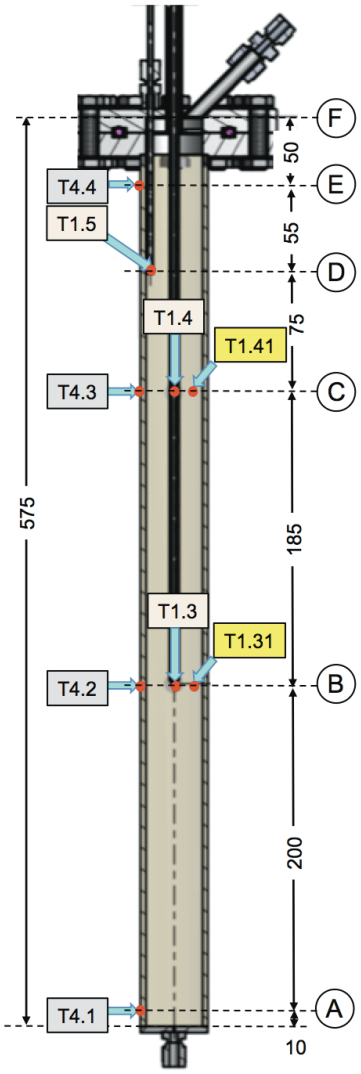

Figure 6.12: Instrumentation and dimensions of the reactor used for the blank tube experiments

the experiments. For a detailed depiction of said data, several plots are provided in the appendix, see fig. 12.3. The absence of liquid metal, hence the absence of corrosive or abrasive events occurring inside of the reactor, yields in the advantage of a practically infinite possible reaction duration. Therefore, for every measurement run and even for each of the temperature levels 750 °C, 850 °C and 900 °C, steady-state conditions could be achieved in a much shorter time frame compared to the 2.1 experiments.

6.6.2 Conversion results obtained with the empty-tube reactor

According to fig. 6.13, methane conversion shows similar dependencies as witnessed during the bubble column experiments. A more detailed discussion and comparison of model calculations will be given in section 8.3. For the blank tube experiments, each depicted measurement was repeated three consecutive times at a delay of 15 min. Relative errors of the samples from the mean value had been in the magnitude of $1 \cdot 10^{-3}$.

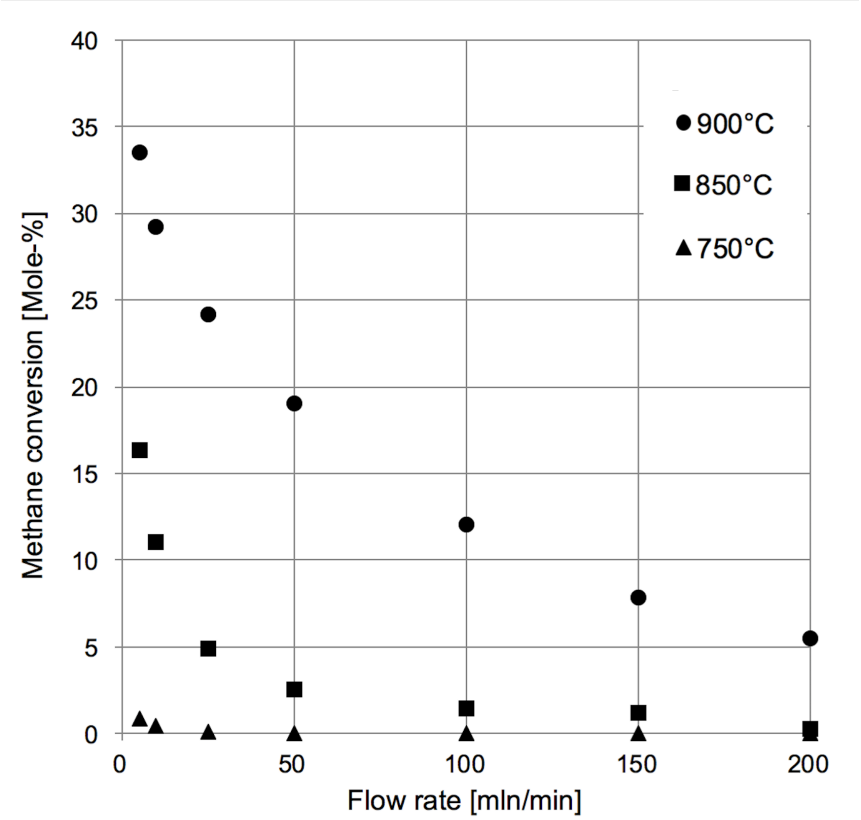

Figure 6.13: Methane conversion obtained during the blank tube experiments

During the blank tube experiments, at 750 °C, no intermediate hydrocarbons had been detected by the gas chromatograph. At 850 °C, at flow rates of 25 mln/min and smaller, ethane formation was detected. As shown in Fig. 6.14, ethane formation increased exponentially for lowered flow rates with the highest concentration being 0.27 mole-% at 5

mln/min. In the same plot, the molar concentration of hydrogen is referring to the right y-axis. During all conducted experiments, hydrogen concentration follows an exponential dependency for lowered flow rates, reaching up to 16%. At 900 °C experiments, ethane formation was detected already at residence times in the range 80 seconds, corresponding to a flow rate of 200 mln/min, see fig. 6.14. At gas residence times of about 160 seconds and higher, ethylene formation was also detected. Ethane concentration climaxed at a residence time of 630 seconds at about 0.9 mole-%. Higher residence times led to reduced formation of ethane. In fact, the lowest ethane concentration was observed at the highest residence time at about 52.5 min. Ethylene formation reached about 0.25% at a residence time of 26 min and dropped to 0.2% for twice the residence time. Due to the constant increase in hydrogen concentration, it is likely that the intermediate products decompose into hydrogen for sufficient gas residence times. As a general conclusion, it was observed that ethane is the first intermediate product among all considered C2-hydrocarbons, followed by ethylene- which is in accordance with the model according to equation 2.4 of a step-wise decomposition of methane via intermediate C2-hydrocarbons. Apart from the order of appearance of said intermediate products, the observed formation does not follow the same systematic compared to the formation of methane. Quite the contrary, it seems as if conversion is maximized for a specific gas residence time and operation temperature. Within the considered range of experiments, such optimum was identified for ethane to be at 900 °C at a gas residence time of roughly 10 min, which is equal to the applied flow rate of 25 mln/min. Ethylene formation was detected to be at a maximum at also 900 °C, yet at a gas residence time of about 26 min; corresponding to an applied nominal feed flow rate of 10 mln/min. However, due to the rather small amount of data a detailed analysis on product formation cannot be assessed. The conclusion that hydrogen is the dominant gaseous reaction product with a concentration more than one order of magnitude higher than any other, still holds

however and is important for the main purpose of the present work.

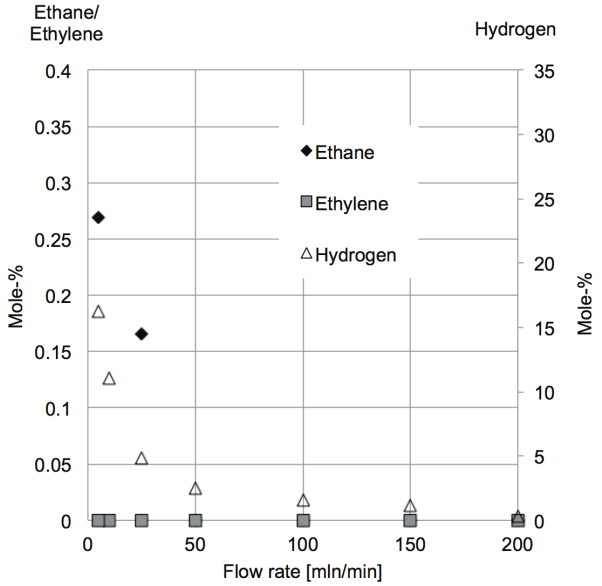

Figure 6.14: Formation of intermediate products and hydrogen during runs with a blank tube reactor at 850 °C. Hydrogen concentration is referring to the right axis.

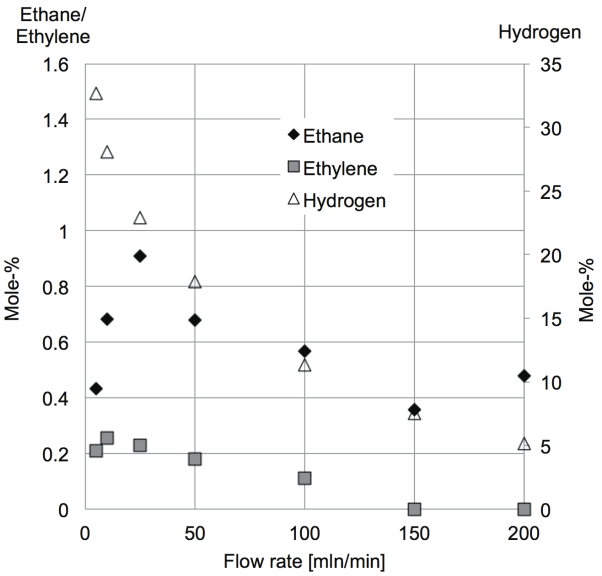

Figure 6.15: Formation of intermediate products and hydrogen during runs with a blank tube reactor at 900 °C. Hydrogen concentration is referring to the right axis.

Chapter 7

Modeling the process

► In the following chapter, thermochemical models used for the calculation of methane conversion in the investigated process are introduced. With respect to the different nature of two-phase and single-phase flows, a section-wise modeling approach of the reactor will be presented.

Previous sections introduced the reactor design and the chemical reaction kinetics based on different literature data. Although it was envisaged to investigate methane conversion in the liquid tin phase alone and to avoid parasitic conversion in the adjacent gas sections during the experiments, the actual system is more complex. Methane is desired to enter the liquid metal at high temperature, in order to minimize the time needed by the bubbles for the heat-up. If the feed gas temperature is too high however, the orifice is in the risk of being blocked due to carbon formation, which would trigger a reactor

malfunction. Furthermore, the conversion of methane directly above the liquid surface inside the reactor needs to be taken into account when analyzing the overall reactor performance and especially the applicability of a liquid metal bubble column reactor for the purpose of thermal cracking of methane. For the purpose of a better gas heat-up and conversion prediction as well as providing the basis for evaluating the generation 2.2 experiments, the considered liquid metal reactor of generation 2.1 was divided into four subsystems, as shown in fig.7.1. For each subsystem, suitable thermo-chemical models have been defined. After passing the controlled preheater, the feed gas flows through the orifice prior to injection. Subsequent to the time needed for bubbling through the liquid metal, the gas dwells inside the tube at high temperatures. In order to quantitatively estimate the impact of the individual subsystems, the introduced components will be explained in terms of their thermal and chemical behavior.

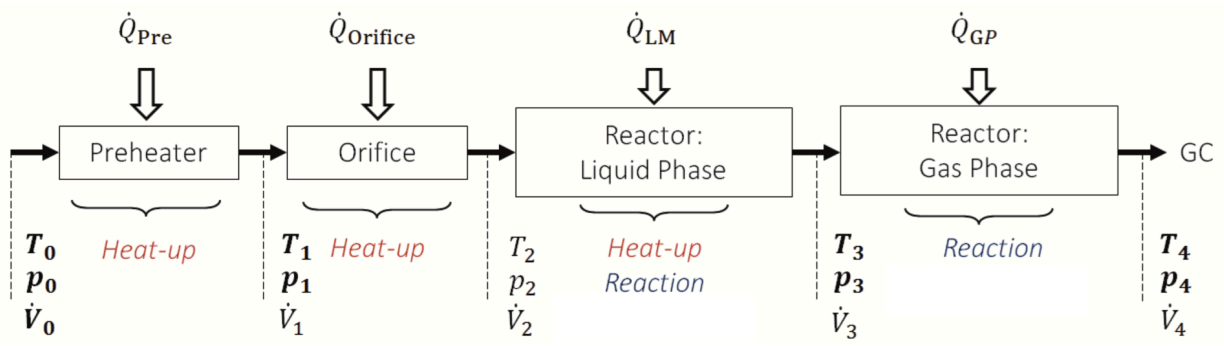

Figure 7.1: Subdivision of the experimental setup for the reactor generation 2.1 to the subsystems Preheater, Orifice, Liquid Phase and Gas Phase. The properties are referring to the gas phase; measured values are in bold letters.

7.1 Preheater and orifice

The preheater is controlled by the outlet temperature T_1, therefore this temperature serves as input parameter for the calculation of the orifice outlet gas temperature T_2. The

measured pressure in the gas phase p_1 results from the pressure losses at the orifice and is the same for the preheater and the orifice.

The subsystem orifice comprises the feed gas pipe with an inner diameter of 4 mm and a length of 26 mm and the orifice itself, being a 1 mm diameter hole in the reactor bottom plate, see fig. 7.2. Due to the proximity of the liquid metal and the solid reactor structure, the wall temperature of the orifice system is considered to be equal to the reactor surface temperature. As an assumption, chemical conversion during the flow through the orifice zones was considered negligible. This is substantiated by the fact that the inner surfaces of the orifice were found to be clear of carbon after the experimental runs. For the thermal calculation, the orifice is divided into zone “Feed” and zone “Orifice”, representing the feed gas tube and the orifice itself correspondingly, see fig. 7.2. Applying the flow rates 5 - 200 mln/min at standard conditions, the Re numbers are below 50, therefore laminar flow was considered in both zones. The used Nu-correlation for laminar flow in a cylindrical tube with a constant wall temperature is depending on the cross-section d and length L of the corresponding tube section. According to Von Böckh et al. [70], it can be expressed as a function of the dimensionless Re and Pr number for laminar conditions, since in the observed range of thermodynamic conditions, in the orifice, the Re-number of the flow is clearly below $\mathrm{Re}_{\mathrm{crit}}$. Furthermore, the Nu-correlation may be expressed by the heat transfer coefficient α, the heat conductivity λ and the length L.

$$\mathrm{Nu}_{\mathrm{d,lam}} = 0.644 \cdot \sqrt[3]{\mathrm{Pr}} \cdot \sqrt{\mathrm{Re} \cdot d/L} = \frac{\alpha \cdot L}{\lambda} \tag{7.1}$$

Equation 7.1 provides the heat transfer coefficient α which is then used to calculate the outlet temperature for each zone. This next step was calculated by means of the energy balance

$$\dot{Q}_{\mathrm{Orifice}} = \alpha \cdot A \cdot \Delta T_{\mathrm{WG}} = \dot{m} c_{\mathrm{p}} (T_{\mathrm{G,out}} - T_{\mathrm{G,in}}) \tag{7.2}$$

with the logarithmic mean temperature difference

$$\Delta T_{\mathrm{WG}} = \frac{T_{\mathrm{G,out}} - T_{\mathrm{G,in}}}{ln \frac{T_{\mathrm{W}} - T_{\mathrm{G,in}}}{T_{\mathrm{W}} - T_{\mathrm{G,out}}}}, \tag{7.3}$$

wherein T_{W} a constant wall temperature and $T_{\mathrm{G,in}}$ and $T_{\mathrm{G,out}}$ the characteristic gas inlet and outlet temperatures in the cross-section A of the corresponding tube section. In the presented case, the gas outlet temperature $T_{\mathrm{G,out}}$ of the orifice is calculated on behalf of the measured temperatures $T_{\mathrm{G,in}} = T_1$ and T_{W}.

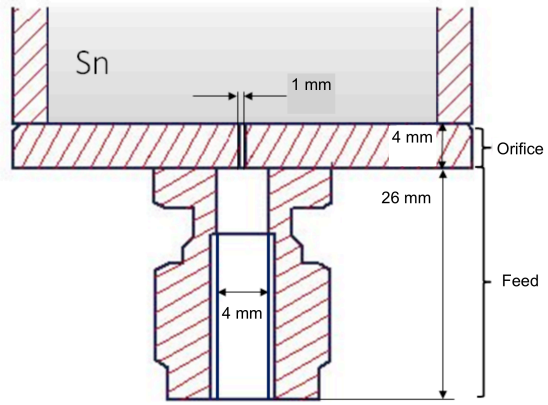

Figure 7.2: Cross-sectional view of the orifice used in the experimental setup

7.2 Liquid phase

Modeling the thermal process and chemical conversion in the liquid phase was realized by a finite difference solver, based the following assumptions, wherein

- The diffusion coefficient D, and the Pr-number are independent from temperature changes;
- The wall temperature T_{ref} measured outside of the tube is equal to the liquid metal temperature, according to the high thermal conductivity of liquid tin;
- The bubble rise velocity is constant during the rise of the bubble and independent of the applied gas flow, according to the results of chapter 5;
- The bubble has a spherical shape with a diameter of 5 mm, based on the findings of chapter 5;
- No convection inside the bubble, only heat conduction;
- The flow is calculated using the assumption of an ideal gas and Arrhenius' equation for the chemical conversion;
- The surface tension- induced pressure change inside the gas bubble is negligibly small, according to the Young-Laplace equation; and
- Gas bubble expansion due to methane conversion is neglected.

The total gas pressure of a bubble is defined as the sum of the gas pressure p_∞ above the liquid metal surface and the hydrostatic pressure of the tin. The material balance equation is defined as

$$\frac{\partial c_{\mathrm{CH_4}}}{\partial t} = \frac{1}{r^2} \cdot \frac{\partial}{\partial r} \left(r^2 \cdot D \cdot \frac{\partial c_{\mathrm{CH_4}}}{\partial r} \right) - k_0 \cdot c_{\mathrm{CH_4}}^n \cdot exp\left(\frac{-E_a}{\Re \cdot T} \right), \tag{7.4}$$

wherein $c_{\mathrm{CH_4}}$ represents the concentration of methane and D the diffusion coefficient. The variables k_0, E_a and n represent the pre-exponential coefficient, the activa-

tion energy and the reaction order. T is the total temperature. The energy conservation equation can be expressed as:

$$\rho_{\mathrm{CH_4}} \cdot c_{\mathrm{p,CH_4}} \cdot \frac{\partial T}{\partial t} = \frac{1}{r^2} \cdot \frac{\partial}{\partial r}\left(r^2 \cdot \lambda_{\mathrm{CH_4}} \cdot \frac{\partial T}{\partial r}\right) - h_f \cdot k_0 \cdot c^n_{\mathrm{CH_4}} \cdot exp\left(\frac{-E_a}{\Re \cdot T}\right) \tag{7.5}$$

wherein $\lambda_{\mathrm{CH_4}}$ is the heat conductivity of methane and h_f is the formation enthalpy. Both of the above stated equations 7.4 and 7.5 have been non- dimensionalized on behalf of the auxiliary parameters t^*, c^*, θ and r^*:

$$t^* = \frac{t}{t_{\mathrm{res}}}; \quad c^* = \frac{c}{c_0}; \quad \theta = \frac{T - T_{\mathrm{LM}}}{T_{\mathrm{LM}}}; \quad r^* = \frac{r}{R_{\mathrm{max}}} \tag{7.6}$$

with t being the time, c the concentration and r the radius. The initial methane concentration is considered to be uniform; the initial temperature distribution was modeled using a symmetric parabolic function. Said function represents the initial temperature distribution of the bubble as it starts to travel through the liquid tin.

Referring to the initial conditions of the temperature distribution, the following considerations have been made and implemented. Since the bubble residence time inside of the liquid tin is in the range of a few seconds and because the gas phase temperature is crucial for methane conversion, the heat-up of the gas phase of the bubble while traveling through the liquid tin shall be represented in the model. Therefore, the innermost temperature $T_{\mathrm{B,0}}$ of the bubble was set to be equal to the gas temperature of the orifice outlet temperature $T_{\mathrm{G,out}}$, the calculation of which is explained in the previous section. The gas bubble temperature $T_{\mathrm{B,R}}$ at the outermost radius $r = R_{\mathrm{max}}$ of the bubble was set equal to the liquid tin temperature T_{LM}. The latter setting is based on a calcula-

tion of the Biot-number for a methane bubble in liquid tin which is equal or greater than 1000:

$$\mathrm{Bi} \geq \frac{2 \cdot \mathrm{r_B}}{\mathrm{d_B}} \frac{\lambda_\mathrm{L}}{\lambda_\mathrm{G}} \approx \frac{\lambda_\mathrm{Sn}}{\lambda_{\mathrm{CH_4}}} = 1000 \tag{7.7}$$

The above shown calculation of the Biot-number is further based on the assumption that there is no convection within the bubble and that the bubble rises in laminar conditions. The Nu-number of the tin- side of the bubble was calculated by the equation:

$$\mathrm{Nu} = 2 + 0.6 \cdot \mathrm{Pr}^{1/3} \cdot \mathrm{Re}^{1/2} \geq 2 \tag{7.8}$$

The initial temperature distribution of the bubble temperature between the center of the bubble and the outer boundary was modeled by a symmetric parabolic function, namely;

$$\theta = -(1 - T_{\mathrm{B},0}/T_{\mathrm{B,R}}) \cdot (1 - r^{*2}) \tag{7.9}$$

The above stated fundamental equations are defined as a one-dimensional problem, solving the temperature and concentration values for a given time and radius. The reaction enthalpy $\Delta \mathrm{H_R}$ was calculated by means of an energy balance according to

$$\Delta \mathrm{H_R} = \Delta \mathrm{H_R^0} + \int_{\mathrm{T_{298K}}}^{\mathrm{T_R}} (2\mathrm{c_{p,H_2}} + \mathrm{c_{p,C}} - \mathrm{c_{p,CH_4}}) \cdot \mathrm{X_{CH_4}} \mathrm{dT}, \tag{7.10}$$

wherein $\Delta \mathrm{H_R^0}$ is the standard reaction enthalpy, $X_{\mathrm{CH_4}}$ is the methane conversion and $c_{\mathrm{p,i}}$ is the specific heat capacity of the referenced species i. The gas pressure was

calculated on behalf of the hydrostatic pressure inside the liquid metal

$$p_{\mathrm{CH_4}} = p_\infty + \rho_{\mathrm{Sn}} \cdot g \cdot h_{\mathrm{Sn}} \tag{7.11}$$

where the density of liquid tin ρ_{Sn} is defined as [72]

$$\rho_{\mathrm{Sn}}(T) = 7374.7 - 0.6765 \cdot T \quad [\mathrm{T(K)}; \mathrm{kg/m^3}]. \tag{7.12}$$

The initial concentration $C_{\mathrm{CH_4}}$ inside the bubble is defined by the ideal gas law according to:

$$C_{\mathrm{CH_4}} = \frac{N_{\mathrm{CH_4}}}{V} = \frac{p}{\Re \cdot T} \tag{7.13}$$

After the calculation of the liquid metal section was completed, the remaining methane concentration in the gas was used as initial condition for the subsequent "Gas-phase" section inside of the reactor.

7.3 Gas phase

The gas phase is referring to a gas volume inside the liquid metal bubble column reactor, characterized in that the lower boundary of the gas volume is represented by the liquid metal surface area at nominal operation temperature and the upper boundary is defined by the inward facing surface of the reactor lid, which is kept at lower temperatures. The cylindrical wall of the gas section is heated on its outer surface and heats the gas phase

on the inside of the tube. As the pyrolysis gas passes through said gas section, it is exposed to different subsequent temperature zones. The thermo-chemical model was set up to calculate the total gas volume of the reactor as a plurality of vertically stacked volume slices through which the gas passes, wherein each volume slice is provided with an individual temperature value. This value is retrieved from an interpolation function which again is calculated from measured gas temperature values. The conversion within each volume slice was calculated using an ideal plug flow reactor at isothermal conditions. As a result of the above described considerations, the entire gas section was modeled by a plurality of isothermal plug flow reactors connected in series. Here, the conditions for the gas phase are substantially different compared to the previous section, the bubble column section. More specifically, the gas residence time is in the range of minutes and the gas is already at a high temperature. Therefore, the assumptions for calculating the methane decomposition are defined slightly different compared to the previous section. For a first order reaction kinetic $n = 1$, the methane conversion in the gas phase volume can be modeled by means of an ideal isothermal plug flow reactor with the performance equation:

$$k\tau = \int_{X_{\mathrm{CH_4,in}}}^{X_{\mathrm{CH_4,out}}} \frac{1+\epsilon X}{1-X} \mathrm{d}X \tag{7.14}$$

using the space time $\tau = \frac{V}{\dot{V}}$, the volumetric expansion factor ϵ and the kinetic rate constant k, according to the Arrhenius law

$$k = k_0 \cdot e^{\left(\frac{-E_a}{\Re \cdot T}\right)} \tag{7.15}$$

Considering the overall reaction of methane to hydrogen and carbon, the volume of the

gas increases as the decomposition proceeds. The increase in volume is taken into account by the fractional change in volume $\epsilon_{\mathrm{CH_4}}$

$$\epsilon_{\mathrm{CH_4}} = \frac{V_{X_{\mathrm{CH_4}}=1} - V_{X_{\mathrm{CH_4}}=0}}{V_{X_{\mathrm{CH_4}}=0}} \tag{7.16}$$

The methane conversion $X_{\mathrm{CH_4}}$ also considers the change of volume:

$$X_{\mathrm{CH_4}} = \frac{C_{\mathrm{CH_4},0} - C_{\mathrm{CH_4}}}{C_{\mathrm{CH_4},0} + \epsilon C_{\mathrm{CH_4}}} \tag{7.17}$$

In the case of thermal decomposition of methane, one mole of methane forms two moles of hydrogen; hence $\epsilon = 1$. The carbon volume fraction is neglected due to the high density of solid carbon compared to gaseous methane and hydrogen.

Chapter 8

Comparison of experimental and model results

► The objective of present chapter is to link the measured results of own conducted experiments with data that was obtained from the thermo-chemical model.

The experimentally measured methane conversion results have been presented within chapter 6, along with general information regarding the facility setup and reactor features. The fundamental equations, assumptions and further model parameters may be found in chapter 7. In this chapter, experimentally obtained processing data from liquid metal bubble column experiments of generation 2.1 are implemented into the thermo-chemical model and the methane conversion results are compared in a first step. In a second step, the same procedure is repeated for the additional gas-phase only experiments of generation 2.2.

As explained in previous chapter, the thermo-chemical model is composed of four sections, comprising different tools for calculating the gas flow phenomena, namely section I "Preheater" section II "Orifice", section III "Liquid Metal" and section IV "Gas Phase". All calculations have been carried out on behalf of several input parameters, taken from the experimental data set. For the calculation of section I, the input data included the methane feed flow rate $\mathrm{F}_{2.2}$, outlet temperature $\mathrm{T}_{1.1}$ and the gas pressure $p_{1.1}$. The calculating section II was achieved by including the two temperature parameters T_{W} and $T_{\mathrm{G,in}}$ to the model. Section III was calculated by inserting the measured wall temperatures $\mathrm{T}_{4.1}$, $\mathrm{T}_{4.2}$ and the reactor filling height L_{LM}. The bubble residence time within the reactor was considered to be constant for all applied flow rates, see experimental results of chapter 5. Section IV was calculated on behalf of the applied methane feed flow rate $\mathrm{F}_{2.2}$ and on behalf of a temperature function fitted to the reactor inner temperature measurements.

For experiments conducted at a nominal wall temperature of 900 °C and a liquid metal filling height of 600 mm, a third gas phase temperature was retrieved from the thermo-couple $\mathrm{T}_{1.3}$. Based on said temperature measurements, the blank tube section of the reactor was separated into two (for 750 °C and 850 °C) or three (for 900 °C) zones in such way that the inlet and outlet of each zone is located at a thermo-couple inside of the reactor. The temperature distribution inside each zone was modeled by a linear function. With respect to the dependency of the found reactor temperatures from the applied flow rates, a total of 42 temperature functions were defined. Said functions are represented by the linear curves in fig. 8.1. In the thermo-chemical model, the temperature gradient within the gas phase was modeled by a series of ideal isothermal PFRs with an incremental length of 1 mm. The top figure of fig. 8.1 depicts the drop in gas temperature for all applied flow rates, referring to normalized conditions. At a distance of 95 mm

from the liquid metal surface an increase in the flow rate by 50 mln/min resulted in an temperature drop of about 30 °C. The lower the flow rate, the less heat is transported to the upper region of the reactor. As shown in the middle figure of fig. 8.1, lower flow rates result in lower gas phase temperatures, yet with a smaller temperature gap compared to the runs at 750 °C. The reduction of the liquid metal filling height by 40% exposes thermocouple $\mathrm{T}_{1.3}$ to the gas phase, defining the intersection between zone 1 and zone 2, as shown in the lower figure of fig. 8.1. Corresponding to the findings of runs at higher filling heights, the temperature decreases for decreasing flow rates. Here, zone 3 is of the same length as zone 2 for runs at 1000 mm filling height.

Further information helps understanding fig. 8.1: It is shown the change in gas temperature for different flow rates for runs at liquid tin temperatures of 750 °C (top figure) and of 850 °C (middle figure) at about 1000 mm filling height. For runs at 750 °C and 850 °C, the gas section of the reactor tube is separated into two zones, whereas zone 1 represents the space in between the liquid metal surface at $L = 0$ mm and the thermocouple $\mathrm{T}_{1.4}$ at $L = 20$ mm, and zone 2 is fitted in between the thermocouples $\mathrm{T}_{1.4}$ at $L = 20$ mm and $\mathrm{T}_{1.5}$ at $L = 95$ mm. For runs at liquid tin temperatures of 900 °C and about 600 mm filling height, the gas section of the reactor tube is separated into three zones. Here, zone 1 is fitted in between the liquid metal surface at $L = 0$ and the thermocouple $\mathrm{T}_{1.3}$ at $L = 220$ mm, zone 2 is fitted in between the thermocouples $\mathrm{T}_{1.3}$ at $L = 220$ mm and $\mathrm{T}_{1.4}$ at $L = 400$ mm and zone 3 is fitted in between the thermocouples $\mathrm{T}_{1.4}$ and $\mathrm{T}_{1.5}$. For the location of the thermocouples, see also fig. 6.8.

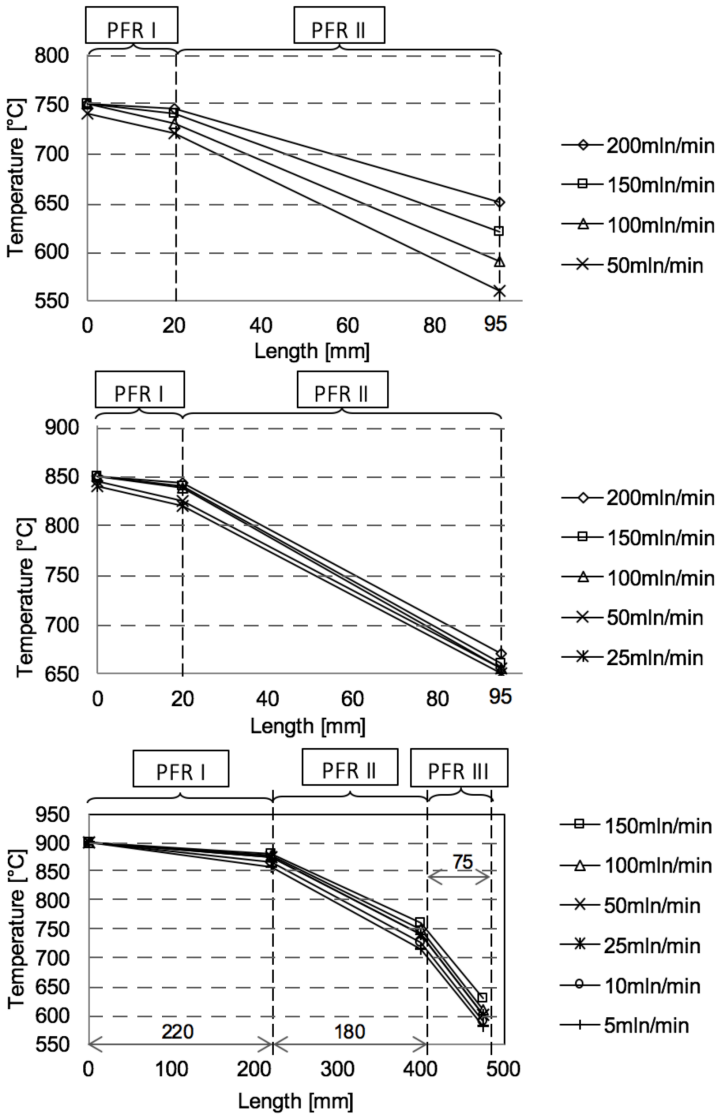

Figure 8.1: Temperature distribution functions in the gas phase above the liquid metal as implemented into the model.

8.1 Modeling results for the conversion in the bubble column experiments of generation 2.1

Modeling the whole reactor was realized by connecting the four individual reactor sections in one calculation script using Matlab. For each data point, consisting of a tem-

perature and a flow rate value and its corresponding temperature functions, different sets of pre-exponential factors and activation energies obtained from the literature have been assigned to the calculation. For further information regarding the utilized kinetic parameters, please refer to chapter 2. Applying the kinetic data shows that kinetic parameters provided by Kevorkian et al. [37] and Kozlov et al. [40] yield a much lower methane conversion compared to kinetic parameters provided by Rodat et al. [24] and Kassel et al. [35], whereas Kevorkian et al. [37] always delivers slightly higher conversions compared to Kozlov et al. [40]. Parameters taken from Rodat et al. [24] yield the highest conversion, except for runs at 750 °C, where Kassel et al. [35] yield the highest conversion. Comparing the results of the thermo-chemical model to their experimental counterparts, for each nominal temperature level, different characteristics are observed. At 750 °C, the only existing experimental conversion result other than zero was found at a flow rate of 50 mln/min, showing a methane conversion of 0.018%. At this flow rate, the highest conversion result gained from the model is about half of the measured value in the case of kinetic parameters taken from Kassel et al. [35] Other kinetic parameters yield even lower values.

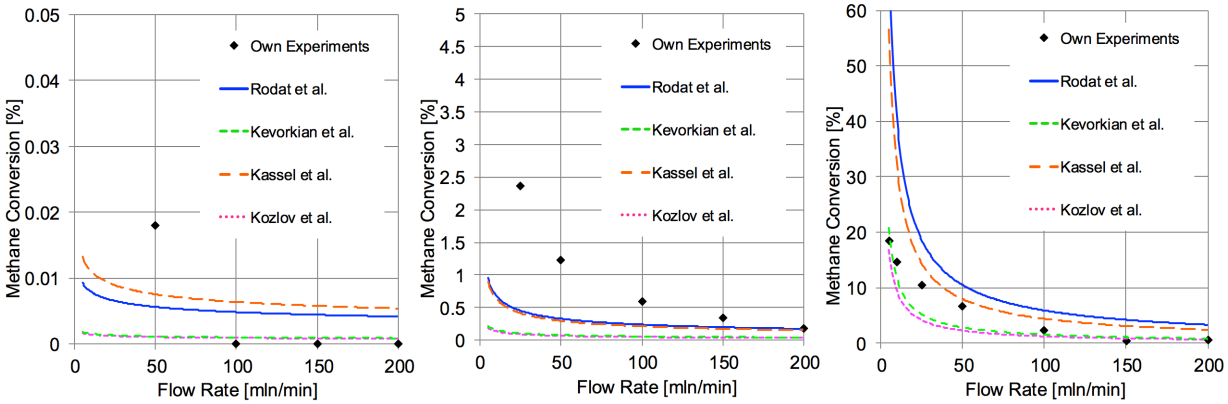

Figure 8.2: Comparison of experimental and calculated methane conversion for runs with liquid metal in relation of the flow rate at nominal operation temperatures of 750 °C (left), 850 °C (middle) and 900 °C (right)

At a nominal temperature of 850 °C, the model again indicates lower conversion rates, compared to the experimental values. However, the results are again in the same order of magnitude as the measured values, as shown in the middle figure of fig. 8.2. A possible reason for the underestimation of the model is the linear approximation in between the measured temperatures. According to the lower figure of fig. 8.1, due to the additional temperature measurement in case of the lower filling height, the axial temperature distribution model shows a more convex shaped contour, hence higher mean temperatures compared to a linear approximation. For the case of runs at 900 °C at a filling height of 600 mm, comparing the results gained from the thermo-chemical model to the measured data, it can be observed that the measured conversion is lower than conversion calculations using kinetic data from Rodat et al. [24] and Kassel et al. [35], whereas Kevorkian et al [37]. and Kozlov et al. [40] predict lower conversion. Towards low flow rates, the values of the model are higher than the obtained experimental results, see fig. 8.2. As a conclusion, even though the observed model predictions are not in perfect agreement with the measured data, at 750 °C and 850 °C measured and modeled methane conversions were found to be in the same order of magnitude. At 900 °C, at low flow rates of 5 - 10 mln/min and 100 - 200 mln/min, the kinetic parameters suggested by Kozlov et al. [40] and Kevorkian et al. [37] provide a good conversion prediction, whereas for flow rates in the range of 25 - 50 mln/min, parameters suggested by Kassel et al. [35] provide the best agreement, see fig. 8.2. Applying kinetic data taken from Shantarovic et al. [39], Palmer et al. [41] et al., Chen et al. [34] and Skinner et al. [36], the predictions were even below those of Kozlov et al. [40] and Kevorkian et al. [37]; kinetic data provided by Steinberg et al. [38] was exceeding the conversion prediction by Rodat et al. [24] and Kassel et al. [35] by far. For the sake of improved clarity, modeling results using kinetic parameters taken from said authors are not represented in the plots.

8.2 Modeling results for the conversion in the liquid metal section only

As shown, the gas heat-up in the orifice is depending on the feed flow rate. In the cases of a liquid metal temperature and wall temperature of 900 °C, feed flow rates of 5 and 10 mln/min already resulted in a gas heat-up to 900 °C. In all other cases, the gas was not entirely heated up by the wall structure before the bubble detached from the orifice. The calculated gas temperatures for each calculated configuration are shown in fig 8.3. Further, according to the calculation, the gas bubble temperature in all calculated cases reached the surrounding liquid temperature at the time the bubble was exiting the liquid metal. Therefore, the bubble heat-up was fully completed during the rise of the bubble inside of the liquid metal inventory.

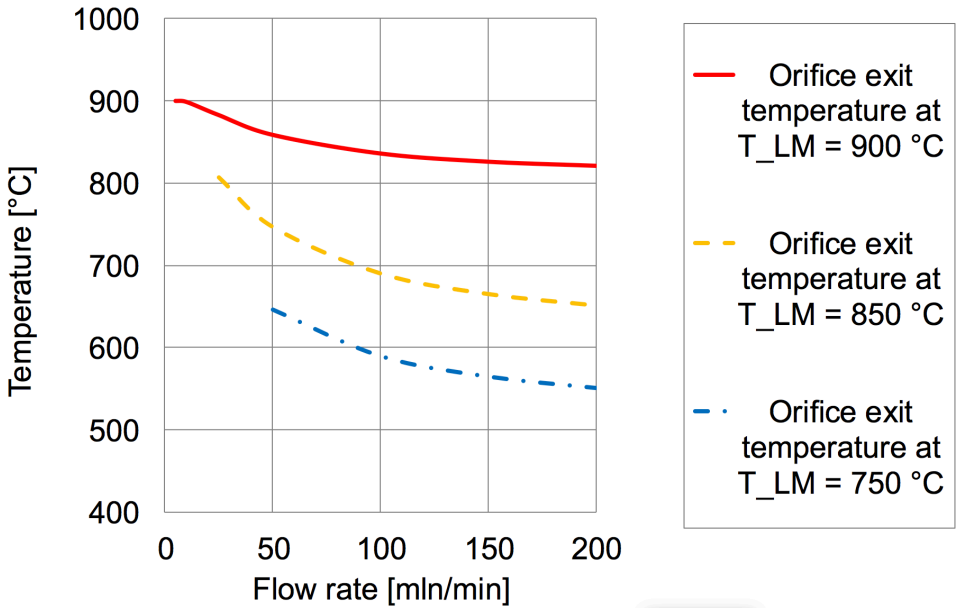

Figure 8.3: Model-calculated orifice outlet temperatures of the gas at different operation temperatures

Taking a look at the conversion results shown by the calculation, two important details

surface. Firstly, conversion results are independent from the feed flow rate which is related to the modeling assumption taken from chapter 5, claiming that bubble rise and bubble size characteristics may be assumed independent from the applied feed flow rate. However, the before-mentioned variation in gas temperature for different flow rates apparently had also no impact on the conversion rate. This may be related to the another aspect, namely the extremely low conversion rate. As shown in fig. 8.4, the methane conversion right at the exit of the liquid metal section was in the range of $7.68 \cdot 10^{-6}$ mole-% (Kozlov et al. [40]) to $5.38 \cdot 10^{-5}$ mole-% (Kassel et al. [35]) in the case of 750 °C, $4.18 \cdot 10^{-4}$ mole-% (Kozlov et al. [40]) to $2.03 \cdot 10^{-3}$ mole-% (Rodat et al. [24]) in the case of 850 °C and $1.42 \cdot 10^{-3}$ mole-% (Kozlov et al. [40]) to $6.58 \cdot 10^{-3}$ mole-% (Rodat et al. [24]) in the case of 900 °C. It is likely that the feed flow rate-induced temperature difference of the gas bubbles at a given liquid metal temperature had such a small impact on the already low conversion, such that it was not represented in the calculated values. The shown results indicate that 1) liquid metal provides an efficient heat-up of the gas bubbles and 2) since the overall results of the calculation are in fact in the same order of magnitude with the measured results, the gas residence time of a few seconds in the liquid metal phase is not sufficient for a considerable amount of methane conversion; hence it must be increased substantially.

In order to independently verify the calculation model for the plug-flow section, isolated gas-phase experiments had been conducted which will be the subject of the subsequent section.

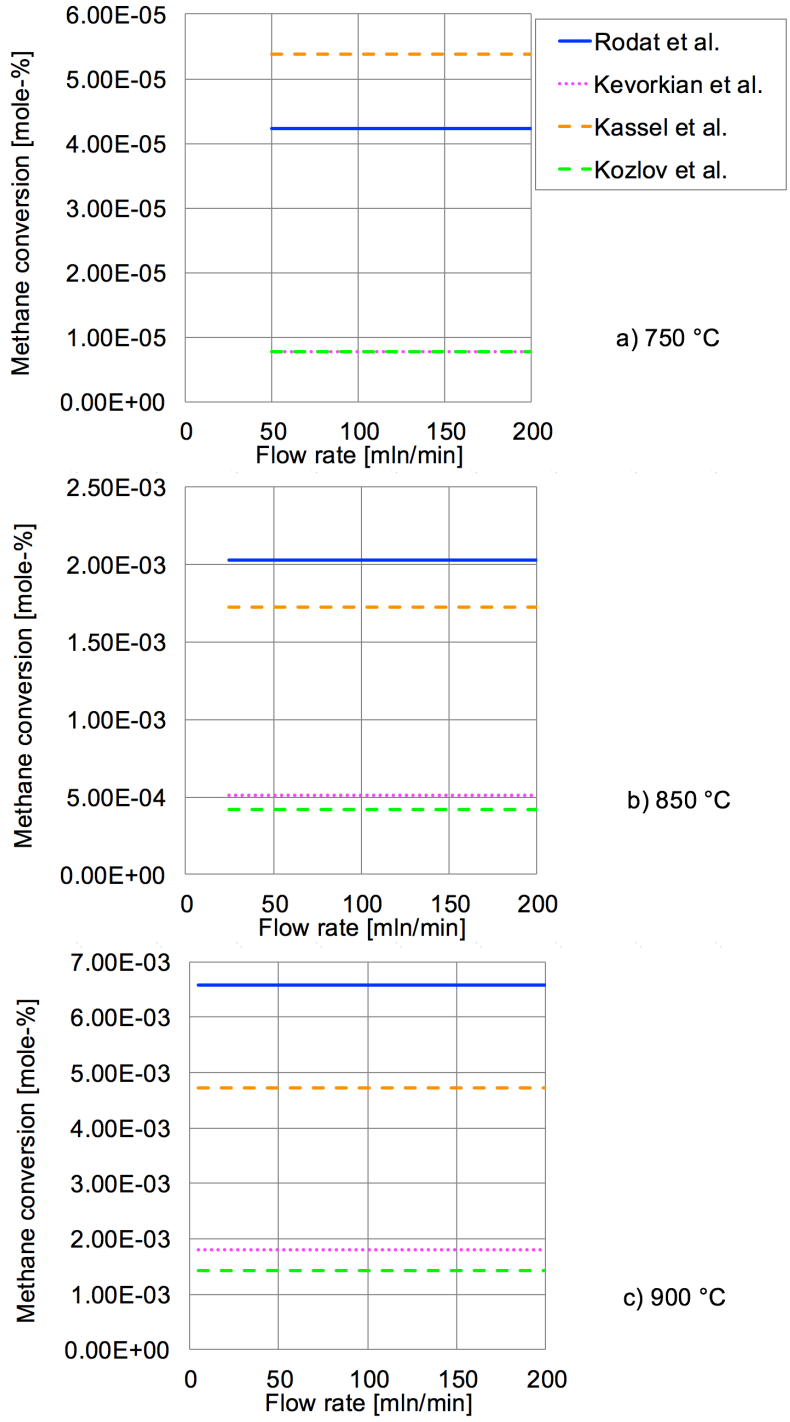

Figure 8.4: Modeling results for the conversion of the liquid metal section alone at a) 750 °C, b) 850 °C and c) 900 °C

8.3 Modeling results for the conversion in the empty-tube experiments of generation 2.2

Modeling of the blank tube experiments was conducted similarly to the previously introduced model as shown in chapter 7, only without the liquid metal section. Again, the reactor tube was modeled by a series of ideal isothermal PFR reactors with an incremental length of 1 mm, using a first order reaction kinetic, as explained in chapter 7. Since the reactor surface was temperature controlled, the temperature profile of the reactor is independent from the methane feed flow rate. Further, kinetic data has been applied to the thermo-chemical model in accordance with the scheme used for the experiments in liquid metal documented in previous section.

The temperature distribution along the vertical axis of the reactor for each of the three previously mentioned temperature levels is depicted in fig. 8.5, comprising all temperature parameters that have been measured by the thermocouples of the reactor. Multiple temperature data points at a given x-axis position for one temperature level correspond to the plurality of thermo couples that are applied to the azimuthal cross-sections B and C. Fig. 8.5 also shows third-order polynomial fit parameters for each nominal temperature level. Having said plurality of temperature values provides the opportunity of applying the polynomial data fit. The yielded polynomial fit was later implemented in the thermo-chemical model, which is discussed in detail within the subsequent chapters of this thesis, see chapters 7 and 8.

In the case of 750 °C and 850 °C experiments, kinetic parameters taken from Rodat et al. [24] and Kassel et al. [35] show a good agreement for the entire range of applied flow rates, see fig. 8.6. The slope of the experimental data points and the thermo-chemical

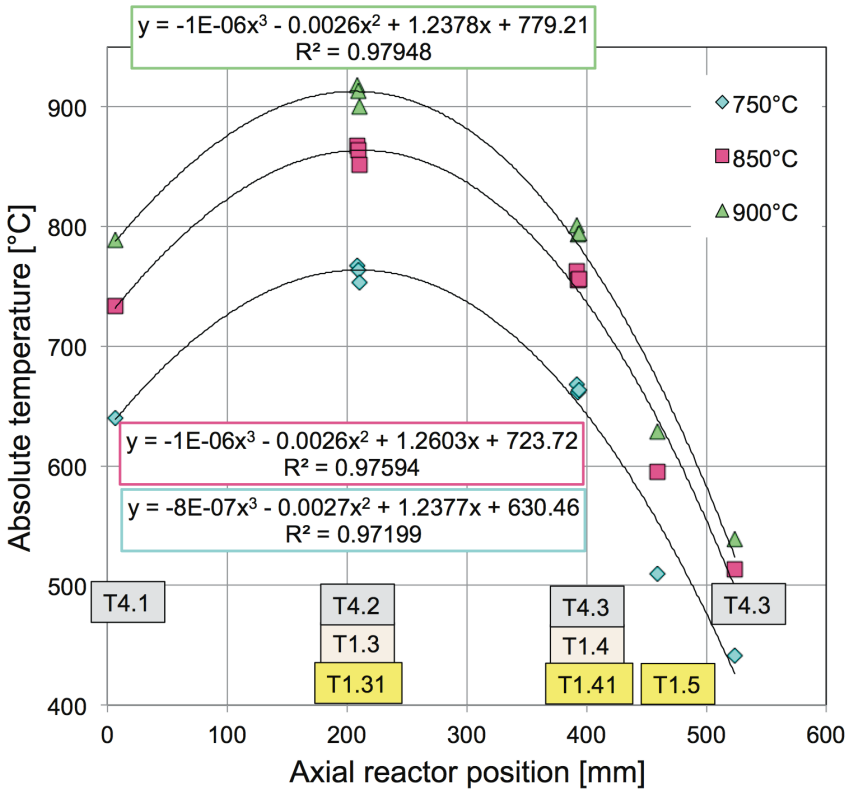

Figure 8.5: Axial temperature distribution for the blank tube experiments. For each nominal temperature level, the fit parameters are shown

model show an almost identical characteristic for all flow rates. Similar tendencies can be observed for experiments at 900 °C for flow rates greater than 50 mln/min. At lower flow rates, the model predicts higher values than measured. Contrary to the observation at lower temperatures, the slopes of the model prediction curves are not matched by experimental data. This observed deviation appears to be a systematic error that is most likely related to the model limitations. Since all models used are referring to a single first order reaction that is not inhibited by hydrogen, it seems possible that a hydrogen inhibition might have occurred towards higher temperatures, as proposed by Kassel et al. [35]. On the other hand, Rodat et al. [24] observed higher hydrogen yields in experiments compared to the accompanied modeling results, even though hydrogen inhibition was not considered kinetically. As a conclusion, the used kinetic parameters

were not sufficient for explaining the experimental results. Further it is assumed that a more sophisticated model comprising a stepwise decomposition and reverse reactions might lead to an improved data fit. Blank tube experiments indicate that conversion val-

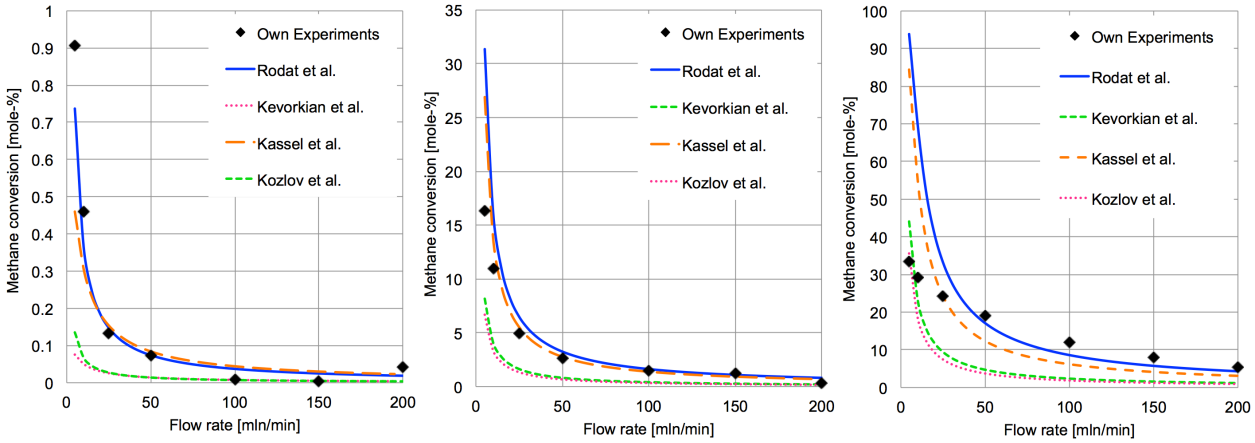

Figure 8.6: Comparison of experimental and calculated methane conversion for runs with an empty-tube reactor in relation of the flow rate at nominal operation temperatures of 750 °C (left), 800 °C (middle) and 900 °C (right)

ues gained from a calculation with kinetic data of Rodat et al. [24] result in an optimistic conversion ratio which represents the upper limit of the observed conversion rate. For small flow rates and runs with 900 °C, the slope of the thermo-chemical model is not justified by experimental findings.

However, the experiments and the models consistently show that for runs with liquid metal, methane conversion increases for a reduced liquid metal inventory- which is related to the much higher residence time of the gas inside a blank tube compared to the residence time of a bubble rising in a liquid bath of the same volume. This indication however is contrary to the findings of Serban et al. [5], who states that the methane conversion of a blank volume is less than the same volume being partially filled with liquid metal. According to Serban et al. [5], the loss of gas residence time inside the reactor caused by the presence of liquid tin was not only compensated, but even surpassed by

presumed catalytic effects of liquid tin on the methane conversion rate. Fig. 8.7 provides an overview of all experimental and calculated results.

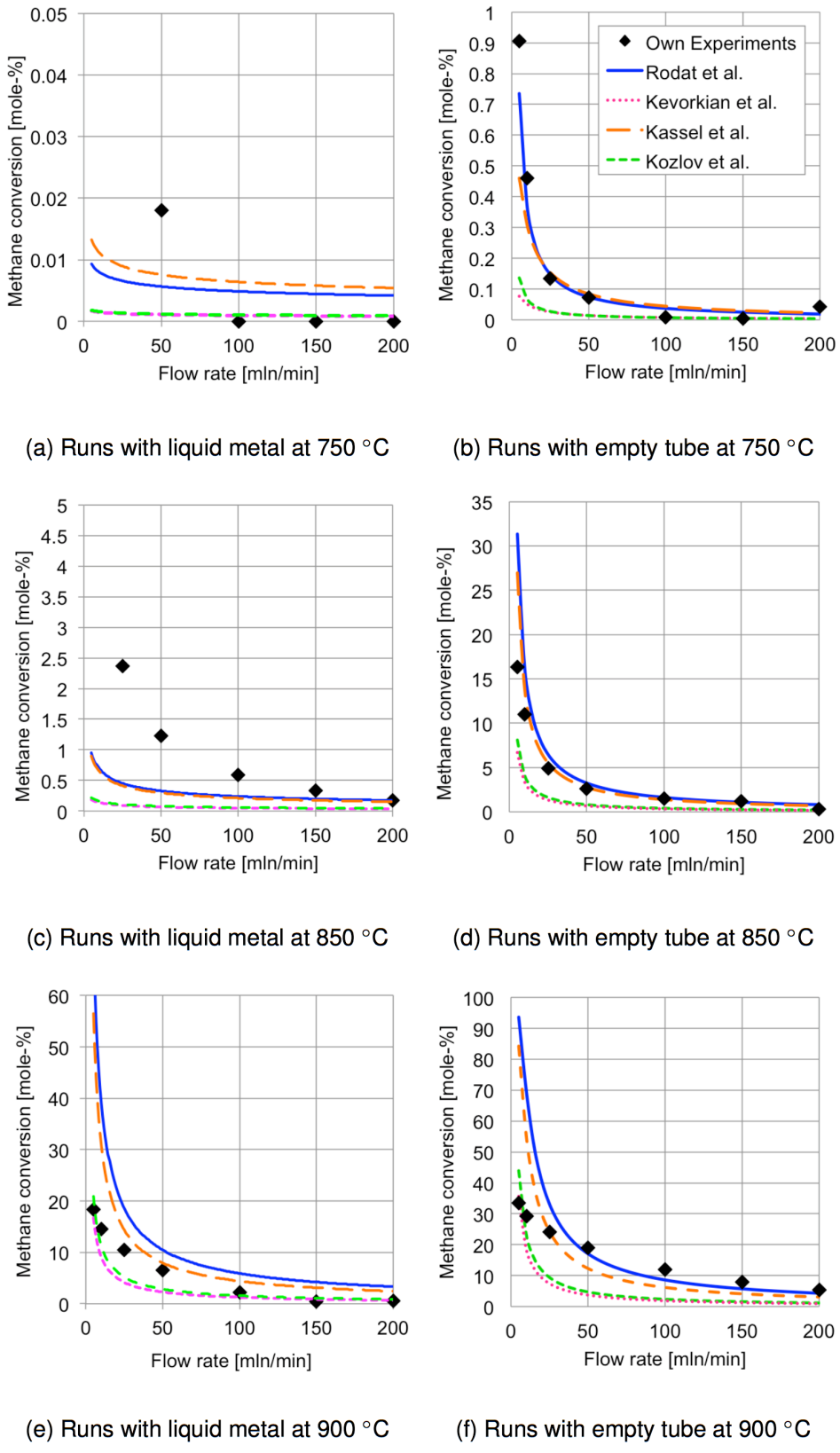

(a) Runs with liquid metal at 750 °C

(b) Runs with empty tube at 750 °C

(c) Runs with liquid metal at 850 °C

(d) Runs with empty tube at 850 °C

(e) Runs with liquid metal at 900 °C

(f) Runs with empty tube at 900 °C

Figure 8.7: Overview of all the experimental and calculated methane conversion results sorted by reactor type (left row: bubble column, right row: empty-tube) and temperature levels.

Chapter 9

Discussion of Serban's results

► Within this chapter, the previously developed and utilized thermo-chemical models for modeling the TDM reaction in own bubble column and empty-tube reactor experiments will now be applied to the reactor setup that was used by Serban et al. [5] after a detailed analysis of a selection of Serban's experimental results.

For the sake of comparing own experiments to Serban's reactor experiments, an analysis of experimental data provided by Serban will be presented in the following. Unfortunately, no detailed process data regarding Serban's reactor experiments is available, particularly with respect to temperature distributions on the inside of the reactor. Also, gas pressure values are not available. Therefore, in the following assessment, ideal conditions are assumed, namely an isothermal reactor at 750 °C, operated at ambient pressure. This assumption leads to an optimistic methane conversion calculation,

since usually the nominal reaction temperature is reached only in a fraction of the entire reactor. However, the presented case therefore is partly speculative and shall not be interpreted as critique of the work conducted by Serban. Rather, it shall provide a comparative analysis, on which ground future experiments may be conducted and put into relation with the findings of Serban. Relevant background information and particularly the selection of experiments relevant for this study had been introduced in chapter 4. With reference to the background of this work and the stated hypotheses therein, three experimental campaigns conducted by Serban are significant for this thesis. In particular, the considered experiments cover runs with liquid tin in a two-phase reactor setup (no solids in the liquid phase) and comparative runs without liquid tin. Further experiments covering liquid lead and packed-bed reactor setups have not been considered in this work.

9.1 Reactor dimensions

The reactor utilized by Serban was of a cylindrical shape with an inner diameter of 25.4 mm and an inner total length of 355 mm. A gas feed tube was mounted on the inside of the reactor to the reactor ceiling, extending almost the entire length of the inner height along the center axis. Optionally, for runs comprising liquid tin as heat transfer fluid, the reactor was partly filled with liquid tin, providing a liquid tin filling height of about 100 mm, measured from the reactor-inner bottom. The dimensions are shown in fig. 9.1. From a modeling perspective, it is important to correctly represent all the individual reaction zones inside of the reactor that are acting as separated reactor sections. In the case of Serban's reactor, it is therefore necessary to differentiate between blank runs, runs with liquid metal and to further distinguish between two different utilized feed

tubes.

As outlined before, the pyrolysis gas enters the reactor from the top and flows to the reactor bottom through the reactor-inner feed pipe. During this time, methane conversion may already occur. Here, the feed pipe acts as a plug-flow reactor at a constant temperature, equal to the reactor operation temperature. This first volume is in the following referred to as "PFR I" -section. Subsequently, after exiting the feed tube, the pyrolysis gas travels through a 100 mm deep liquid metal bath, the "liquid metal" or "LM" -section for all runs with liquid metal. After this section, the pyrolysis gas enters the empty-tube section above the liquid metal surface; the "PFR II" -section. The latter section again constitutes a plug-flow reactor comprising a cross-section that equals to the reactor-inner cross-section less the outermost cross-section of the gas feed tube and a length that is the total inner height of the reactor less the liquid metal filling height. Alternatively, for runs without liquid metal, the pyrolysis gas is led directly into the main reactor, which again embodies a plug-flow reactor comprising a cross-section as explained before and a length that is the total inner height of the reactor. This volume is in any case referred to as "PFR II" -section in the following. Therefore, in the case of liquid metal being present within the tube reactor, the pyrolysis gas is exposed to a plug-flow reactor "PFR II" -section again after exiting the liquid metal section, similar to the modeling concept of own experiments.

Due to Serban's small reactor inner diameter, the presence of the feed tube has a significant impact on the inner volume and thus the total and sectional gas residence time. During the herewithin discussed experimental campaign, Serban investigated the impact of a change in bubble size on methane conversion by utilizing two different open bore feed tubes. The bigger tube, named feed tube 1, comprises an inner diameter of 5.33 mm and an outer diameter of 6.35 mm, whereas the smaller feed tube, named

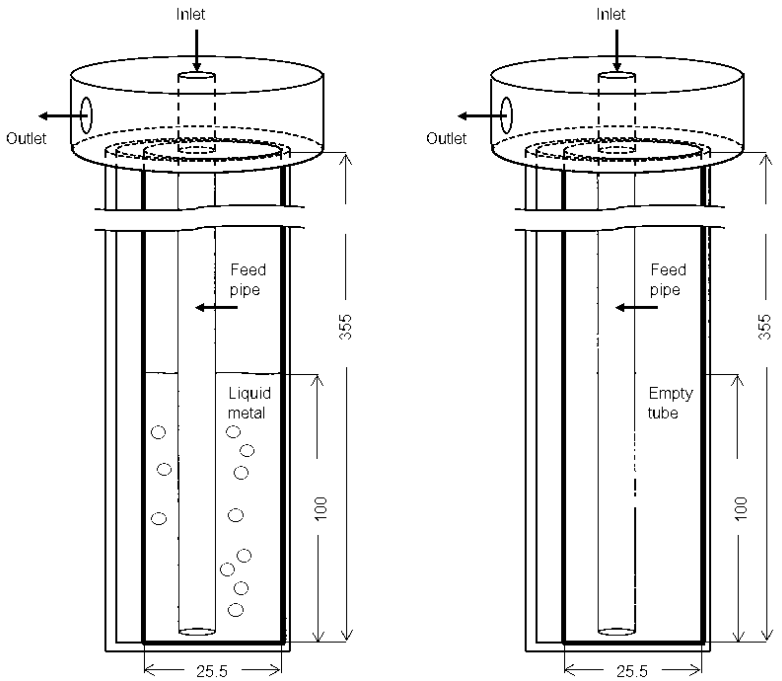

Figure 9.1: Schematic illustration and dimensions of Serban's reactor presented in $[\mathrm{mm}]$-units. [5]

tube 2, has an inner diameter of 0.51 mm and an outer diameter of 1.6 mm.

Runs in the presence of liquid tin using the bigger feed tube as gas injection device have been implemented into the thermo-chemical model as follows. The first plug-flow reactor section is defined by the inner volume of the bigger feed tube $V_{\mathrm{PFR\,I\,tube\,1,\,I.D.}}$ = 7.9 ml. The smaller feed tube yields a much smaller inner volume of the first plug-flow section, namely $V_{\mathrm{PFR\,I\,tube\,2\,I.D.}}$ = 0.073 ml. Regardless of whether liquid metal is present, the feed tubes always are assumed to be filled with gas along the entire length of the tube. For the PFR II -section, the outer diameter of the feed tubes has some impact on the net volume provided for the gas. According to the latter, the PFR II -section above the liquid metal surface for runs with liquid metal has the volume

$$V_{\mathrm{PFR\,II,\,tube\,1}} = V_{\mathrm{Reactor}} - V_{\mathrm{LM}} - V_{\mathrm{tube\,1,\,O.D.,\,PFR\,II}} = 121.1\ \mathrm{ml}, \tag{9.1}$$

with $V_{\text{tube 1, O.D., PFR II}}$ being the volume covered by the bigger feed tube along the vertical length of the plug-flow section. Corresponding to the smaller outer diameter of the smaller feed tube, the volume of the plug-flow section using the smaller feed tube yields in a slightly increased net volume:

$$V_{\text{PFR II, tube 2}} = V_{\text{Reactor}} - V_{\text{LM}} - V_{\text{tube 2, O.D., PFR II}} = 128.7\,\text{ml}. \tag{9.2}$$

Accordingly, the net volume of the plug-flow section for runs with a blank tube also shows a slightly higher volume, if the smaller tube 2 is mounted inside of the reactor:

$$V_{\text{PFR II, tube 1}} = V_{\text{Reactor}} - V_{\text{tube 1, O.D}} = 168.7\,\text{ml}, \tag{9.3}$$

$$V_{\text{PFR II, tube 2}} = V_{\text{Reactor}} - V_{\text{tube 2, O.D}} = 179.2\,\text{ml}, \tag{9.4}$$

9.2 Gas residence time

Upon the above stated equations, it is shown that the optionally two or three consecutive reactor zones all comprise different reactor volumes, depending on the used reactor setup. The gas residence time τ is depending on both the reactor volume V_{Reactor} and the applied volumetric flow rate $\dot{V}_{\text{Feed}}$

$$\tau = V_{\text{Reactor}}/\dot{V}_{\text{Feed}} \tag{9.5}$$

for all the PFR -sections. The gas residence time inside of the liquid metal section solely depends on the gas bubble rise velocity, which was found to be at least 0.2 m/s or higher and to be rather independent from the applied flow rate; see also chapter 5 for more information.

In order to depict the above discussed sections in terms of their impact on the gas residence time, fig. 9.2 illustrates the actual gas residence time for all the different reactor setups used by Serban and discussed herewithin. The depicted case represents a feed flow rate of 9 mln/min, which was also subject of all considered experiments conducted by Serban. For simplification purposes, it was assumed an isothermal reactor at 750 °C operated at ambient pressure.

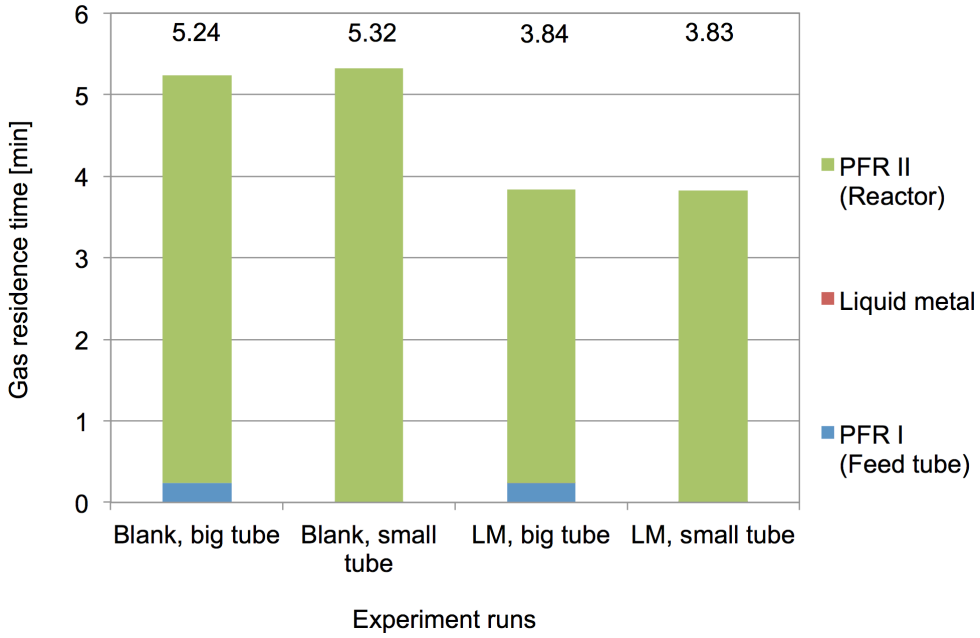

Figure 9.2: Calculated gas residence times for different reactor setups at an exemplary gas feed flow rate of 9 mln/min, assuming isothermal reactor conditions at ambient pressure. The gas residence time within the liquid metal (red bullet) is positioned between the blue bar (Feed tube) and the green bar (Reactor), but is too small to be applicable in the comparison shown above.

Here, the four different reactor setups, differentiating between the used feed tube (big or

small) and whether liquid metal (LM) or an empty tube (Blank tube) were utilized. The blue bars refer to the feed tube section, named PFR I, the red bars refer to the liquid metal section (LM) and the green bars refer to the gas section inside the reactor above the liquid metal surface, named PFR II.

Several aspects may be learned from fig. 9.2. First, the majority of gas residence time has to be accounted to the PFR II section, wherein only the big tube contributes to the total residence time with a considerable share. Even though the small feed tube yields a negligible gas residence time, the total gas residence time is higher, due to the smaller volumetric displacement of the smaller tube. Furthermore, it is shown that the liquid metal section also accounts to a negligible fraction of the gas residence time. Here, the gas bubble rise velocity was assumed to be 20 cm/s, but even if the gas bubble rise velocity was only half of this value, it would still be equal to 1s, considering the 10 cm height of the liquid metal inventory. As a matter of fact, a reduction of gas bubble rise velocity is always correlated with an increased gas hold-up of the liquid metal inventory, hence the surface level rises accordingly. Therefore, for the considered setups, the total gas residence time can at no operation condition be higher than the depicted value for the referred gas conditions. The sheer presence of liquid tin cancels about 30% of gas volume out of the reactor. As a consequence, if methane conversion is observed to be increased for runs with liquid metal compared to runs without liquid metal, the sole presence of liquid metal must trigger a conversion increase equal or larger to an increase of gas residence time by 30%.

Fig. 9.3 depicts the methane conversion measured by Serban for the above introduced reference experiments conducted at 750 °C at a flow rate of 9 mln/min. Here, the previously addressed problem becomes evident. Comparing runs with and without liquid metal separately, it is shown in both cases that a slightly increased total residence time

increases methane conversion. However, when comparing all runs with each other it is striking that even though about 30% of the total gas residence time for runs with liquid metal is lost, the conversion ratios during runs with liquid metal yield much higher conversion ratios compared to runs with an entirely empty reactor. The only explanation for this observation according to Serban et al. [5] may be a strong catalytic activity of liquid tin on the methane conversion.

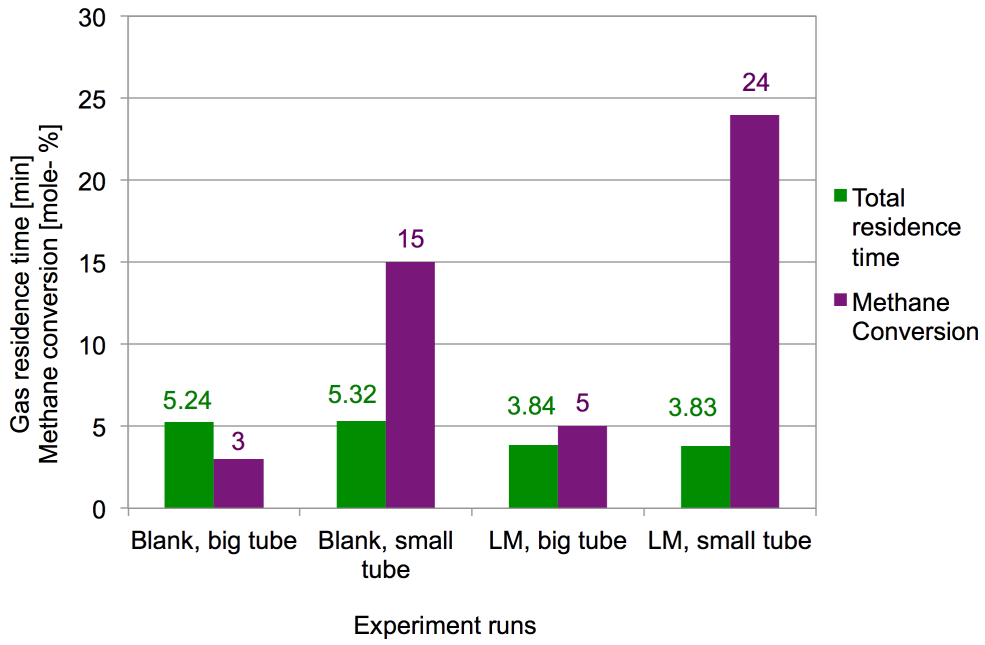

Figure 9.3: Calculated gas residence times for different reactor setups at an exemplary gas feed flow rate of 9 mln/min, assuming isothermal reactor conditions at ambient pressure.

The problem yet to be solved was to test, whether the models which have been developed for the herewithin documented experimental runs, are applicable to the experiments of Serban and will be in line with Serban's experimental findings. In principle, at least the empty-tube runs should lead to similar agreements as observed during own experiments[1].

[1] Methane conversion was calculated by Serban referring to the gas fraction only, using the same model as applied to own "empty-tube" experiments.

9.3 Modeling Serban's reactor

The thermo-chemical model was achieved in a similar fashion as the thermo-chemical model used for own experiments. As outlined above, the entire reactor was considered to be an isothermal reactor, comprising a first PFR I -section, defined by the feed tube and a subsequent PFR II -section, which is defined by the reactor volume. Optionally, a liquid metal, LM -section, is stacked in between the first and the second PFR -sections. Since the reactor is considered isothermal, modeling the PFR -sections is rather straightforward without the need for implementing a temperature-function. The liquid metal section was also modeled as outlined in chapter 7 and according to fig. 9.4.

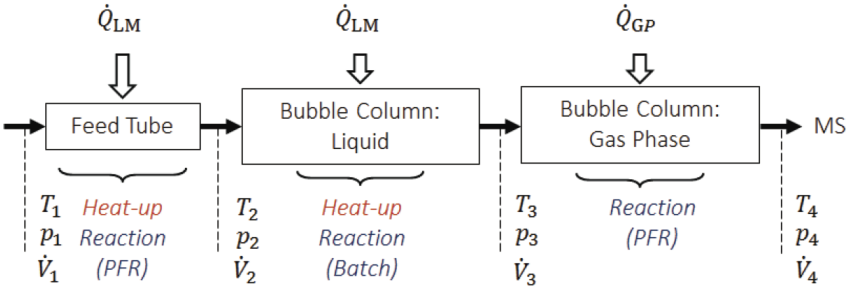

Figure 9.4: Schematic illustration of the thermo-chemical model used for Serban's reactor.

Again, the same four kinetic data sets from the previously introduced references had been utilized in the model. The results gained from the thermo-chemical model are shown below in relation with the conversion data as presented by Serban et al. [5]. Here, fig. 9.5 comprises runs with a blank tube reactor, whereas runs with the large tube are shown on the left and runs with the small tube are shown on the right. Correspondingly, fig. 9.6 illustrates the results and measured conversion data for runs with liquid metal; again showing experiments using the big tube on the left side and experiments using the small tube on the right side of the figure.

In general, a strikingly large deviation in between measured results and the results

gained from the thermo-chemical model may be observed. In fact, due to this huge difference, methane conversion was referenced using a logarithmic scale. Similar to own results, kinetic data of Rodat et al. as well as Kassel et al. indicate a higher conversion compared to the results obtained with kinetic data taken from Kevorkian et al. and Kozlov et al. However, due to this inevitable gap, an analysis of tendencies appears plainly unreasonable in this matter. The only conclusion that might be drawn from the depicted illustrations is that for runs with a blank tube, thermo-chemical results are outperformed by Serban's measurements by the order of two, whereas experimental results related to runs in liquid metal outperform thermo-chemical model results by three orders of magnitude. As a conclusion, it is not apparent, what circumstances are responsible for the observed deficiencies of own results in view of Serban's results.

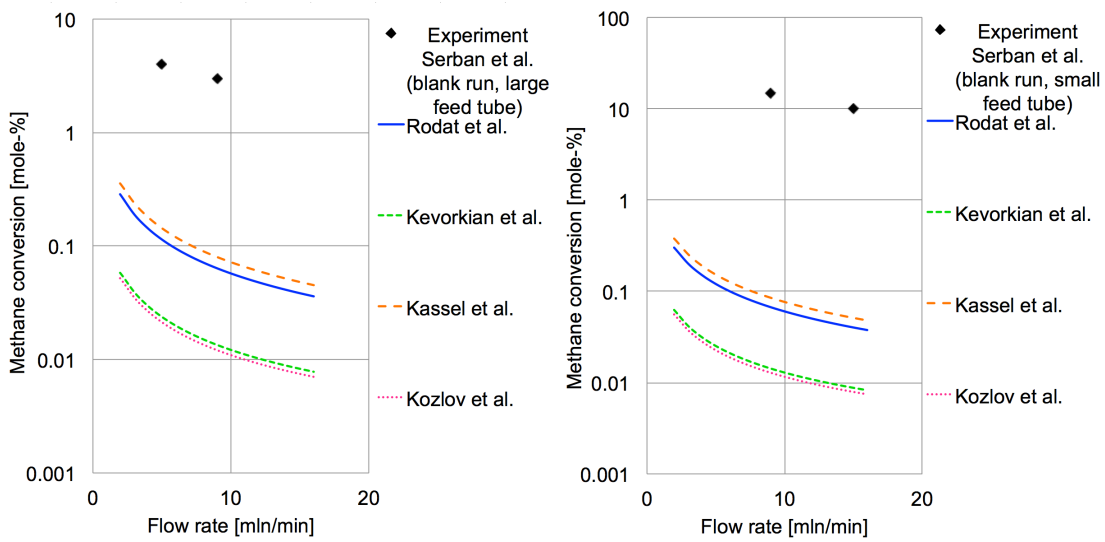

Figure 9.5: Conversion prediction results of the thermo-chemical model and measured methane conversion data provided by Serban. Experiments show blank-runs using tube 1 (left) and tube 2 (right) at an operation temperature of 750 °C

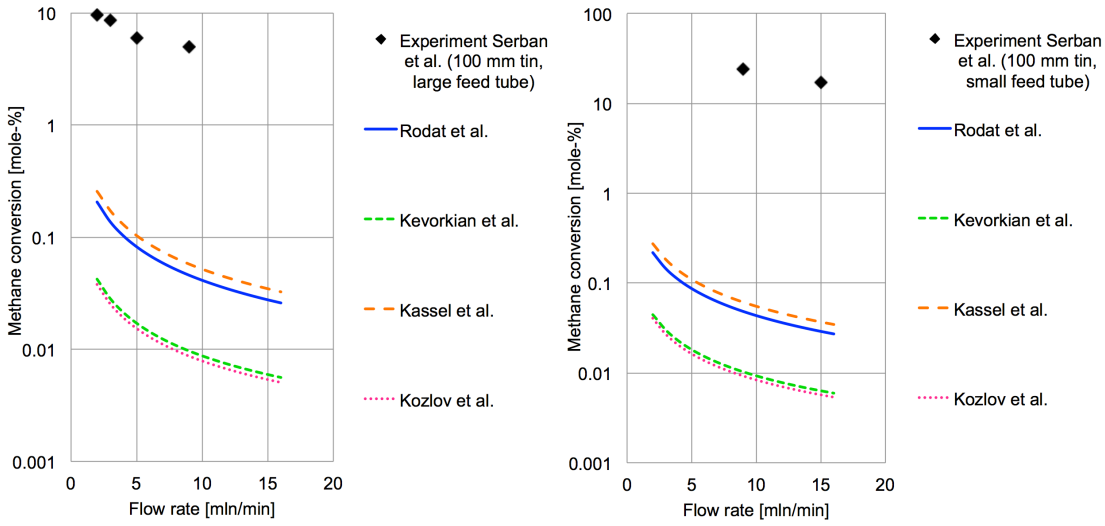

Figure 9.6: Conversion prediction results of the thermo-chemical model and measured methane conversion data provided by Serban. Experiments show runs with liquid metal using tube 1 (left) and tube 2 (right) at an operation temperature of 750 °C

Chapter 10

Experimental results in the context of the basic hypotheses

► The subject-matter of the following chapter covers the interpretation of previously presented results in light of the basic hypotheses stated earlier in chapter 4. In the end of this chapter, a new, improved hypothesis is claimed.

One core element of this thesis is to investigate the applicability of Serban's work as a tool for developing a process for thermal decomposition of methane. In this respect, it was chosen to apply falsification means to a study provided by Serban et al. [5], which was identified as the closest and most advanced research document available during the development of this thesis.

The in-depth review of cited study resulted in one main hypothesis, stating that liquid tin

must have a catalytic impact on the thermal decomposition reaction of natural gas at an operation temperature of 750 °C. As outlined in chapter 4 and as further discussed in chapter 9, this hypothesis is based on the fact that the documented methane conversion characteristics shown by Serban make it difficult finding explanations for the observed methane conversion other than catalytic activity of liquid tin.

According to the Popperesque intrinsic validation methodology of the falsification process, several basic hypotheses had to be stated which allow a conclusion on whether or not the hypothesis may be considered false or not. In view thereof, chapter 4 states three basic hypothesis that served as basis for experimental investigations, which had been subject of this thesis. Now, the obtained results of the latter experiments shall be evaluated in the context of their corresponding basic hypothesis.

10.1 Bubble size and bubble rise velocity dependencies

Basic hypothesis BH_3 states that *"Bubble size and bubble rise velocities of gas injected into liquid tin using a porous sparger are significantly flow rate dependent"*.

It is not agreed thereto. Experiments using a porous sparger for the dispersion of gas into liquid metal have shown that the bubbles formed are only to a very limited extent dependent on the applied flow rate. In detail, during an exemplary experiment in liquid tin at 300 °C, an increase of the volumetric gas flow rate from 25 mln/min to 200 mln/min only caused a very small increase of the bubble rise velocity. Simultaneously, the bubble frequency almost doubles at the location of the sensor alone. Due to the disc-like

sparger device, the formed bubbles were spread over a large cross-sectional area of the reactor tube and could not be detected altogether. Fig. 10.1 illustrates the measured bubble rise velocities together with the measured bubble frequencies.

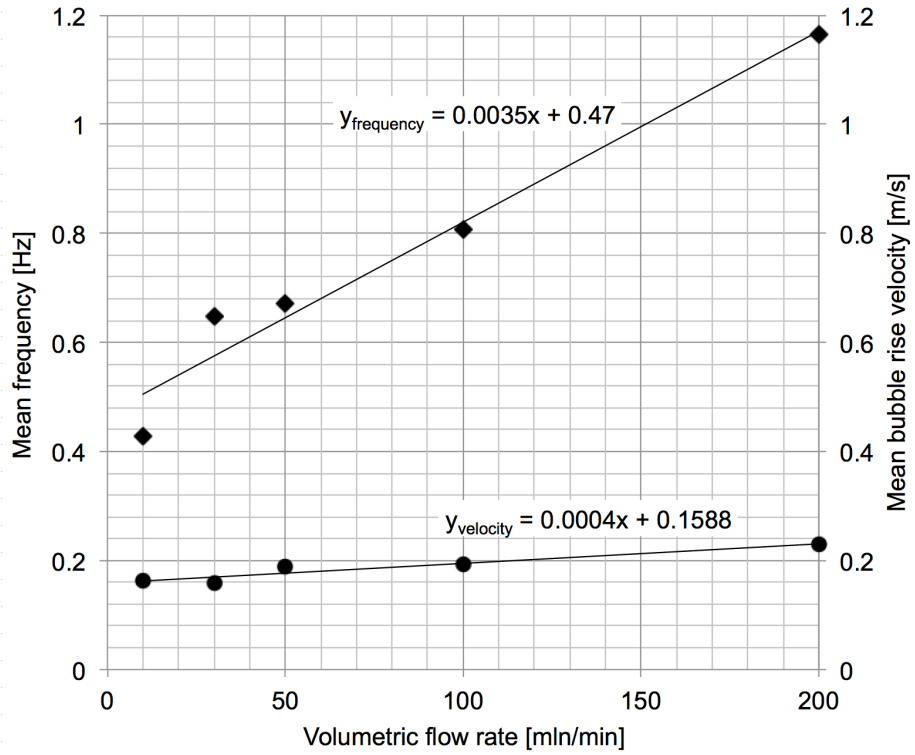

Figure 10.1: Overview of the experimental results. Obtained bubble frequencies (⧫) and mean bubble rise velocities (●) are shown for various flow rates of Ar gas injected into liquid tin at 300 °C using a reactor according to the previously introduced embodiment.

10.2 The presence of tin and its relation with methane conversion as a function of the gas residence time

According to the previous section, smaller flow rates will not substantially increase the bubble residence time, neither the specific interface area between gas and liquid. However, it may still be observed from Serban's experiments that if liquid tin is

present, methane conversion increases much faster for longer gas residence times, hence smaller feed gas flow rates. The subject-matter of BH_2 claims that *"at an operation temperature of 750 °C, runs without tin show an increase in methane decomposition for longer gas residence times, yet with a softer slope compared to runs with liquid tin"*.

Said hypothesis is based on the conversion data provided by Serban et al. [5], as shown in fig. 10.2. Here, two experimental runs are shown; runs with liquid metal are represented by dots connected with the solid line and runs conducted without liquid metal are shown in dashed lines.

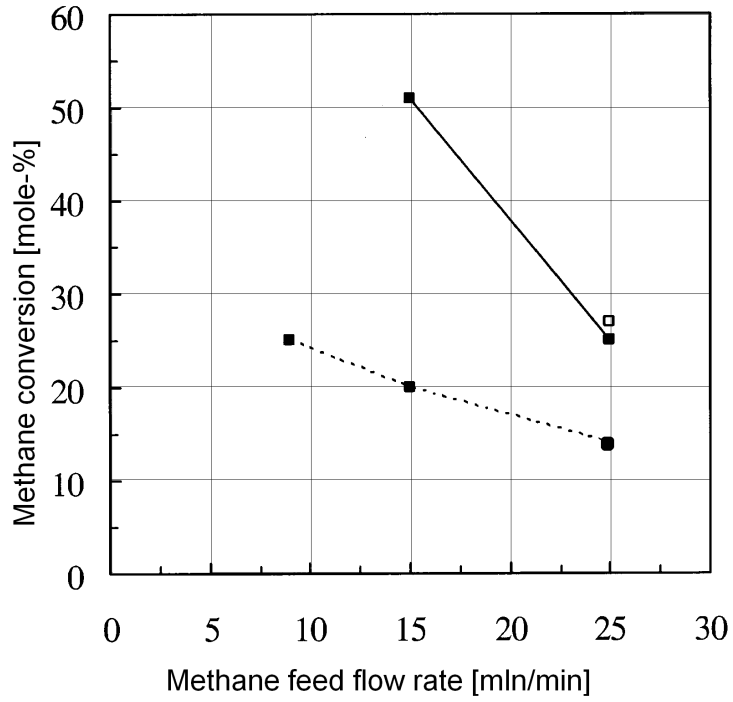

Figure 10.2: Methane conversions in natural gas pyrolysis over 4-in. molten Sn (solid line) or blank runs (dashed line) bubbled through a 0.5 μm (■) Mott sparger at 750°C. Symbol (□) indicates repeated pyrolysis experiments. All shown experiments conducted by Serban et. al [5].

In order to test basic hypothesis BH_2, Serban's experimental scheme was adopted during own experiments. One reactor was operated at a given temperature with and without the presence of liquid metal. By doing so, the dependencies of the gas residence time on

the conversion shall be compared for both runs. Unfortunately, due to the very small conversion rates at 750 °C observed during runs with a liquid metal bubble column, no useful data was obtained during own experiments. As a matter of fact, such result already falsifies hypothesis BH_2. However, one may assume that if BH_2 was false, it could also be verified false for a wider range of operation conditions. Therefore, present hypothesis shall be assessed in a wider operation range. In this respect, a comparison of the conversion performance for both reactor configurations is provided in fig. 10.3. Here, it is shown that the slopes with and without the presence of liquid tin are more or less identical. The tendency observed by Serban, characterized in that if liquid metal is present, the gas residence time sensitivity increases substantially, cannot be depicted. As a consequence, the hypothesis BH_2 may be considered falsified herewithin.

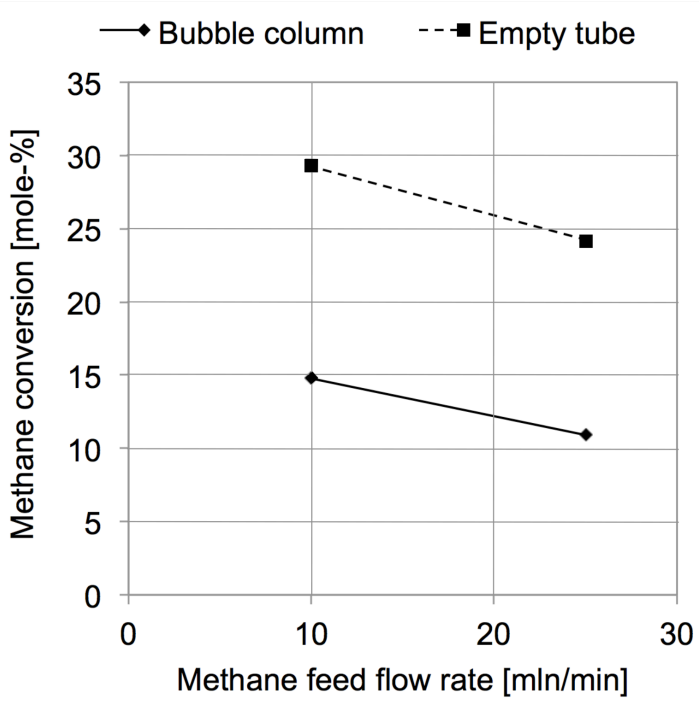

Figure 10.3: Comparison of conversion slopes for runs with liquid metal and runs with an empty-tube reactor. Data taken from own experiments, operated at 900 °C.

10.3 The presence of tin and its impact on the operation temperature

Basic hypothesis BH_1 states that *"At 750 °C and at similar gas residence times compared to Serban et al., runs with liquid metal yield a higher conversion rate compared to runs without liquid metal"*.

BH_1 can be falsified without looking into a detailed analysis of results. In fact, during all experiments conducted at 750 °C, both with or without liquid metal present in the reactor, the maximum observed conversion was a strikingly low value of 0.9 % in methane conversion. This result was achieved during runs with an empty-tube reactor at a gas residence time of about 60 min. Results in liquid metal were even ten times smaller, as shown in chapter 8. Serban's highest observed methane conversion at 750 °C was obtained at a gas residence of about 3 min and yielded a methane conversion of more than 50%. Own experiments at a gas residence time of 3 min yielded no conversion within a detectable range, hence below 0.01%. In other words, repeating Serban's experiment conditions in terms of applied gas residence time and operation temperature do not lead to any methane conversion above 0.05 mole-%. Therefore, the above stated hypothesis needs to be considered false.

10.4 Catalytic activity of liquid tin for the TDM reaction

As a matter of fact, methane conversion observed during own experiments was frustratingly low, particularly during an operation temperature of 750 °C. It is not clear, how the extremely high conversion rates provided by Serban et al. [5] had been achieved. One

possibility would be that the operation pressure was lowered dramatically. However, no reference is made regarding the operation pressure within the work of Serban et al. On the other hand, if a lower pressure was in fact the cause for the alleged high conversion rates, runs with liquid metal should not comprise such high values, since the hydrostatic pressure of liquid tin inflicts additional pressure to gas bubbles submerged in the liquid.

Even at higher temperatures, not only the conversion rates as provided by Serban were not achieved, but also the alleged gas-residence time and reactor configuration related conversion-tendencies claimed by Serban were falsified, as shown before. In summary, it must be concluded that within the observed range of operation conditions, the reaction of thermal decomposition of methane is merely driven by the applied temperature and gas residence time. The hypothesis, claiming that *"at an operation temperature of about 750 °C, liquid tin has a catalytic impact on the decomposition of natural gas, particularly methane".* therefore must be considered false in view of the herewithin considered experiments.

In view thereof, a new hypothesis NH shall be stated according to

New Hypothesis (NH_1) *At temperatures in the range of about 700 °C and up to 950 °C, at absolute gas pressures in the range of 1.01 to 1.1 bar and at methane residence times of up to 5 seconds, no catalycity of liquid tin on the overall reaction of hydrogen formation by thermal methane decomposition can be observed.*

Chapter 11

Summary and Outlook

The main objective of this thesis was to identify and investigate a process for thermal decomposition of methane for the purpose of hydrogen production. Thermal decomposition of methane is a pyrolytic reaction which decomposes methane into its elementary substances hydrogen and carbon as final products. The reaction itself is moderately endothermal, however relatively high operation temperatures beyond 500 °C, are required in order to obtain measurable conversion results. In fact, most experiments documented in literature experiments considered operation temperatures higher than 1000 °C. An in-depth literature survey prefigured that the formation of solid carbon, a reaction by-product of the thermal decomposition TDM, is likely to be the main obstacle when trying to achieve a continuously operable TDM process. That is, because the formed solid carbon tends to stick to any solid surface on which the TDM reaction proceeded due to thermal or thermo-catalytical reaction phenomena. Two disadvantageous effects have been identified in this matter. First, in almost all studies where methane conversion was observed, solid carbon blocks the gas flow by its sole presence within the reactor entity and second, catalytically active surfaces are also functionally deteriorated according to

the degree of carbon coverage. In view thereof, during the initial stage of designing the experiment, it was found to utilize a liquid surface as boundary surface to the pyrolysis gas instead of a solid surface. Here, the solid carbon formed during reaction was expected to be washed atop of the liquid surface and even further, for each gas bubble formed, a new carbon-clean bubble-inner surface was expected to form.

For the above-referenced process, liquid tin was identified as being most suitably as a heat transfer fluid and -according to Serban et al. [5]- even with the possibility of comprising catalytical impacts on the TDM reaction. In a further step, among a variety of different chemical reactor candidates, the liquid bubble column reactor was chosen due to its promising two-phase phenomena and also because of the possibility to remove carbon from it during operation.

One specific prior art document provided by Serban et al. [5] discloses quite promising methane conversion rates of methane in a liquid tin bubble column reactor. In fact, more than 50% of methane conversion was achieved at an operation temperature of only 750 °C. On the basis of these results and further comparative experiments discussed therewithin, a hypothesis was postulated, claiming that liquid tin must have a catalytical impact on the TDM reaction. According to the falsification theory presented by Karl Popper, several basic hypotheses were defined; serving as the basis for subsequent experiments. Said basic hypotheses tackled the methane conversion at 750 °C at a given gas residence time, the comparison of runs in the presence and in the absence of liquid tin, as well as the question, whether a change in flow rate changes the gas bubble size and gas bubble rise velocity.

Referring to gas bubble characteristics and thus, the third basic hypothesis, it was shown that a change in the applied gas flow rate does not significantly change the bubble

size and the bubble rise velocity. Rather, the change in flow rate is more or less solely compensated by a change in bubble frequency; hence more bubbles of the same features. From a conversion performance point of view, an increase in bubble frequency does not lead to a change in conversion, since all gas bubbles behave similarly. As a consequence, methane conversion occurring within the liquid metal bubble column shall only marginally be dependent on the applied flow rate. Furthermore, it was indicated by the model and also indirectly by gas-phase-only experiments that conversion in the liquid phase was negligibly small. The latter is most likely linked to the comparably short gas residence time inside of the liquid phase, being in the range of a few seconds. However, the model indicated that the methane heat-up was effectively completed within the liquid phase.

Referring to the first and second basic hypothesis, several experimental campaigns to investigate the thermal dissociation of methane in liquid metal bubble columns and also runs with a blank tube were carried out and compared with a thermo-chemical model of the reactor processes using various kinetic parameters obtained from the literature. Since this study observed the influence of a flow rate variation at three different nominal temperatures on the methane conversion ratio, the presented model has been used to explain the gas heat-up before and chemical conversion after the intended reaction zone, the liquid metal bubble column as well as the blank tube section. The model has been applied using different kinetic parameters from various sources. Results with own experimental data show, that although a universal agreement cannot be found, kinetic data obtained from homogeneous reaction experiments tend to show a better agreement compared to data gained from heterogeneous experiments. For runs with a blank tube reactor, best agreement for kinetic data taken from Rodat et al. [24] at a wide range of temperature and flow rates. Conversion rates of experiments in liquid metal at

900 °C were best modeled using kinetic data from Kozlov et al. [40] and Kevorkian et al. [37]; in case of the 850 °C experiments, Rodat et al. [24] showed the best agreement. For a conclusion, the results show, that for a significant methane conversion, the operation temperature and/or the gas residence time needs to be increased further. Since existing literature lacks suitable kinetic data, further experiments are needed to investigate the potential of thermal decomposition of methane using liquid metal as heat transfer fluid.

To conclude, thermo-chemical models considering a first order reaction for the decomposition of methane to hydrogen yield conversion results that are within the same order of magnitude, consistently in itself and when compared to own experiments. However, if the same modeling principles are applied to the reactor shown by Serban et al. [5], the thermo-chemical results differ by two orders of magnitude for runs in the absence of tin and by three orders of magnitude in the presence of tin. Therefore, the strikingly high conversion results as reported by Serban et al. [5] could not be explained or repeated within this thesis.

On the contrary, it was found that the observed methane conversion occurred within the gaseous sections of the reactor, rather than within the liquid sections of it, and that the TDM reaction is merely depending on the state of the gas (temperature and pressure) and the gas residence time within the reactor. It is suggested that the impact of liquid tin shall further be investigated in more detail. To do so, it is crucial to a) reduce hot gas volumes inside of the reactor in order to avoid conversion outside of the liquid and b) to increase the gas residence time within the liquid. The latter may be achieved by means of different reactor improvements, for example by including a packed bed or the like to the liquid phase.

Apart from the results gained with respect to the conversion characteristics in the liquid and gaseous sections of a liquid tin bubble column reactor, several reactor-design related insights had been achieved. First of all, it was proven that the concept of injecting methane into liquid tin at the bottom of the reactor is in fact advantageous in terms of avoiding carbon formation in the feed tubes; a common problem that was identified in almost all known studies related to thermal decomposition of methane. Secondly, post-processing of the liquid phase, which was carried out in parallel from colleagues of the IHM at KIT, surfaced that carbon was not found within the tin, but only on top of the frozen tin surface and on of the reactor-inner boundary surfaces in the gas section and the gas filter in the exhaust tube. The latter indicates that liquid tin might be effectively separating the carbon on top of the liquid tin surface. This thesis included constructing the entire experimental facility and defining suitable reactor materials, reactor design and the integration of the reactor into a facility that allows a continuous operation at the envisaged operation conditions. At the beginning of this thesis, a quartz-glass reactor was foreseen as the ideal reactor material, since all corrosion related adversities would have been avoided. However, since several material- and production-related obstacles could not be overcome in due time, quartz-glass was not used. In view of the latest operational reactor generation 2.1 within this thesis, it may be concluded that future reactors should ideally be made of quartz-glass material, comprising a single-hole orifice at the reactor bottom.

Bibliography

[1] M. Granovskii, I. Dincer, and M. A. Rosen, "Life cycle assessment of hydrogen fuel cell and gasoline vehicles," *International Journal of Hydrogen Energy*, vol. 31, no. 3, pp. 337 – 352, 2006. Fuel Cells.

[2] R. Kothari, D. Buddhi, and R. Sawhney, "Comparison of environmental and economic aspects of various hydrogen production methods," *Renewable and Sustainable Energy Reviews*, vol. 12, no. 2, pp. 553 – 563, 2008.

[3] J. Dufour, D. Serrano, J. Gilvez, J. Moreno, and C. Garcia, "Life cycle assessment of processes for hydrogen production. Environmental feasibility and reduction of greenhouse gases emissions," *International Journal of Hydrogen Energy*, vol. 34, no. 3, pp. 1370 – 1376, 2009.

[4] F. Romagnoli, D. Blumberga, and I. Pilicka, "Life cycle assessment of biohydrogen production in photosynthetic processes," *International Journal of Hydrogen Energy*, vol. 36, no. 13, pp. 7866 – 7871, 2011. Hysydays.

[5] M. Serban, M. A. Lewis, C. L. Marshall, and R. D. Doctor, "Hydrogen production by direct contact pyrolysis of natural gas," *Energy & Fuels*, vol. 17, no. 3, pp. 705–713, 2003.

[6] N. Muradov, F. Smith, C. Huang, and A. T-Raissi, "Autothermal catalytic pyrolysis of methane as a new route to hydrogen production with reduced co2 emissions," *Catalysis Today*, vol. 116, no. 3, pp. 281 – 288, 2006. 2nd European Hydrogen Energy Conference.

[7] International Energy Agency (IEA),"Energy Technology Perspectives 2012," 2012.

[8] H. F. Abbas and W. W. Daud, "Hydrogen production by methane decomposition: A review," *International Journal of Hydrogen Energy*, vol. 35, no. 3, pp. 1160 – 1190, 2010.

[9] A. Iulianelli, P. Ribeirinha, A. Mendes, and A. Basile, "Methanol steam reforming for hydrogen generation via conventional and membrane reactors: A review," *Renewable and Sustainable Energy Reviews*, vol. 29, no. 0, pp. 355 – 368, 2014.

[10] P. Spath, M. Mann, and N. R. E. L. (US), *Life cycle assessment of hydrogen production via natural gas steam reforming*. National Renewable Energy Laboratory, 2000.

[11] A. Ozbilen, I. Dincer, and M. Rosen, "A comparative life cycle analysis of hydrogen production via thermochemical water splitting using a cu-cl cycle," *International Journal of Hydrogen Energy*, vol. 36, no. 17, pp. 11321 – 11327, 2011. International Conference on Hydrogen Production (ICH2P)-2010.

[12] U. Ashik, W. W. Daud, and H. F. Abbas, "Production of greenhouse gas free hydrogen by thermocatalytic decomposition of methane," *Renewable and Sustainable Energy Reviews*, vol. 44, pp. 221 – 256, 2015.

[13] T. Kodama, "High temperature solar chemistry for converting solar heat to chemical fuels," *Progress in Energy and Combustion Science*, vol. 29, no. 6, pp. 567 – 597, 2003.

[14] T. Smolinka, E. T. Ojong, and J. Garche, "Chapter 8 - hydrogen production from renewable energies-electrolyzer technologies," in *Electrochemical Energy Storage for Renewable Sources and Grid Balancing* (P. T. M. Garche, ed.), pp. 103 – 128, Amsterdam: Elsevier, 2015.

[15] M. Wullenkord, *Determination of Kinetic Parameters of the Thermal Dissociation of Methane*. PhD thesis, Rheinisch-Westfälischen Technischen Hochschule Aachen, 2011.

[16] A. Dominguez, B. Fidalgo, Y. Fernández, and J. Pis, "Microwave-assisted catalytic decomposition of methane over activated carbon for -free hydrogen production," *International Journal of Hydrogen Energy*, vol. 32, no. 18, pp. 4792 – 4799, 2007.

[17] B. Fidalgo, Y. Fernández, A. Dominguez, and J. Pis, "Microwave-assisted pyrolysis of ch4/n2 mixtures over activated carbon," *Journal of Analytical and Applied Pyrolysis*, vol. 82, no. 1, pp. 158 – 162, 2008.

[18] W.-H. Chen, H.-J. Liou, and C.-I. Hung, "A numerical approach of interaction of methane thermocatalytic decomposition and microwave irradiation," *International Journal of Hydrogen Energy*, vol. 38, no. 30, pp. 13260 – 13271, 2013.

[19] L. Fulcheri and Y. Schwob, "From methane to hydrogen, carbon black and water," *International Journal of Hydrogen Energy*, vol. 20, no. 3, pp. 197 – 202, 1995.

[20] L. Fulcheri, N. Probst, G. Flamant, F. Fabry, E. Grivei, and X. Bourrat, "Plasma processing: a step towards the production of new grades of carbon black," *Carbon*, vol. 40, no. 2, pp. 169 – 176, 2002. Third International Conference on Carbon Black.

[21] N. Muradov, F. Smith, G. Bockerman, and K. Scammon, "Thermocatalytic decomposition of natural gas over plasma-generated carbon aerosols for sustainable production of hydrogen and carbon," *Applied Catalysis A: General*, vol. 365, no. 2, pp. 292 – 300, 2009.

[22] C.-H. Tsai and K.-T. Chen, "Production of hydrogen and nano carbon powders from direct plasmalysis of methane," *International Journal of Hydrogen Energy*, vol. 34, no. 2, pp. 833 – 838, 2009.

[23] M. Dors, H. Nowakowska, M. Jasinski, and J. Mizeraczyk, "Chemical kinetics of methane pyrolysis in microwave plasma at atmospheric pressure," *Plasma Chemistry and Plasma Processing*, vol. 34, no. 2, pp. 313–326, 2014.

[24] S. Rodat, S. Abanades, J. Coulio, and G. Flamant, "Kinetic modelling of methane decomposition in a tubular solar reactor," *Chemical Engineering Journal*, vol. 146, no. 1, pp. 120 – 127, 2009.

[25] A. Abánades, C. Rubbia, and D. Salmieri, "Technological challenges for industrial development of hydrogen production based on methane cracking," *Energy*, vol. 46, no. 1, pp. 359 – 363, 2012. Energy and Exergy Modelling of Advance Energy Systems.

[26] A. M. Dunker, S. Kumar, and P. A. Mulawa, "Production of hydrogen by thermal decomposition of methane in a fluidized-bed reactor: Effects of catalyst, temperature, and residence time," *International Journal of Hydrogen Energy*, vol. 31, no. 4, pp. 473 – 484, 2006.

[27] N. Shah, D. Panjala, and G. P. Huffman, "Hydrogen production by catalytic decomposition of methane," *Energy & Fuels*, vol. 15, no. 6, pp. 1528–1534, 2001.

[28] D. Paxman, S. Trottier, M. Nikoo, M. Secanell, and G. Ordorica-Garcia, "Initial experimental and theoretical investigation of solar molten media methane cracking for hydrogen production," *Energy Procedia*, vol. 49, no. 0, pp. 2027 – 2036, 2014. Proceedings of the SolarPACES 2013 International Conference.

[29] M. Plevan, L. Stoppel, T. Wetzel, A. Heinzel, A. Weisenburger, G. Müller, C. Fazio, J. Konys, C. Schroer, C. Rubbia, A. Abánades, C. F. C., A. Ghannadzadeh, S. Stückrad, and D. Salmieri, "Hydrogen production via direct thermal cracking of methane: Concept of a molten metal bubble column reactor," *Proc. Of the 5th World Hydrogen Technologies Convention (WHTC2013)*, vol. 5, p. 111, 2013.

[30] S. Krzyzynski, "Activated carbons as catalysts for hydrogen production via methane decomposition," *International Journal of Hydrogen Energy*, vol. 33, no. 21, pp. 6172 – 6177, 2008.

[31] K. K. Lee, G. Y. Han, K. J. Yoon, and B. K. Lee, "Thermocatalytic hydrogen production from the methane in a fluidized bed with activated carbon catalyst," *Catalysis Today*, vol. 93 - 95, no. 0, pp. 81 – 86, 2004. Selections from the presentations of the 3rd Asia-Pacific Congress on Catalysis.

[32] N. Muradov, F. Smith, and A. T-Raissi, "Catalytic activity of carbons for methane decomposition reaction," *Catalysis Today*, vol. 102 - 103, no. 0, pp. 225 – 233, 2005.

[33] I. Suelves, J. Pinilla, M. Lázaro, and R. Moliner, "Carbonaceous materials as catalysts for decomposition of methane," *Chemical Engineering Journal*, vol. 140, no. 1-3, pp. 432 – 438, 2008.

[34] C.-J. Chen, M. H. Back, and R. A. Back, "The thermal decomposition of methane. i. Kinetics of the primary decomposition to C2H6 + H2; rate constant for the homogeneous unimolecular dissociation of methane and its pressure dependence," *Canadian Journal of Chemistry*, vol. 53, no. 23, pp. 3580–3590, 1975.

[35] L. S. Kassel, "The thermal decomposition of methane," *Journal of the American Chemical Society*, vol. 54, no. 10, pp. 3949–3961, 1932.

[36] G. B. Skinner and R. A. Ruehrwein, "Shock tube studies on the pyrolysis and oxidation of methane," *The Journal of Physical Chemistry*, vol. 63, no. 10, pp. 1736–1742, 1959.

[37] V. Kevorkian, C. E. Heath, and M. Boudart, "The decomposition of methane in shock waves," *The Journal of Physical Chemistry*, vol. 64, no. 8, pp. 964–968, 1960.

[38] M. Steinberg, "Production of hydrogen and methanol from natural gas with reduced CO2 emission," *International Journal of Hydrogen Energy*, vol. 23, no. 6, pp. 419 – 425, 1998.

[39] P. S. Shantarovic and B. V. Pavlov, "Thermal cracking of methane," *International Chemical Engineering*, vol. 2, no. 3, pp. 415–418, 1962.

[40] G. Kozlov and V. Knorre, "Single-pulse shock tube studies on the kinetics of the thermal decomposition of methane," *Combustion and Flame*, vol. 6, no. 0, pp. 253 – 263, 1962.

[41] H. B. Palmer and T. J. Hirt, "The activation energy for the pyrolysis of methane1," *The Journal of Physical Chemistry*, vol. 67, no. 3, pp. 709–711, 1963.

[42] B. Alchagirov and A. Chochaeva, "Temperature dependence of the density of liquid tin," *High Temperature*, vol. 38, no. 1, pp. 44–48, 2000.

[43] B. Alchagirov, O. Kurshev, and T. Taova, “Surface tension of tin and its alloys with lead,” *Russian Journal of Physical Chemistry A*, vol. 81, no. 8, pp. 1281–1284, 2007.

[44] M. J. Assael, A. E. Kalyva, K. D. Antoniadis, R. Michael Banish, I. Egry, J. Wu, E. Kaschnitz, and W. A. Wakeham, “Reference data for the density and viscosity of liquid copper and liquid tin,” *Journal of Physical and Chemical Reference Data*, vol. 39, no. 3, pp. –, 2010.

[45] A. Mersmann, “Auslegung und Maßstabsvergrößerung von Blasen- und Tropfensäulen,” *Chemie Ingenieur Technik*, vol. 49, no. 9, pp. 679–691, 1977.

[46] A. Mersmann, M. Kind, and J. Stichlmair, *Thermische Verfahrenstechnik*. Springer, 2005.

[47] B. Kraushaar-Carnetzki and R. Dittmeyer, *Chemische Verfahrenstechnik Skript*. Institut für Chemische Verfahrenstechnik CVT, Karlsruher Institut für Technologie KIT, 09 2014.

[48] M. Suppes, “Method of skimming slag from molten metal.,” Jan. 9 1906. US Patent 809,405.

[49] W. Ruff, “Bath constituent(s) removal method from metal crucible, using liquid metal(s),” July 23 1998. DE Patent App. DE1,997,101,679.

[50] P. Bourke and D. Taylor, “Flotation machine,” Aug. 9 2005. US Patent 6,926,154.

[51] G. Abel, “Apparatus for de-slagging casting ladles,” May 13 1975. US Patent 3,883,124.

[52] A. Blank, “Mechanical skimmer,” Mar. 2 1976. US Patent 3,941,360.

[53] P. Klotz and H. Bottcher, “Process and apparatus for removing a layer of fluid on top of a bath,” Nov. 15 1983. US Patent 4,415,144.

[54] H. Matsunaga, K. Ishikura, K. Imamura, F. Kato, S. Mineyuki, and A. Minami, “Method for removing slag on the surface of molten metal by suction,” Sept. 22 1982. EP Patent App. EP19,820,301,304.

[55] Y. Sahai and R. Guthrie, “Hydrodynamics of gas stirred melts: Part i. Gas/liquid coupling,” *Metallurgical Transactions B*, vol. 13, no. 2, pp. 193–202, 1982.

[56] K. Popper, “The Logic of Scientific Discovery,” *Rev. Ed. London, Hutchinson*

[57] J. C. M. Mohr, “Karl Popper - Lesebuch,” *Paul Siebeck, 1995*

[58] D. T. Early, *The Tension Between Falsificationism and Realism: A Critical Examination of a Problem in the Philosophy of Karl Popper*. PhD thesis, Faculty of the Virginia Polytechnic Institute and State University, 1999.

[59] M. Sano and K. Mori, "Dynamics of bubble swarms in liquid metals," *Transactions of ISIJ*, vol. 20, pp. 668–674, 1980.

[60] M. Iguchi, T. Nakatani, and H. Tokunaga, "The shape of bubbles rising near the nozzle exit in molten metal baths," *Metallurgical and Materials Transactions B*, vol. 28, no. 3, pp. 417–423, 1997.

[61] M. Iguchi, T. Nakatani, and H. Kawabata, "Development of a multineedle electroresistivity probe for measuring bubble characteristics in molten metal baths," *Metallurgical and Materials Transactions B*, vol. 28, no. 3, pp. 409–416, 1997.

[62] M. Iguchi, H. Kawabata, K. Nakajima, and Z.-I. Morita, "Measurement of bubble characteristics in a molten iron bath at 1600 c using an electroresistivity probe," *Metallurgical and Materials Transactions B*, vol. 26, no. 1, pp. 67–74, 1995.

[63] Y. Saito, K. Mishima, Y. Tobita, T. Suzuki, and M. Matsubayashi, "Measurements of liquid metal two-phase flow by using neutron radiography and electrical conductivity probe," *Experimental Thermal and Fluid Science*, vol. 29, no. 3, pp. 323 – 330, 2005. Third European-Japanese Two-Phase Flow Group Meeting.

[64] Y. Saito, X. Shen, K. Mishima, and M. Matsubayashi, "Shape measurement of bubble in a liquid metal," *Nuclear Instruments and Methods in Physics Research Section A: Accelerators, Spectrometers, Detectors and Associated Equipment*, vol. 605, no. 1-2, pp. 192 – 196, 2009. Proceedings of the sixth Topical Meeting on Neutron Radiography.

[65] R. Andreini, J. Foster, and R. Callen, "Characterization of gas bubbles injected into molten metals under laminar flow conditions," *Metallurgical Transactions B*, vol. 8, no. 3, pp. 625–631, 1977.

[66] S. Herbst, "Blasenaufstiegsverhalten in einem Flüssigmetall-Blasensäulenreaktor: Experimentelle Untersuchung," Master's thesis, Karlsruher Institut für Technologie KIT, 2013.

[67] M. Plevan, T. Geißler, S. Herbst, L. Stoppel, and T. Wetzel, "Experimental investigation of bubble rise velocities in a molten metal bubble column reactor," *Proc. of the 11th Multiphase Flow Conference & Short Course*, 2013.

[68] R. Clift, J. R. Grace, and M. E. Weber, *Bubbles, drops, and particles*. Courier Dover Publications, 2005.

[69] A. Weisenburger, A. Heinzel, G. Müller, and A. Abanades, “Materials for hydrogen production by direct methane conversion - tests in liquid tin at high temperatures” in *The Energy and Materials Research Conference (EMR 2015)*, Madrid, E, February 25- 27, 2015 Book of Abstracts. Courier Dover Publications, 2005.

[70] P. Von Böckh and T. Wetzel, *Wärmeübertragung*. Springer, 2003.

[71] M. Plevan, T. Geißler, S. Herbst, L. Stoppel, and T. Wetzel, “Experimental investigation of bubble rise velocities in a molten metal bubble column reactor.,” in *Proc. of the 11th Multiphase Flow Conference & Short Course*, 2013.

[72] S. Sharafat and G. N., “Summary of thermo-physical properties of Sn, and compounds of Sn-H, Sn-O, Sn-C, Sn-Li, and Sn-Si and comparison of properties of Sn, Sn-Li, Li, and Pb-Li,” *APEX Study University of California Los Angeles*, vol. -, pp. –, 2000.

[73] M. Steinberg, “Fossil fuel decarbonization technology for mitigating global warming,” in *International Journal of Hydrogen Energy* ,1999, 24, 771 - 777

Nomenclature

Abbreviations and acronyms

CCS	Carbon Capture and Sequestration
CSP	Concentrated Solar Power
CSTR	Continuous Stirred-Tank Reactor
ICE	Internal Combustion Engine
IEA	International Energy Agency
LDV	Light Duty Vehicle
LM	Liquid Metal
PEMFC	Proton Exchange Membrane Fuel Cell
PFR	Plug Flow Reactor
PSA	Pressure Swing Adsorption
TDM	Thermal Decomposition of Methane
UDV	Ultrasonic Doppler Velocimetry

Roman letters

A	Cross-sectional area	[m^2]
$\dot{m}$	Mass flow	[kg s^{-1}]
$\dot{V}$	Flow rate	[ml min^{-1}]
ΔH	Reaction enthalpy	[J mol^{-1}]

ΔH_R^0	Standard reaction enthalpy	[J mol^{-1}]
C_D	Drag coefficient	[-]
C_i	Concentration of a species	[mol m^{-3}]
c_p	Specific heat capacity	[J kg^{-1} K^{-1}]
D	Diffusion coefficient	[m^2 s^{-1}]
d	Pipe diameter	[m]
E	Energy	[J mol^{-1}]
f	Frequency	[s^{-1}]
h	Filling height	[m]
h_f	Formation enthalpy	[J mol^{-1}]
k_0	Pre-exponential factor	[s^{-1}]
L	Length	[m]
p	Pressure	[bar]
R	Electric resistance	[Ω]
r	Reaction rate s^{-1}	[mol m^{-3}]
T	Temperature	[K]
t	Time	[s]
V	Volume	[m^3]
v	Rise velocity	[m s^{-1}]
w	Fluid particle velocity	[m s^{-1}]
X	Conversion	[-]
Z	Vertical axis	[-]
$\Re$	Universal gas constant	[$R = 8.314$J (mol K)$^{-1}$]
g	Gravity	[$g = 9.80665$m s^{-1}]

Greek letters

α	Heat transfer coefficient	[W m^{-2} K^{-1}]

ϵ	Volumetric expansion factor	[-]
λ	Thermal conductivity	[W m^{-1} K^{-1}]
ρ	Density	[kg m^{-3}]
σ	Surface tension	[kg s^{-2} K^{-1}]
τ	Space time	[s^{-1}]
θ	Non-dimensional temperature	[-]

Non-dimensional numbers

Bi	Biot number
Eo	Eötvos number
Fr	Froude number
Mo	Morton number
Nu	Nusselt number
Pe	Peclet number
Pr	Prandtl number
Re	Reynolds number
We	Weber number

Subscripts

0	Initial value, entry value
∞	Reference
B	Bubble
c	Continuous phase
crit	Critical
d	Disperse phase
DAQ	Data acquisition converter
g	Gas
in	Inlet

LM	Liquid metal
m	Mean
max	Maximum
n	Order of reaction
O	Orifice
out	Outlet
PFR	Plug flow reactor
Pre	Preheat
R	Reaction
res	Residence
S	Sensor
s	Solid
Sn	Liquid tin
STP	Normalized conditions
W	Wall
x	Non-dimensional length
i	Molecular species
t	terminal

Chapter 12

Appendix: TDM Experiments

12.1 Generation 2.1 experiments: Successful experiments using a liquid metal bubble column reactor

Figs. 12.1 and 12.2 depict some of the data which was measured during runs with liquid tin. The plots show temperature, pressure and flow rate values arranged in chronological order. More precisely, temperature and flow rate data are arranged on the left Y-axis (primary) and pressure values are arranged on the right Y-axis (secondary). Each vertical line represents a gas chromatography measurement, referring to the actual conversion time inside the reactor taking into account the time delay caused by the flushing time t_{flush}[1] and the retention time of the gas chromatograph itself.

[1]The flushing time was calculated as the three-fold of the theoretical gas residence time, which was calculated on the basis of an ideal gas and the assumption of a bubble rise velocity of 100 mm/s for the gas inside of the liquid metal section of the reactor.

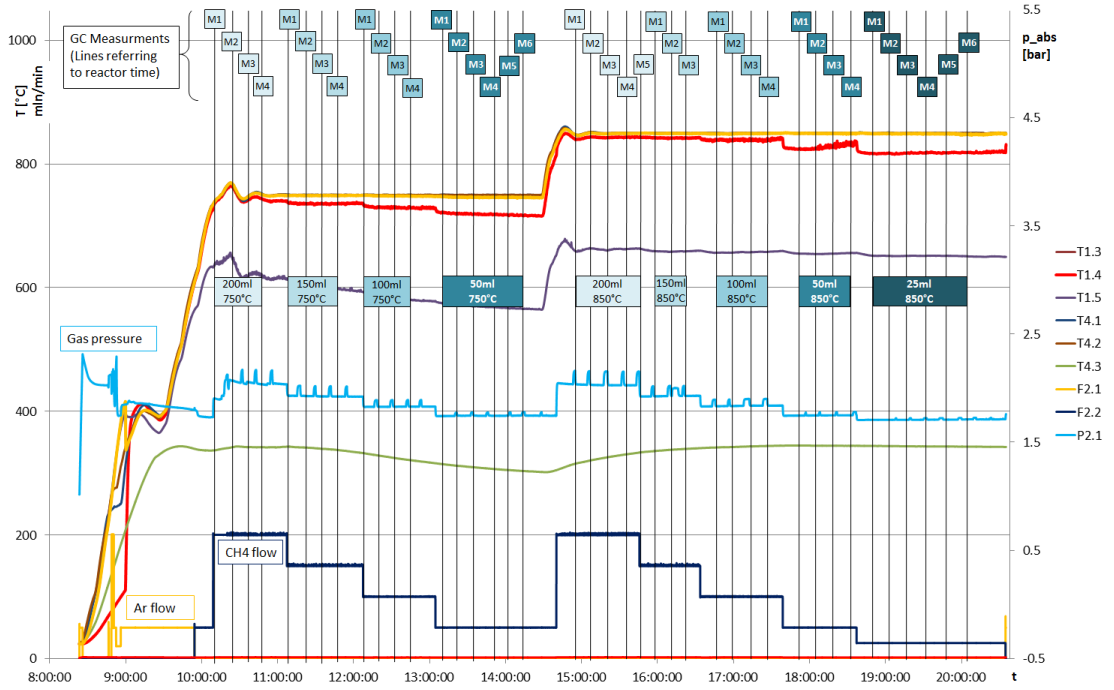

Figure 12.1: Plant operating data including GC measurements referring to the actual gas conversion time inside the reactor for day 1

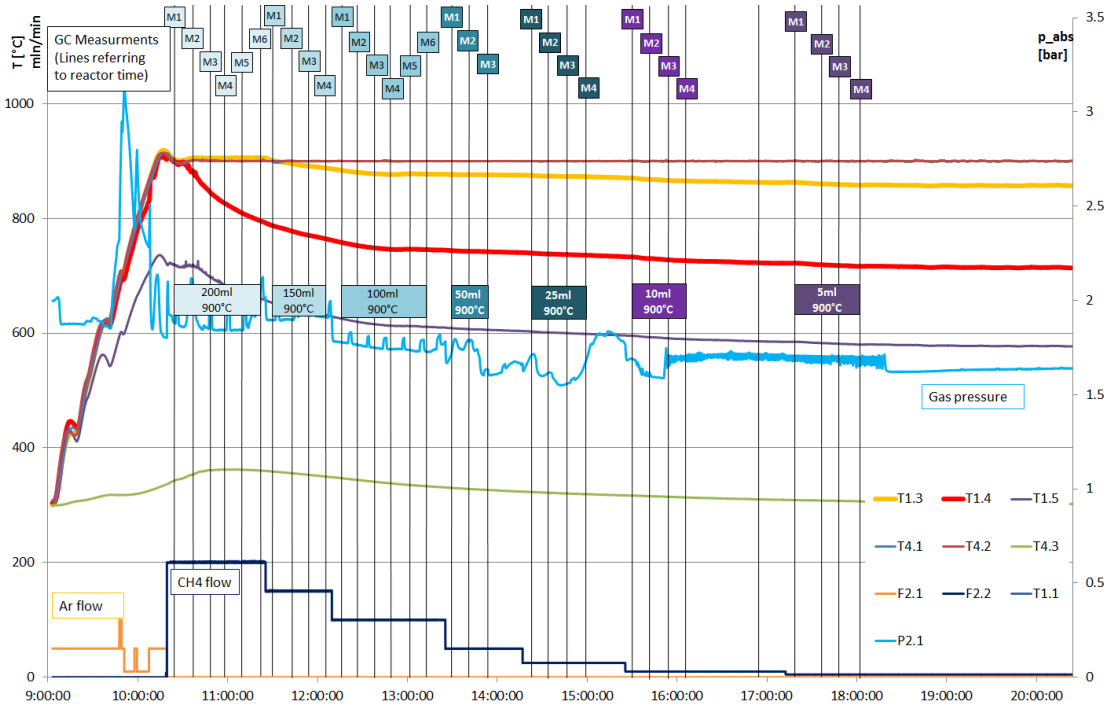

Figure 12.2: Plant operating data including GC measurements referring to the actual gas conversion time inside the reactor for day 2

12.2 Generation 2.2 experiments: Additional experiments using a gas-phase reactor

Reference temperature: 750°C			
Flow rate	Reactor residence time	Reactor residence time	Total gas residence time
mln/min	min	min	min
5	60	181	207
10	30	90	103
25	12	36	41
50	6	18	21
100	3	9	10
150	2	6	7
200	2	5	5

Table 12.1: Table showing the calculated gas residence times for the reactor at 750 °C, assuming pure methane and ideal gas law

Reference temperature: 850°C			
Flow rate	Reactor residence time	Reactor residence time (3-fold)	Total gas residence time (3-fold)
mln/min	min	min	min
5	55	164	191
10	27	82	95
25	11	33	38
50	5	16	19
100	3	8	10
150	2	5	6
200	1	4	5

Table 12.2: Table showing the calculated gas residence times for the reactor at 850 °C, assuming pure methane and ideal gas law

Reference temperature: 900°C			
Flow rate	Reactor residence time	Reactor residence time (3-fold)	Total gas residence time (3-fold)
mln/min	min	min	min
5	52	157	184
10	26	79	92
25	10	31	37
50	5	16	18
100	3	8	9
150	2	5	6
200	1	4	5

Table 12.3: Table showing the calculated gas residence times for the reactor at 900 °C, assuming pure methane and ideal gas law

Reference temperature: 750°C, values in vol-%						
Methane	Hydrogen	Ethylene	Ethane	Adj. amount	Conversion	Flow
100.17	0.08	0	0	100.25	0.08	200
100.64	0.04	0	0	100.68	0.04	200
100.76	0.01	0	0	100.77	0.01	200
100.82	0.00	0	0	100.83	0.00	150
100.85	-0.01	0	0	100.84	-0.01	150
100.92	-0.01	0	0	100.90	-0.01	150
100.80	0.01	0	0	100.81	0.01	100
100.89	0.01	0	0	100.90	0.01	100
100.90	0.01	0	0	100.91	0.01	100
100.81	0.08	0	0	100.88	0.07	50
100.78	0.07	0	0	100.85	0.07	50
100.86	0.07	0	0	100.93	0.07	50
99.11	0.14	0	0	99.25	0.14	25
100.24	0.13	0	0	100.37	0.13	25
100.87	0.13	0	0	101.00	0.13	25
100.43	0.47	0	0	100.89	0.46	10
100.45	0.46	0	0	100.92	0.46	10
100.48	0.47	0	0	100.95	0.46	10
99.77	0.93	0	0	100.70	0.92	5
99.79	0.91	0	0	100.70	0.91	5
99.82	0.90	0	0	100.72	0.89	5

Table 12.4: Conversion results measured during campaign 2.2 at 750 °C

Reference temperature: 850°C, values in vol-%						
Methane	Hydrogen	Ethylene	Ethane	Adj. amount	Conversion	Flow
100.45	0.30	0	0	100.75	0.30	200
100.57	0.33	0	0	100.90	0.33	200
100.62	0.34	0	0	100.96	0.34	200
99.76	1.14	0	0	100.90	1.13	150
99.58	1.34	0	0	100.91	1.32	150
99.68	1.23	0	0	100.91	1.22	150
99.29	1.57	0	0	100.86	1.55	100
99.41	1.46	0	0	100.88	1.45	100
99.50	1.42	0	0	100.92	1.40	100
98.22	2.53	0	0	100.75	2.51	50
98.22	2.64	0	0	100.86	2.62	50
98.25	2.68	0.01	0	100.93	2.66	50
95.90	4.88	0.17	0	100.94	5.00	25
95.79	4.90	0.07	0	100.77	4.94	25
95.82	4.94	-0.13	0	100.63	4.78	25
88.95	11.07	-0.04	0	99.98	11.03	10
89.13	10.98	-0.07	0	100.04	10.90	10
89.20	10.98	0.14	0	100.32	11.08	10
83.87	16.22	0.27	0	100.36	16.43	5
84.01	16.23	-0.08	0	100.16	16.12	5
83.93	16.32	0.16	0	100.42	16.42	5

Table 12.5: Conversion results measured during campaign 2.2 at 850 °C

Reference temperature: 900°C, values in vol-%						
Methane	Hydrogen	Ethylene	Ethane	Adj. amount	conversion	Flow
95.48	5.16	0.48	0	101.11	5.58	200
95.36	5.25	0.41	0	101.02	5.60	200
95.56	5.10	0.17	0	100.83	5.23	200
92.76	7.53	0.36	0	100.65	7.84	150
92.84	7.47	0.57	0	100.88	7.97	150
93.01	7.33	0.59	0	100.94	7.85	150
88.53	11.37	0.57	0.11	100.57	11.97	100
88.66	11.27	0.79	0.12	100.84	12.07	100
88.39	11.52	0.64	0.11	100.66	12.19	100
81.47	17.89	0.68	0.18	100.22	18.71	50
81.20	18.01	0.92	0.19	100.32	19.06	50
81.03	18.30	0.90	0.19	100.42	19.31	50
76.04	22.92	0.91	0.23	100.10	24.03	25
75.74	23.20	0.82	0.24	100.00	24.26	25
75.85	23.07	0.82	0.24	99.98	24.13	25
70.19	28.09	0.68	0.26	99.23	29.26	10
70.30	28.16	0.33	0.25	99.03	29.01	10
70.11	28.37	0.55	0.26	99.29	29.39	10
66.21	32.68	0.43	0.21	99.54	33.48	5
66.13	32.77	0.31	0.21	99.42	33.49	5
66.18	32.79	0.33	0.21	99.51	33.50	5

Table 12.6: Conversion results measured during campaign 2.2 at 900 °C

$\dot{V}_{\mathrm{STP}}$	**200**	**150**	**100**	**50**	**25**	**10**	**5**
Reference temperature: 750°C							
M 1	0.08	-0.01	0.01	0.07	0.14	0.46	0.92
M 2	0.04	0.00	0.01	0.07	0.13	0.46	0.91
M 3	0.01	-0.01	0.01	0.07	0.13	0.46	0.89
Mean	0.04	0.00	0.01	0.07	0.13	0.46	0.91
Error	$1.9{\cdot}10^{-2}$	$3.8{\cdot}10^{-3}$	$1.4{\cdot}10^{-3}$	$1.9{\cdot}10^{-3}$	$3.4{\cdot}10^{-3}$	$5.5{\cdot}10^{-4}$	$9.4{\cdot}10^{-3}$
t_{res} [min]	1.5	2.0	3.0	6.0	12.0	30.1	60.2
Reference temperature: 850°C							
M 1	0.30	1.13	1.55	2.51	5.00	11.03	16.43
M 2	0.33	1.32	1.45	2.62	4.94	10.90	16.12
M 3	0.34	1.22	1.40	2.66	4.78	11.08	16.42
Mean	0.32	1.22	1.47	2.59	4.90	11.01	16.32
Error	$1.1{\cdot}10^{-2}$	$5.7{\cdot}10^{-2}$	$4.4{\cdot}10^{-2}$	$4.5{\cdot}10^{-2}$	$6.4{\cdot}10^{-2}$	$5.3{\cdot}10^{-2}$	$1.0{\cdot}10^{-1}$
t_{res} [min]	1.4	1.8	2.7	5.5	11.0	27.4	54.8
Reference temperature: 900°C							
M 1	5.58	7.84	11.97	18.71	24.05	29.28	33.50
M 2	5.60	7.97	12.07	19.07	24.27	29.03	33.51
M 3	5.23	7.85	12.19	19.31	24.15	29.40	33.52
Mean	5.47	7.89	12.08	19.03	24.16	29.24	33.51
Error	$1.2{\cdot}10^{-1}$	$4.2{\cdot}10^{-2}$	$6.1{\cdot}10^{-2}$	$1.7{\cdot}10^{-1}$	$6.6{\cdot}10^{-2}$	$1.1{\cdot}10^{-1}$	$5.3{\cdot}10^{-3}$
t_{res} [min]	1.3	1.7	2.6	5.2	10.5	26.2	52.5

Table 12.7: Operation parameters for the experimental campaigns

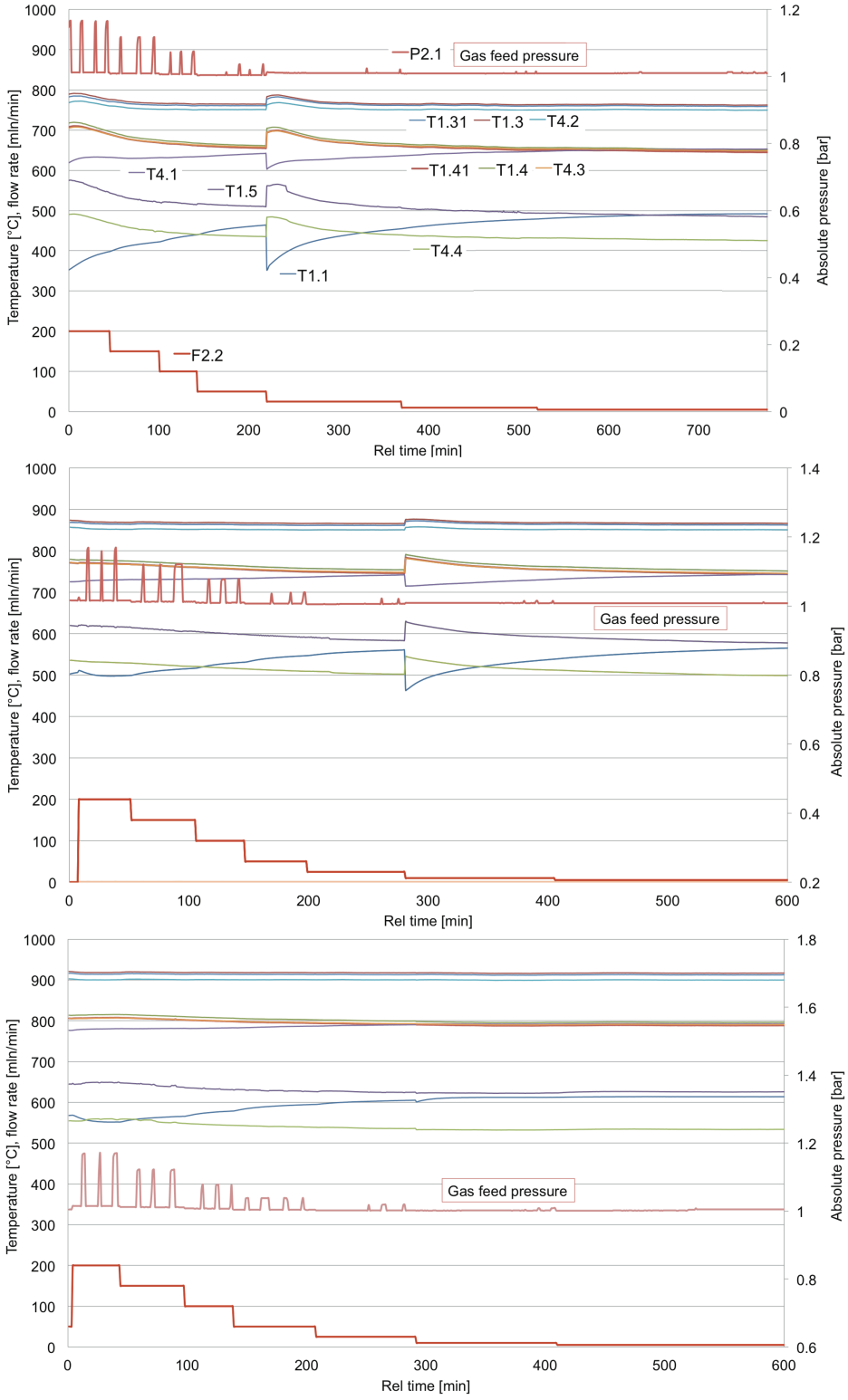

Figure 12.3: Overview of the process data obtained during the gas-phase experiments